ÇUKUROVA UNIVERSITY INTERNATIONAL CONFERENCE ON CONDENSED MATTER AND MATERIAL SCIENCES

2019 | 14-19 October , Adana/ TURKEY

http://iccm2019.cu.edu.tr

SPONSORS

ÇUKUROVA ÜNİVERSİTESİ 1973

ATO
ADANA
TİCARET ODASI

ADASO
ADANA SANAYİ ODASI

DELTA KİMYA
LABORATUVAR ÜRÜNLERİ

Pusula Medikal

giris
dijital baskı merkezi-kırtasiye

Tarihi Yeni Uğur® Helvacısı

ARMA
www.armamarble.com

anka textil
europa gmbh

Preface

Dear Participants,
I am very pleased to welcome you all to the “International Conference on Condensed Matter and Materials Science-2019 (ICCMMS-2019)” organized between 14-19 October, 2019 in Mithat Özsan Amfi of Çukurova University, Adana, Turkey.
The conference was open to all physics researchers and graduate students from all the countries. The purpose of the conference was to provide a platform for researchers and graduate students in the areas identified in Condensed Physics and Materials Science to publicize their ongoing research work through oral and poster presentations. The aim of the oral and poster presentation was to encourage the young researchers and students to research and practice on giving presentations. In this way, the young researchers and graduate students would have the opportunity to interact with their peers and publicize and get feedback on their work, exchange experiences, make contacts, and learn what other researchers are doing in the Condensed Matter Physics and Material Sciences.
It is particularly pleasing to see participation of so many graduate students, young researches and senior scientists. We are grateful to you for your contributions and support. We should also like to thank to Tubitak for support (**2223-B Scientific Meetings Grants Program, Project Number-1929B021900661**) and our sponsors for their generous contributions in this conference.

Yours Sincerely,

Bekir ÖZÇELİK
Director for ICCMMS-19

Director: Prof. Dr. Bekir ÖZÇELİK

Local Organizing Committee

Halil İbrahim Yavuz
Sezen ÖZÇELİK

Honory Committee

Prof.Dr.Mustafa KİBAR(Rector of Cukurova University)

International Advisory Board

Prof.Dr. Javier CAMPO (Spain)
Prof.Dr. Xerman de la Fuente LEIS (Spain)
Prof.Dr. Luis Alberto ANGUREL (Spain)
Prof.Dr. Andres SOTELO (Spain)
Prof.Dr. Katsuya INOUE (Japan)
Prof.Dr. Vasudeva SIRUGURI (India)
Prof.Dr. Garry MCINTYRE (Australia)

Scientific Committee

M.Ali AKSAN (İnönü Univ.)
Canan AKSOY (KTÜ)
Naoyuki AMEMİYA (Japan)
Luis Alberto ANGUREL (Spain)
Lutfi ARDA (Bahçeşehir Univ.)
Alev AYDINER (KTÜ)
İbrahim BELENLİ (Abant İzzet Baysal Univ.)
Nejat BULUT (İYTE)
Javier CAMPO (Spain)
Florinda COSTA (Portugal)
Şükrü ÇAVDAR (Gazi Univ.)
Şükrü ÇELİK (Sinop Univ.)
Tolga DEPÇİ (İSTE)
Ahmet EKİCİBİL (Cukurova Univ.)
Yüksel ERGÜN (Anadolu Univ.)
Ayşe EROL (İst.Üniv.)
Mehmet ERTUĞRUL (Atatürk Univ.)
Ramazan ESEN (Cukurova Univ.)
Xerman de la FUENTE (Spain)
Ali GENCER (Ankara Uni.)
Oğuz GÜLSEREN (Bilkent Univ.)
Marian JASKULA (Poland)
Kazuo KADOWAKI (Japan)
Hiroshi KAGAYEMA (Japan)
Faruk KARADAĞ (Cukurova Univ.)
Hakan GÜNDOĞMUŞ (Hakkari Univ.)
Hakan GÜNGÜNEŞ (Hitit Univ.)
Hamide KAVAK (Çukurova Univ.)
Kazumasa IIDA (Japan)
Haluk KORALAY (Gazi Univ.)
Andrei KOVALEVSKY (Portugal)
Çağlıyan KURDAK (USA)
Igor MOROZOV (Russia)
Marwan MOUSA (Jordan)
Süleyman ÖZÇELİK (Gazi Univ.)
Sezen ÖZÇELİK (Hakkari Üniv.)
Kemal ÖZTÜRK (KTÜ)
Sultan ÖZTÜRK (KTÜ)
Özgür ÖZTÜRK (Kastamonu Üniv.)
Berdan ÖZKURT (Mersin Üniv.)
Lütfi ÖZYÜZER (İYTE)
Shahed RASEKH (Portugal)
M.Anis-ur-REHMAN (Pakistan)
Burcu SAVAŞKAN (KTÜ)
Anatoli SIDORENKO (Moldova)
Andres SOTELO (Spain)
Yoshihiko TAKANO (Japan)
Ebru Şenadım TÜZEMEN (Cumhuriyet Univ.)
Pan WEI (China)
Akiyasu YAMAMOTO (Japan)
H.Ibrahim YAVUZ (MSU)
Ali ZAOUI (France)

Invited Speakers

Luis Alberto ANGUREL
Ali BOZBEY
Javier CAMPO
Juan B.Carda CASTELLO
Adrian CRISAN
Tolga DEPÇİ
Yüksel ERGÜN
Ramazan ESEN
Ali GENCER
Oğuz GÜLSEREN
Samir KHENE
Andrei KAVALEUSKİ
Xerman de la Fuente LEIS
Kemal ÖZTÜRK
Sultan ÖZTÜRK
Halime Ö.PAKSOY
Shahed RASEKH
David Muñoz-ROJAS
Andres SOTELO
Yoshihiko TAKANO
Akiyasu YAMAMOTO
H.Ibrahim YAVUZ
Ali ZAOUI

International Conference on Condensed Matter and Materials Science
ICCMMS-2019
14-19 October 2019
ADANA, TURKEY

Effect of Rb Substitution on the Structural, Physical and Superconducting Properties of Bi-2212 Superconductor

I.Ergin[1*], B. Özçelik[1], M. A. Madre[2], A. Sotelo[2]
[1] *Department of Physics, Faculty of Sciences and Letters, Cukurova University. 01330 Adana, Turkey*
[2] *ICMA (CSIC-Universidad de Zaragoza). María de Luna, 3. 50018 Zaragoza, Spain*
Corresponding author: erginibrahim2@gmail.com

Abstract

In this research, the effects of Rubidium (Rb) inclusion on the microstructural, physical and superconducting properties of $Bi_2Sr_2Ca_{1-x}Rb_xCu_2O_{8+y}$ with x=0.0, 0.025, 0.05, 0.075, 0.10, and 0.125, superconductor have, in detail, been studied. For this purpose, the samples were prepared through the classical solid state reaction route. From the XRD patterns, the crystal symmetries of samples were determined as pseudo tetragonal and consist of dominant Bi-2212 phase together with small amount of secondary phases. SEM-EDX results have confirmed that the major phase is related to Bi-2212, with minor amounts of secondary phases. In magnetization versus temperature measurements, very sharp diamagnetic transition is observed. The superconducting critical temperatures, T_C, for all samples are obtained around 80 K. From *M-H* measurement, it has been found that all samples have very narrow loop areas. By using the data from *M-H* measurements in the Bean model, the intragranular critical field, J_C, has been determined. It has been found that the pure Bi-2212 (x=0.0) sample shows the highest superconducting properties and the largest J_C values ($2{,}2 x 10^4$ A/cm^2 at 10 K).

Keywords: Bi-2212, Rubidium substitution, Magnetic Properties.

1. Introduction

Bi-based superconductors with Bi-Sr-Ca-Cu-O (BSCCO) content and stoichiometric 2-2-1-2 respectively are called Bi-2212, which are into the high-temperature superconductor structure. It is too easy to produce in terms of their oxidized structure and contain no rare earth elements and is not easily affected by oxygenated environments. Moreover, it has high current carrying capacity, high magnetic field carrying capacity and the high transition temperature to superconductivity makes this type of superconductor more attractive in industry. However, mechanical properties such as weak bonds, brittleness and weak elasticity in the structure of this superconductor family restrict their application. The BSCCO superconductor family with a chemical structure has n = 1, 2 and 3 phase structures (Bi-2201, Bi-2212 and Bi-2223 respectively) depending on CuO_2 content [1-3].

It has been stated the superconducting properties of the BSCCO system can be improved by alkaline metals substitutions, since their +1 valence state generates a variation in the charge carrier concentration. In addition, their ionic radii, ranging in between 73–181 pm, superpose with the Bi, Sr, Ca, and Cu ones [4-6]. In this work, the optimum amount of Rb substitution into BSCCO system by replacing Ca will be determined through the variation of structural, physical and magnetic properties of the doped systems as a function of Rb-concentration.

2. Experimental details

$Bi_2Sr_2Ca_{1-x}Rb_xCu_2O_y$ samples were produced by solid state method at x = 0.0, 0.025, 0.05, 0.075, 0.1, and 0.125 combinations. Oxidized and carbonate powders used are Bi_2O_3, $SrCO_3$, $CaCO_3$, Rb_2O and CuO. Oxidized and carbonate powders were mixed separately for each sample. The mixtures were well mixed by milling in an agate mortar and calcined twice at 750 and 800°C for 12 h in order to decompose the alkaline-earth carbonates. The purpose of the calcination course is to ensure the decomposition of carbonated structures. The carbonated structures are separated during the sintering process after calcination and can form bubble structures. In this case it may have a slowing or stopping effect on the formation of the desired crystal structure. Rigaku Minifilex, XRD device, which emits CuKa radiation at a certain ratio of 10 to 70 degrees (2θ) at room temperature as powder, was used to determine the phases in the heat treated material. From these phases, crystal lattice parameters were calculated with an uncertainty of ± 0.001. For surface morphology and elemental analysis, LEO Evo-40 VPX scanning electron microscopy (SEM) and energy dispersive spectroscopy (EDS) were used. For magnetic measurements, the 7304 model Vibrating Sample Magnetometer of Lake Shore was used to determine the transition temperature to superconductivity and to observe the magnetization change in the ±1 Tesla magnetic field.

3. Results and Discussion

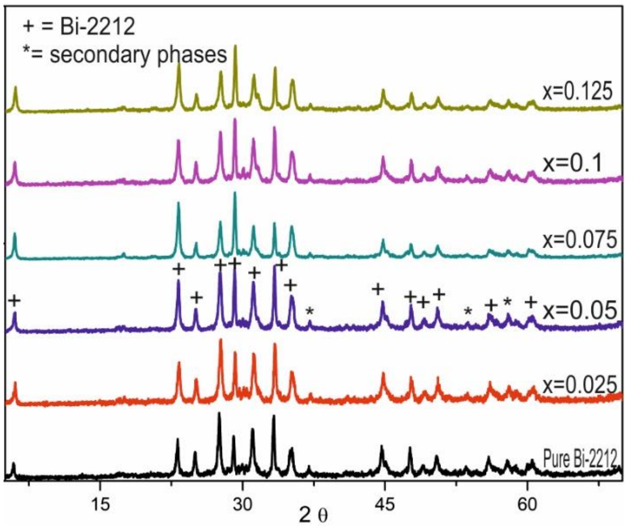

Fig. 1. XRD patterns for all samples with increasing Rb concentration from bottom to top.

As can be observed from XRD patterns given in Fig.1, the main phase labeled as (+) is Bi-2212 one together with minor phases (*), for all different Rb-substitution. The crystal symmetry is found as pseudo tetragonal with the lattice parameters, calculated by using the least squares method, are $a=b=5.398$ Å and $c=30.685$ Å, in all cases.

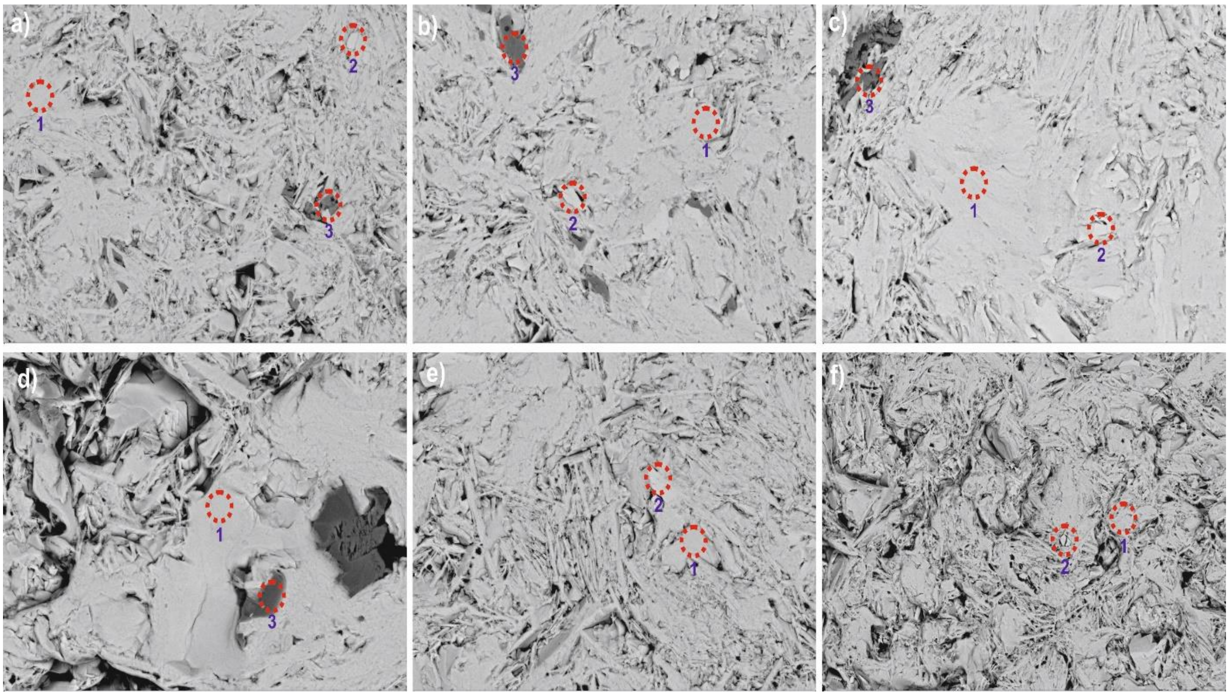

Fig. 2. SEM micrographs for all samples. (a) x=0.0, (b) x=0.025, (c) x=0.05, (d) x=0.075, (e) x=0.1, (f) x=0.125

Fig. 2 shows the phases according to the specific contrast setting on the material surface. The identities of the phases are determined according to the elemental analysis (EDS) at the places marked with 1, 2 and 3. EDS analysis of these contrasts has allowed to associate each of them to different phases: major gray contrast (indicated by #1) in all micrographs corresponds to the Bi-2212 superconducting phase, while white (#2) and dark gray (#3) have been associated to $Bi_{2+x}(Sr,Ca)_2O_{6+d}$ (without Cu phase), and $(Sr,Ca)CuO_2$ (without Bi phase) secondary phases, respectively.

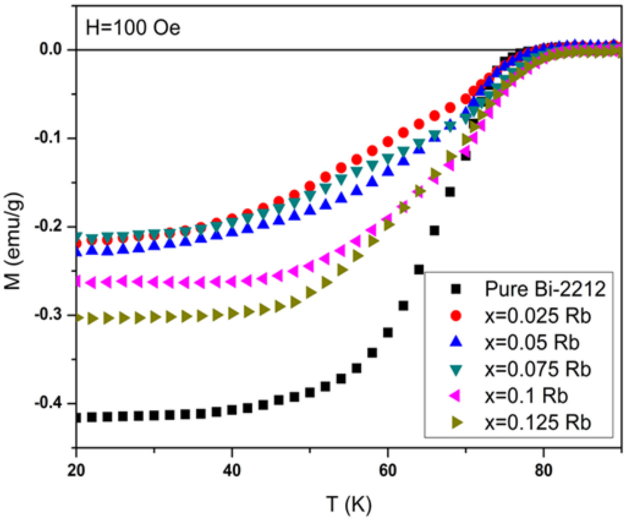

Fig. 3. Magnetization (*M)* versus temperature (*T*), for all samples.

Magnetization, *M*, versus temperature is exhibited in Fig. 3, for all samples. All data were generated in a cooled mode under magnetic field from 20 K to 100 K under 100 Oe magnetic field. By increasing the sensitivity in a temperature range close to the transition temperature, T_C, it is provided to determine the transition temperatures to an exact value. From the *M-T* graph, the critical transition temperatures for all samples were deduced in a very similar way. It can be seen from Table 1 that all samples, regardless of the concentration of the Rb additive, have a critical transition temperature of around 80 K.

Samples	***T_C (K)***
x=0.0	80
x=0.025	78.6
x=0.05	80.3
x=0.075	79.5
x=0.1	79
x=0.125	82

Table 1. Critical transition temperature, T_C, for all samples

It is likely that diamagnetic behavior makes it difficult to infiltrate the magnetic field between these grain boundaries due to the strong connection between the grain boundaries.

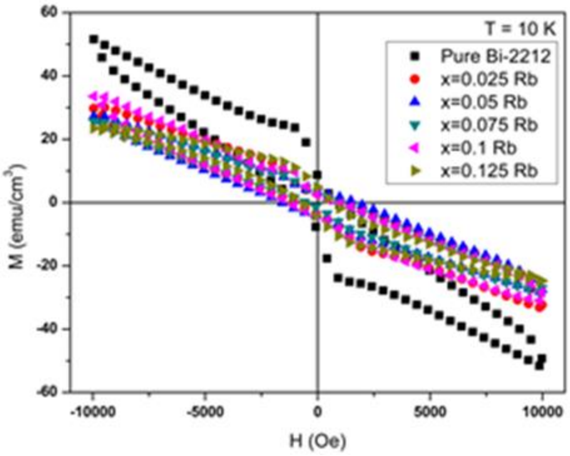

Fig. 4. Magnetization, *M*, versus magnetic field, *H*, for all samples.

The *M–H* loops measured at 10 K, between ±1 Tesla applied external fields, and determined under ZFC mode, are presented in Fig. 4. All samples exhibit very narrow hysteresis and the area of these hysteresis loops decrease depending on concentration. *M-H* data were used in Eq. 1, proposed for quadrangular samples, in the well-known critical Bean model [7]

$$J_C = 20\frac{\Delta M}{a(1-\frac{a}{3b})} \tag{1}$$

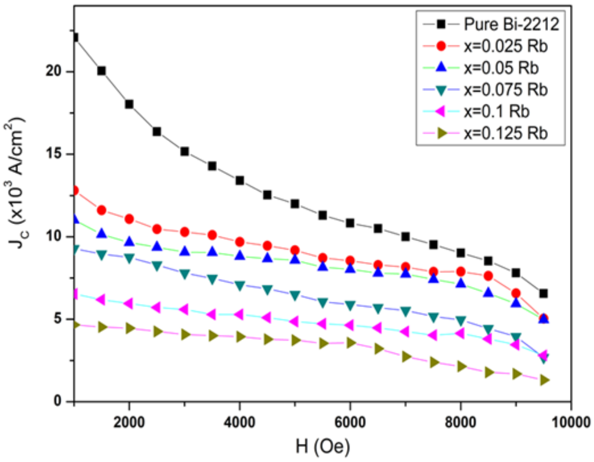

Fig. 5. Critical current density, J_C, versus magnetic field, *H*, for all samples.

where $\Delta M = M_+ - M_-$ is measured in electromagnetic units per 200 Oe, ***a*** and ***b*** are the length of the sample plane perpendicular to the applied magnetic field. Using the Eq.1, the intragranular critical current density values, *Jc*, in ampéres per square centimeter are calculated for all samples, and the results obtained at 10 K are presented in Fig. 5. These data clearly show that the pure sample (x=0.0) possesses higher superconducting properties and has the largest J_C values (2,2x10^4 A/cm^2 at 1000 Oe fields), which explicitly reduce when the magnetic field and the amount of Rb are raised. In this stage, it is possible to argue that the different type of secondary phases embedded in the crystal structure can reveal such a kind of results. According to the flux-pinning mechanism, those non-superconducting phases behave like very effective flux-pinning centers. Depending on the sizes of those secondary phases, the applied fields may diffuse into the sample, causing a decline in the critical current, Jc, values. The maximum J_C value obtained for the x=0.05 sample is almost near with the given in literature for Vanadium (2.53×10^5 A/cm^2) [8], and very similar to the obtained in Cs-substituted materials ($2{,}3 \times 10^4$ A/cm^2) [9]. This effect may be associated to the different cation sizes affecting the oxygen quantity and the number of charge carrier. In addition, comparison to Na-doped materials, a possible slight charge carrier concentration enhancement can be arisen by the lower effective attraction of the external electrons in the Rb^+ cations [10].

Conclusions:

In summary, the structural, physical and magnetic properties of $Bi_2Sr_2Ca_{1-x}Rb_xCu_2O_{8+y}$ superconducting material with x=0.0, 0.025, 0.05, 0.075, 0.10, and 0.125 has been intensively studied. X-ray diffraction patterns indicate that all samples have main Bi-2212 phase. SEM micrographs and EDX results have shown that Bi-2212 was major phase with minor amounts of secondary phases. A very sharp diamagnetic transitions typical for granular materials were observed, when measuring magnetization versus temperature. The critical onset temperatures were around 80 K, independently of Rb content. *M-H* measurements have shown that the hysteresis loops are very narrow. The critical current field, J_C, of pure sample was found the highest value as $2{,}2 \times 10^4$ A/cm^2.

Acknowledgements

M. A. Madre, and A. Sotelo acknowledge the MINECO-FEDER (MAT2017-82183-C3-1-R), and Gobierno de Aragon-FEDER (Research Group T 54-17 R) for funding. The authors wish to acknowledge the use of Servicio General de Apoyo a la Investigación-SAI, Universidad de Zaragoza.

References

[1] H. Maeda, Y. Tanaka, M. Fukutumi, T. Asano, Jpn. J. Appl. Phys. 27, 209 (1988)
[2] C. Michel, M. Herviev, M.M. Borel, A. Grandin, F. Deslands, J. Provost, B. Raveav, Z. Phys. B 86, 421 (1987)
[3] J.M. Tarascon, W.R. McKinnon, P. Barboux, D.M. Hwang, B.G. Bagley, L.H. Greene, G.W. Hull, Y. LePage, N. Stoffel, and M. Giroud, Phys. Rev. B, 1988. 38(13): 8885-8892**.**
[4] B. Ozcelik, M. Gursul, A. Sotelo, M. A. Madre, J. Mater. Sci. Mater. Electron. **26**, 441 (2015)
[5] B. Ozcelik, M. Gursul, A. Sotelo, M. A. Madre, J. Mater. Sci. Mater. Electron. **25**, 4476 (2014)
[6] L.D. Sykorova, O. Smrckova, V. Jakes, Phys. Stat. Sol. (C) **1**(7), 1952 (2004)
[7] C. P. Bean, Phys. Rev. Lett., 8, 250 (1962)
[8] Nane, O. & Özçelik, B. J Mater Sci: Mater Electron (2016) 27: 7633. https://doi.org/10.1007/s10854-016-4747-3
[9] I. Ergin, B. Özçelik, M.A. Madre, A.Sotelo, J Supercond Nov Magn. https://doi.org/10.1007/s10948-019-05150-4
[10] Özçelik, B., Gürsul, M., Sotelo, A. et al. J Mater Sci: Mater Electron (2015) 26: 441. https://doi.org/10.1007/s10854-014-2419-8

International Conference on Condensed Matter and Materials Science
ICCMMS-2019
14-19 October 2019
ADANA, TURKEY

Specific Heat Capacity Behaviours of P/M Distaloy AE Alloy Compacts

Ayşe Nur ACAR[1,2], Abdul Kadir EKŞİ[2], Ahmet EKİCİBİL[3]

[1]Cukurova University, Ceyhan Engineering Faculty, Mechanical Engineering Department, Ceyhan, Adana, Turkey
[1]Cukurova University, Engineering Faculty, Mechanical Engineering Department, Sarıçam, Adana,,Turkey
[3]Cukurova University, Sciences and Letters Faculty, Physics Department, Sarıçam, Adana, Turkey
Corresponding Author: Ayşe Nur ACAR; anacar@cu.edu.tr

The alloying techniques consist of pre-alloyed, pre-mixed and diffusion-bonded powders. Depending on these techniques, microstructures of steel alloys that are produced via powder metallurgy (P/M) method change. Distaloy AE alloy used in this study is type of diffusion-bonded alloy consisting of Fe, Ni and Mo alloying elements and has high strength sintered components. In this study, distaloy AE powder pressed on the 400 and 600 MPa pressures via die pressing technique. Compacted distaloy AE alloy samples sintered at 1200°C for 2 hrs under N_2 atmosphere. Sintered distaloy AE alloy samples cut to down small pieces. Specific heat capacity behaviours of these small alloy pieces have been examined at temperature ranging from 0 to 600 °C via heat flux type Differential Scanning Calorimeter (DCS). Specific heat capacity measurements supported by SEM images, EDS spectrums and XRD patterns of these alloy samples.

Introduction

Powder metallurgy, which is one of manufacturing methods of iron and iron-based alloys, provides net or near-net shape, better material utilization, pure microstructure, controllable characteristic properties and high dimensional stability [1-4]. This method consists of various stages of powder preparation, shaping of powder and sintering of shaped powders and secondary operations to sintered body [5]. This sintered body has regular-net shape, strengthening microstructure.

Related to alloying techniques such as pre alloyed, pre mixed, and diffusion bonded; microstructures of iron and iron based alloys prepared by powder metallurgy changes. Pre alloyed or diffusion bonded alloys have Fe,Ni and Mo alloying elements and more relevance for researchers owing to high strengthening structure and possess more utilization areas in industry [6-8]. The distaloy AE is a diffusion bonding powder and consist of Fe, Ni and Mo alloying elements. Alloying elements spread into the Fe. Between Fe and spreading alloying elements, metallurgical bonding occurs. Therefore, the microstructure of Fe-alloy gains high strengthening besides high compactibility [8-10].

The thermophysical properties refers as physical properties changing with temperature; specific heat capacity of alloys is also needed heat amount to rise temperature of 1 g alloy by 1°C [12-14]. In this work; the thermophysical properties (i.e. specific heat capacity) of distaloy AE alloys prepared by powder metallurgy method have been examined and discussed how this properties of this alloys changes with the powder metallurgy method.

Material and Method

In this work; Distaloy AE alloy powder which is acquired from Höganas in Sweden used. The chemical composition of this powder consists of 0.01 of C%, 4.00 of Ni%, 0.50 of Mo% and Fe in balance and also, particle shape of this powder has irregular appearance as seen in Figure 1.

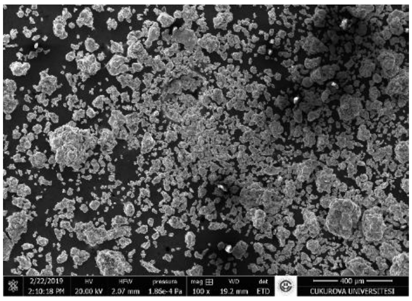

Figure 1. The SEM image of Distaloy AE alloy powder

In order to acquire homogeneous distribution; this Distaloy AE powder was blended with lubricant and 37 g of distaloy AE alloy mixture was placed into prismatic mold of (10×15×70) mm and pressed on the 400 and 600MPa pressures applying conventional pressing technique at RT (room temperature). The pressed Distaloy AE specimens, sintered under N_2 atmosphere. Firstly; Samples waited on the 600and 900°C temperatures for 30 min in order to delubricate, debind and remove contaminants and oxides according to literature [15-17]. After, samples sintered 1200°C, for 2 hours and after then, cooled to room temperature in furnace. Heating and cooling rate were selected as 5°C/min. In this work; the specific heat capacity behaviours of these sintered samples were examined and sintered samples cut to down small pieces. These behaviours of these samples were performed at range of Differential Scanning Calorimeter (DSC) with 20 °C/min of heating rate, 50mL/min gas flow and applied under N_2 atmosphere and also the Specific heat capacity measurements of these samples supported by SEM images using FEI Quanta 650 Field Emission SEM device; EDS spectrums which is subsidiary SEM device and crystal structures of these samples characterized using PANalytical Empyrean XRD (λ=1.54Å).

Results and Discussions

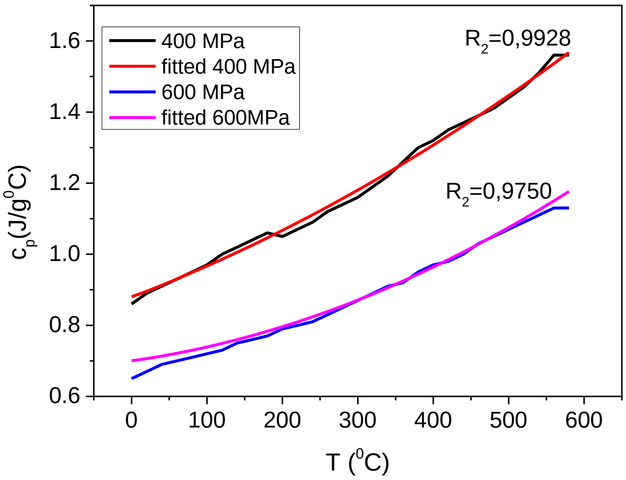

Figure 2. The Specific Heat Capacity (c_p) versus temperature curves of Sintered Distaloy AE alloy samples with fitted c_p values

In Figure 2; the specific heat capacity versus temperature curves of Distaloy AE samples prepared on 400 and 600 MPa pressures are observed and in Table 1., specific heat capacity values of these samples are given with fitted cp values and errors of percentages. With increasing of temperature; specific heat capacity values of both samples increases. Generally; as increasing of pressure; pores closes and grain binding occurs and the structure of materials has more strengthening structure. It was interested that when increasing pressure, specific heat capacity of samples decreased. It can be considered and recommended that carbide precipitations in the microstructures of alloy cause to increase thermophysical properties. Maximum specific heat capacity is obtained on the sample prepared on the high pressure (1,56 J/g°C, 580 °C). For sample prepared on the 400 MPa pressures, At range of 200 - 380°C temperature; plateau like appearance observed and it can be recommended that this appearance resulted from precipitation which is occurred on the structure of samples [18]. On the Figure 2; Both specific heat capacity v.s temperature curves of distaloy AE alloy samples fitted according to equation (1) that is formula of Specific heat capacity [19]. The fit coefficients and nonlinear –squares regression values of specific heat capacity behaviour of both distaloy AE alloy samples were given on the Table 2. From non linear-squares regression values of distaloy AE samples on Table 2; the better fit was provided on the sample prepared on the low pressure (R^2=0.9928).

$$c_p = c_0 + c_1 x + c_2 x^2 + c_3 x^{-3} \qquad (1)$$

Table 1. The Specific Heat Capacity values versus temperature of sintered Distaloy AE alloy samples with fitted cp values and errors %

T	400MPa	Fitted 400 MPa	Error%	600 MPa	Fitted 600 MPa	Error%
0,1	0,86	0,88025513	2,355248	0,65	0,70131	7,893846154
20	0,89	0,895729145	0,643724	0,67	0,70636	5,426865672
40	0,91	0,91270368	0,297108	0,69	0,71344	3,397101449
60	0,93	0,930197752	0,021264	0,7	0,72124	3,034285714
80	0,95	0,948211362	-0,18828	0,71	0,72976	2,783098592
100	0,97	0,966744508	-0,33562	0,72	0,739	2,638888889
120	1,0	0,985797192	-1,42028	0,73	0,74896	2,597260274
140	1,02	1,005369413	-1,43437	0,75	0,75964	1,285333333
160	1,04	1,025461172	-1,39796	0,76	0,77104	1,452631579
180	1,06	1,046072467	-1,31392	0,77	0,78316	1,709090909
200	1,05	1,0672033	1,63841	0,79	0,796	0,759493671
220	1,07	1,08885367	1,762025	0,8	0,80956	1,195
240	1,09	1,111023578	1,928769	0,81	0,82384	1,708641975
260	1,12	1,133713022	1,224377	0,83	0,83884	1,065060241
280	1,14	1,156922004	1,484386	0,85	0,85456	0,536470588
300	1,16	1,180650524	1,780218	0,87	0,871	0,114942529
320	1,19	1,20489858	1,251982	0,89	0,88816	-0,206741573
340	1,22	1,229666174	0,792309	0,91	0,90604	-0,435164835
360	1,26	1,254953305	-0,40053	0,92	0,92464	0,504347826
380	1,3	1,280759973	-1,48	0,95	0,94396	-0,635789474
400	1,32	1,307086178	-0,97832	0,97	0,964	-0,618556701
420	1,35	1,333931921	-1,19023	0,98	0,98476	0,485714286
440	1,37	1,361297201	-0,63524	1,0	1,00624	0,624
460	1,39	1,389182018	-0,05885	1,03	1,02844	-0,151456311
480	1,41	1,417586373	0,538041	1,05	1,05136	0,12952381
500	1,44	1,446510264	0,452102	1,07	1,075	0,46728972
520	1,47	1,475953693	0,405013	1,09	1,09936	0,858715596
540	1,51	1,50591666	-0,27042	1,11	1,12444	1,300900901
560	1,56	1,536399163	-1,51287	1,13	1,15024	1,791150442
580	1,56	1,567401204	0,474436	1,13	1,17676	4,138053097

Table 2. The fit coefficients and nonlinear –squares regression values of specific heat capacity behaviour of Distaloy AE alloy samples prepared on the 400 and 600 MPa pressures.

	400 MPa	**600 MPa**
c_0	0,87927415	0,7
c_1	0,00080976	0,0003
c_2	6,4942E-07	0,0000009
c_3	0,0000009	0,0000001
R^2	0,9928	0,9750

In Figure 3; The SEM images and EDS spectrums of Distaloy AE samples prepared on the 400and 600MPa pressures are given. Surfaces of both Distaloy AE samples, has smooth appearances. On the EDS spectrums on the sintered Distaloy AE samples; it was appeared that C, Ni, Cu ratios decreased, Fe and Mo increased. This case supported by XRD patterns. Sintering at 1200°C, reaction forming among alloy matrix and carbides produces a liquid phase. This liquid phase causes to densification [20]. Much carbon amount on the microstructure of Distaloy AE alloy prepared on the low pressure causes transition to martensitic structure having Cu-rich network [6]. Porosity in diffusion bonded alloys are observed in martensitic structures on both Distaloy AE alloys. This situation is much more on the sample prepared on the 400MPa pressure. Ni-rich areas lead to austenitic structure and Cu melts at approximately ~1083°C and throughout sintering process; liquid phase around powder particles forms and Ni diffusion occur into the Cu-melting. Ni and Cu-rich martensitic structure have a role on the reinforcing of the sintering neck [6].

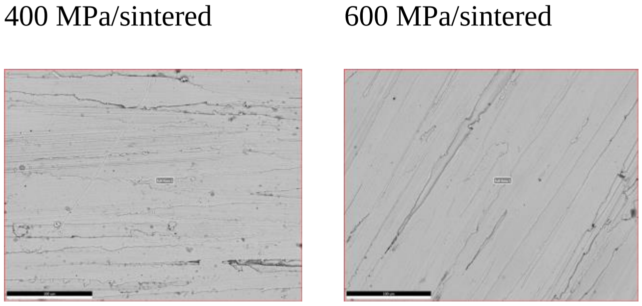

(a) (b)

	400MPa/sintered
C	4.11
Ni	4.21
Cu	1.56
Mo	0.3
Fe	89.82

(c)

600MPa/sintered	
C	3.7
Ni	4.09
Cu	1.28
Mo	0.34
Fe	90.59

(d)

Figure 3. The SEM images (a and b) and EDS Spectrums (c and d) of Distaloy AE alloy compacts prepared on the 400 and 600MPa pressures

In Figure 4; the XRD patterns of powder and sintered Distaloy AE samples are seen. On the XRD patterns of these alloy; it was appeared that Fe, Ni alloying element into microstructure of alloys were dominated to Cu alloying element. XRD pattern of this alloy powder; (111) cubic crystal structure (at 43.4°) changed to (011) crystal structure on the both sintered Distaloy AE alloys and at 50.59-51.85° range (020) cubic crystal structure (Cu,Ni) on the distaloy powder was not seen on both sintered Distaloy AE alloys [21].

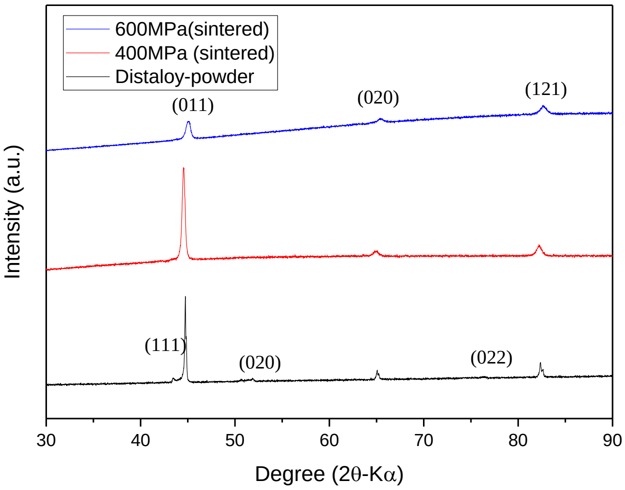

Figure 4. The XRD patterns of powder and press-sintered Distaloy AE alloy samples

Conclusion

On this work; specific heat capacity behaviours of Distaloy AE alloy samples prepared by powder metallurgy method were examined. Following experimental results are given;

- When increasing of temperature; specific heat capacity values of both Distaloy AE samples increased
- When increasing of pressure; specific heat capacity values of distaloy AE alloys decreased.
- Surfaces of both alloy samples showed smooth surfaces and also it can be recommended decreasing C , Cu, Ni in the microstructures of alloy samples caused to thermophysical properties of samples.

Acknowledgement: The authors are greatly thankful to Cukurova University research funding (FBA-2018-11074)

References

[1] Panda S.S., Singh V., Upadhyaya A., Agrawal D., Sintering Response of Austenitic (316L) And Ferritic (434L) Stainless Steel Consolidated in Conventional and Microwave Furnaces, Scripta Materialia 54 (2006) 2179–2183

[2] Giménez S., Vagnon A., Bouvard D., Van der Biest O., Influence of the Green Density on the Dewaxing Behaviour of Uniaxially Pressed Powder Compacts, Materials Science and Engineering A 430 , (2006) ,277–284

[3] Yılmaz R.,Ekici M.R., Üretim Parametrelerin Düşük Alaşımlı TM Çeliklerin Sertlik Ve Aşınma Özelliklerine Etkisi ISITES2015 Valencia –Spain, 2545-2554

[4] Zarebski K., Putyra P., 2015, Iron Powder-based Graded Products Sintered by Conventional Method and by SPS, Advanced Powder Technology 26 (2015) 401–408

[5] Al-Qureshi H.A., Galiotto A., Klein A.N., On the Mechanics of Cold Die Compaction for Powder Metallurgy, Journal of Materials Processing Technology 166 (2005) 135–143

[6] Abdoos H., Khorsand H., Shahani A.R., Fatigue Behavior of Diffusion Bonded Powder Metallurgy Steel with Heterogeneous Microstructure, Materials and Design 30 (2009) 1026–1031

[7] James WB, OtBrien RC. High performance Ferrous PM Materials: The Effect of Alloying Method on Dynamic Properties. Progress in powder Metallurgy. Princeton NJ: MPIF; 1986.

[8] Alzati L, Bergmark A, Andersson J. Fatigue Performance of PM Steel in Assintered State. Presented at PMAI conference, Mumbai, India, February;2005

[9]Lindskog P. The history of Distaloy, Powder Metallurgy, 56:5, (2013) 351-361,

[10]Öksüz K.E., Kumruoğlu L.C., Tur O. , Effect of Sic$_p$ on the Microstructure and Mechanical Properties of Sintered Distaloy DC Composites, (5th International Biennial Conference on Ultrafine Grained and Nanostructured Materials, UFGNSM15), 11-12 November 2015, Tehran-Iran, Procedia Materials Science 11 (2015) 49 – 54

[11]Karwan-Baczewska J. ,2011, The Properties Of Fe-Ni-Mo-Cu-B Materials Produced Via Liquid Phase Sintering, Archives of Metallurgy and Materials Volume 56 2011 Issue 3, 789-796

[12]Morintale E., Harabor A., Constantinescu C., Rotaru P. 2015, Use of Heat Flows from DSC Curve for Calculaion of Specific Heat of the Solid Materials, Physics AUC. Vol. 23, 89-94

[13]Wielgosz, E., Kargul T., Falkus J. 2014, Comparison of Experimental and Numerically Calcuated Thermal Properties of Steels, International Conference on Metallurgy and Materials, Metal 2014, May 21 st-23rd 2014, Brno, Czech Republic

[14]Fang H.,, Wong M.B., Bai Y. 2015,Use of Kinetic Model for Thermal Properties of Steel at High Temperatures, Australian Journal of Civil Engineering, 13:1, 40-47,

[15]Pandya S., Ramakrishna K.S., Annamalai A.R., Upadhyaya A., Effect of Sintering Temperature on the Mechanical and Electrochemical Properties of Austenitic Stainless Steel, Materials Science and Engineering A 556 (2012) 271–277,

[16] Butković S., Oruč M., Šarić E., Mehmedović M., Effect of Sıntering Parameters on the Density, Microstructure And Mechanical Properties of the Niobium-Modified Heat-Resistant Stainless Steel GX40CrNiSi25-20 Produced by MIM Technology, Materiali in tehnologije / Materials and technology 46 (2012) 2, 185–190,

[17]Butković S., Sinterability And Tensile Properties of Nickel Free Austenitic Stainless Steel X15CrMnMoN 17 11 3,Tehnički vjesnik 20, 2(2013), 269-274 269, Technical Gazette 20, 2(2013), 269-274).

[18] Wilthan B., Reschab H., Tanzer R., Schützenhöfer W., Pottlacher G., Thermophysical Properties of Chromium-nickel-Molybdenum Steel in the Solid and Liquid Phases, Int. J. Thermophys. (2008), 29: 434-444.

[19] Kelley K.K. 1949, X. High - Temperature Heat - Content, Heat - Capacity, and Entropy Data For İnorganic Compounds, Bureau of Mines Bull. 476, 192.

[20] Karwan-Baczewska J. Processing and Properties of Distaloy SA Sintered Alloys with Boron and Carbon, Archives of Metallurgy and Materials 2015 ,60 (1),41-45

[21] _Acar A.N., Ekşi A.K., Ekicibil A. Structural and Physical Properties of Sintered Distaloy AE Alloy Compacts, The Proceedings of Fourth International Iron and Steel Symposium (UDCS’19) April 4-6, 2019, Karabuk University, Karabuk, Turkey. pp. 231-233.

Magnetic Properties of Pt-doped Co nanoparticles at 20 K

Dogan Kaya[1], Idris Adanur[2], Mustafa Akyol[3], Faruk Karadag[2], Ahmet Ekicibil[2]

[1]Cukurova University, Vocational School of Adana, Department of Electronics and Automation, Adana, Turkey, dogankaya@cu.edu.tr
[2]Cukurova University, Faculty of Art and Sciences, Department of Physics, Adana, Turkey
[3]Adana Alparslan Turkes Science and Technology University, Faculty of Engineering, Materials Engineering Department, Adana, Turkey

ABSTRACT

Co- and Pt-rich CoPt nanoparticles are synthesized by polyol process to control the structural and magnetic properties for bottom-up nanotechnological applications. This process provides monodispersed and uniform cluster formations in the samples, which are revealed by SEM images, with an average size of 13 and 9 nm for Co_3Pt_1 and $Co_{0.5}Pt_1$, respectively. We also determined magnetization as a function of the applied field up to 5 T, and the nanoparticles exhibit ferromagnetic order at 20 K. When we examine the hysteresis loop of the samples, the large coercive field (H_c), remanent magnetization (M_r), and saturation magnetization (M_s) are observed in the Co-rich Co_3Pt_1 sample. This is because Co provides ferromagnetic order in the structure and Pt compensates this order in the Pt-rich $Co_{0.5}Pt_1$ sample.

Key Words: Doping Pt, CoPt, Nanoparticles, Magnetic properties

1. INTRODUCTION

Tailoring magnetic nanoparticles properties at the subnanometer scale have attracted great attention because of potential applications in magnetic resonance imaging (MRI) and magnetic recording media [1-4]. To be applicable for biomedical purposes, these particles should provide low toxicity, biocompatible and biodegradable in the body [5,6]. Therefore, controlling the magnetic properties of ferromagnetic (Fe, Co, Ni, etc.) atoms doping with noble metals (Au, Pt, Pd, Ag, etc.) is highly important for realistic applications. Among them, Co is a soft ferromagnetic material and widely uses in magnetic storage [7] and lithium battery [8] applications. In this context, the magnetic properties of Co nanoparticles can be tailored with doping Pt, Pd, and Au. CoPt nanoalloys can be investigated with several methods: magnetron sputtering, thermal decomposition, polyol and solgel processes [4,9-11]. While the physical methods provide more precise nanoparticle growth with a size of subnanometer scale, the chemical methods allow us to produce a large amount of nanoparticles in considerably short time. The size of CoPt are highly depended on temperature and processing time to produce a monodispersed and uniformly distributed samples. Synthesizing CoPt nanoparticles via polyol process provide order-disorder phase transitions at a sub-10 nm scale [3].

We study the effect of Pt content in the magnetic properties of CoPt nanoparticles. Therefore, we produced Co- and Pt-rich CoPt samples using polyol process. This chemical process allows us to control Co and Pt ratio in the structure, so the structural and magnetic properties. Scanning Electron Microscope (SEM) images used to determine the size and formation of nanoparticles in the samples. We also performed magnetic measurements at 20 K as a function of applied field. In this experiment, Co- and Pt-rich CoPt nanoparticles magnetic properties determined such as coercive field (H_c), exchange bias (H_e), remanent magnetization (M_r), and saturation magnetization (M_s).

2. EXPERIMENTAL METHOD

We prepared CoPt nanoparticles using polyol process. In this chemical reaction, for Co_3Pt_1 sample 2.34 mmol Co(II) acetylacetonate ($C_{10}H_{14}O_4Co$, 257.15 g/mol) and 0.78 mmol Pt(II) acetylacetonate ($C_{10}H_{144}Pt$, 393.29 g/mol) as starting material in a flask and than 0.78 mmol 1-2Hexadecanediol ($C_{19}H_{34}O_2$, 6.46 g) as reducing agent added and dissolved in diethyl ether solution. Following, 15.6 mmol oleylamine ($C_{18}H_{37}N$, 267.49 g/mol) and 15.6 mmol oleic acid ($C_{16}H_{34}O_2$, 282.46 g/mol) added at 40 °C to prevent aggregation and oxidation, respectively. The solution temperature increased slowly up to 200 °C under N_2 gas flow and waited for 1 h to observe a clear black color where the CoPt nanoparticles are formed. Then the solution is left to cool down to room temperature and washed with n-hexane and separated by centrifugation cycles (9000 rpm for 10 min) after adding ethanol. The particles stayed in an owen at 50 °C for two days. We imaged the formation and size of the particles by FEI scanning electron microscopy (SEM) at 20 kV. The magnetizations of the samples were measured as a function of applied field at 20 K by Quantum Design Physical Property measurement system (PPMS) with a vibrating sample magnetometer (VSM) head.

3. RESULTS AND DISCUSSION

To study the effect of Pt in CoPt nanoparticles, we produced Co rich and Pt rich nanoparticles, Co_3Pt_1 and $Co_{0.5}Pt_1$, respectively. The CoPt nanoparticle morphology was determined by scanning electron microscopy images and presented in Figure1 (a, b) for both samples. We observed that all particles monodisperse without agglomeration for both samples. The particles also provide round-like formation which can be revealed via SEM images. The average particle sizes of Co and Pt rich particles found to be 13 and 9 nm, respectively (see Table 1). The size of particles plays a crucial role on magnetic properties due to the surface area and interaction between FM Co atoms and metallic Pt atoms [2]. We also observed that long-range flat surfaces with no impurity on the surfaces via SEM images.

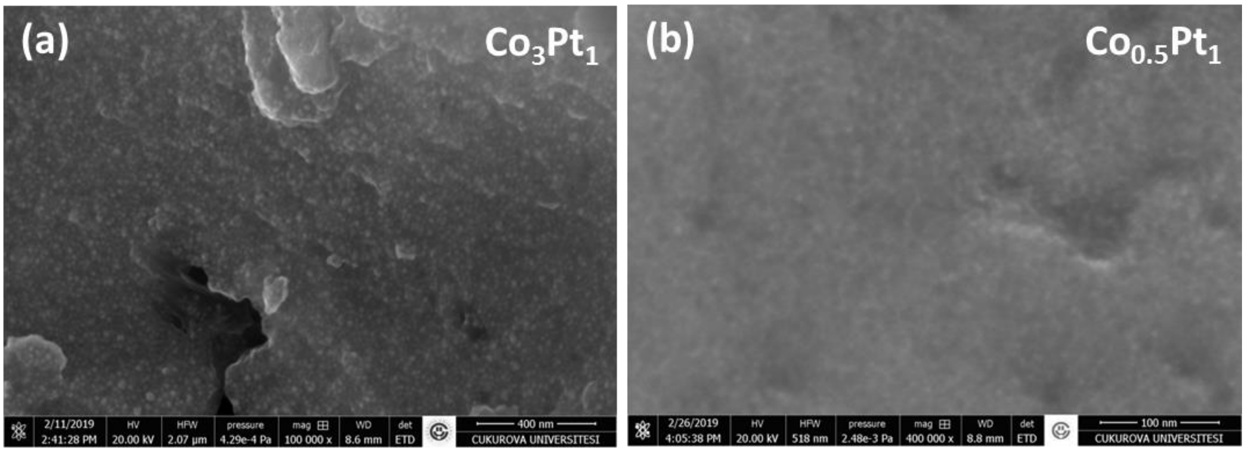

Figure 1: (a-b) Uniform distributed particles reveal by SEM images Co_3Pt_1 and $Co_{0.5}Pt_1$ with x100000 and x400000 magnifications, respectively.

In Figure2, the magnetic moment measurements as a function of applied field performed via a PPMS-VSM magnetometer. The black and red loops in Figure2 (a,b) are magnetic moments of Co_3Pt_1 and $Co_{0.5}Pt_1$ samples, respectively. We observed clear hysteresis loops for both samples at 20 K. While CoPt nanoparticles exhibit paramagnetic behaviour at room temperature without hysteresis loop [11,12], a ferromagnetic behaviour is observed at 20 K which is below the blocking temperature of CoPt nanoparticles ($T_B \approx 58$ K) [12]. We calculated coercive field (H_c), exchange bias (H_e), remanent magnetization (M_r), and saturation magnetization (M_s) from the hysteresis loops that are given in Figure2 (b) with zooming around the origin and all values presented in Table 1.

We recorded positive ($+H_c$) and negative ($-H_c$) intercepts of the field axis and calculated the coercive field $H_c=(+H_c-(-H_c))/2$ and the exchange bias $H_e=(+H_e+(-H_e))/2$. We found that the H_c exhibits considerable high (115.05 Oe) for Co-rich sample (Co_3Pt_1) with comparing Pt-rich sample (31.25 Oe). This is because the ferromagnetic order of Co atoms in the nanoparticle is not compensated with Pt atoms. Besides, H_e is found 13.25 Oe and 2.55 Oe for Co_3Pt_1 and $Co_{0.5}Pt_1$ samples, respectively. These values are negligible and prove that there is no antiferromagnetic (AFM) order in the sample. Therefore, we can conclude that the system is prevented from oxidation and CoO formation so AFM order. Moreover, M_r is obtained from both positive and negative intercepts of the magnetic moment axis. We calculated 10.79 and 2.54 emu/gr for Co_3Pt_1 and $Co_{0.5}Pt_1$ samples, respectively. The Co-rich sample provides four times higher remanent magnetization. M_s also calculated as 30.63 and 18.75 emu/gr for both samples at a magnetic field of 5 T which is considered not enough for both samples.

Table 1: Calculated values of average particle size, coercive field (H_c), exchange bias (H_e), remanent magnetization (M_r), and saturation magnetization (M_s) from the hysteresis loops for Co_3Pt_1 and $Co_{0.5}Pt_1$ samples at 20 K.

	Average Particle Size (nm)	**H_c (Oe)**	**H_e (Oe)**	**M_r (emu/gr)**	**M_s (emu/gr)**
Sample 1	13	115.05	13.25	10.79	30.63
Sample 2	9	31.25	2.55	2.54	18.75

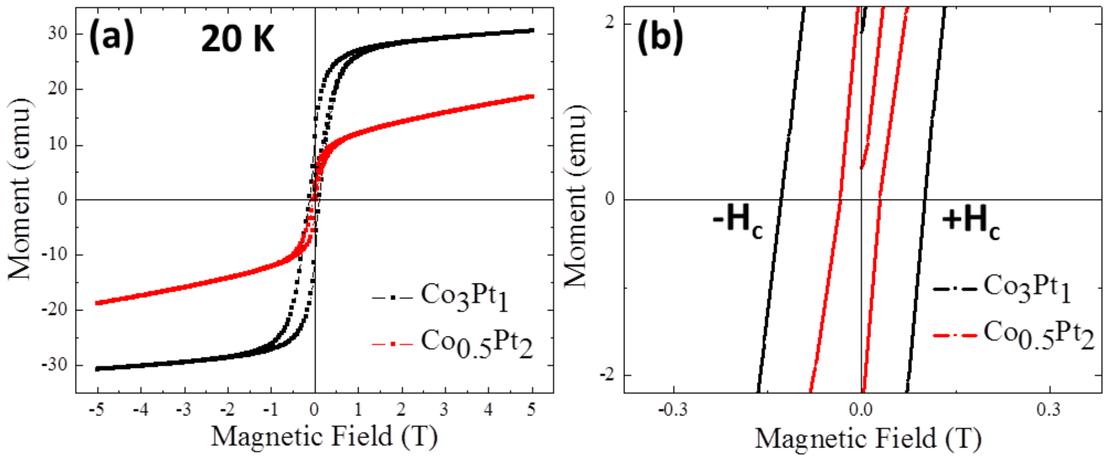

Figure 2: Magnetic moment measurements as a function of applied field up to 5 T for Co_3Pt_1 (black) and $Co_{0.5}Pt_1$ (red) samples. (a). *M(H)* of Co_3Pt_1 and $Co_{0.5}Pt_1$ samples at 20 K. (b). The enlarged M-H graph.

4. CONCLUSION

In summary, we investigated the formation and magnetic properties of Co and Pt-rich CoPt nanoparticles. Polyol process allows us to produce monodispersed nanoparticle with a size of 13 and 9 nm for Co_3Pt_1 and $Co_{0.5}Pt_1$, respectively. The average size of Co-rich nanoparticles is enhanced due to more Co involved in the structure. The particle distributions for both samples are uniform without agglomeration which is revealed by SEM images. This provides more magnetic properties in the samples. The magnetic properties of samples are determined by measuring hysteresis loops at 20 K. All coercive field (H_c), exchange bias (H_e), remanent magnetization (M_r), and saturation magnetization (M_s) values are enhanced by Co content in the structure. So Pt can be doped in Co nanoparticles to control the magnetic properties of Co-based nanoparticles for ultrahigh density memory devices, biological and medical purposes.

ACKNOWLEDGEMENT

The authors are thankful for the financial support of Cukurova University Scientific Research Funding Grand No: FBA-2018-10412.

REFERENCES

1. Ourry L, Mammeri F, Toulemon D, Gaudisson T, Delamar M, et al. (2016) A tandem polyol process and ATRP used to design new processable hybrid exchange-biased Co x Fe 3− x O 4@ CoO@ PMMA nanoparticles. RSC Advances 6: 49973-49979.
2. Ourry L, Toulemon D, Ammar S, Mammeri F (2017) Methods for preparing polymer-decorated single exchange-biased magnetic nanoparticles for application in flexible polymer-based films. Beilstein Journal of Nanotechnology 8: 408-417.
3. Alloyeau D, Ricolleau C, Mottet C, Oikawa T, Langlois C, et al. (2009) Size and shape effects on the order–disorder phase transition in CoPt nanoparticles. Nature Materials 8: 940.
4. Liu Y, Yang Y, Zhang Y, Wang Y, Zhang X, et al. (2013) A facile route to synthesis of CoPt magnetic nanoparticles. Materials Research Bulletin 48: 721-724.
5. Auzans E, Zins D, Blums E, Massart R (1999) Synthesis and properties of Mn-Zn ferrite ferrofluids. Journal of Materials Science 34: 1253-1260.
6. Zaitsev VS, Filimonov DS, Presnyakov IA, Gambino RJ, Chu B (1999) Physical and Chemical Properties of Magnetite and Magnetite-Polymer Nanoparticles and Their Colloidal Dispersions. Journal of Colloid and Interface Science 212: 49-57.
7. Narayanan T, Shaijumon M, Ajayan P, Anantharaman M (2009) Synthesis of High Coercivity Core–Shell Nanorods Based on Nickel and Cobalt and Their Magnetic Properties. Nanoscale Research Letters 5: 164.
8. Joulié M, Laucournet R, Billy E (2014) Hydrometallurgical process for the recovery of high value metals from spent lithium nickel cobalt aluminum oxide based lithium-ion batteries. Journal of Power Sources 247: 551-555.
9. Sun A-C, Yuan F-T, Hsu J-H, Lee HY (2009) Evolution of structure and magnetic properties of sputter-deposited CoPt thin films on MgO(111) substrates: Formation of the L11 phase. Scripta Materialia 61: 713-716.
10. Sobal NS, Ebels U, Möhwald H, Giersig M (2003) Synthesis of Core−Shell PtCo Nanocrystals. The Journal of Physical Chemistry B 107: 7351-7354.
11. Park J-I, Kim MG, Jun Y-w, Lee JS, Lee W-r, et al. (2004) Characterization of Superparamagnetic “Core−Shell” Nanoparticles and Monitoring Their Anisotropic Phase Transition to Ferromagnetic “Solid Solution” Nanoalloys. Journal of the American Chemical Society 126: 9072-9078.
12. Kaya D, Adanur I, Akyol M, Karadag F, Ekicibil A (2019) Physical Properties of CoPt Magnetic Core-Shell Nanoparticles. In: Özcanlı M, Çalık A, editors. 4th International Mediterranean Science and Engineering Congress. Antalya, Turkey. pp. 1265-1268.

Determination of the intrinsic viscosity and molecular weight of Poly (methyl methacrylate) blends

Y. Yigit[1], A. Kilislioglu[2], S. Karakus[2], N. Baydogan[1*]

[1]*Energy Institute, Ayazaga Campus, Maslak, 34469, Istanbul, Turkey*
[2]*Department of Chemistry, Faculty of Engineering, Istanbul University-Cerrahpasa, 34320 Avcilar, Istanbul, Turkey*
Corresponding Author: doganni l@itu.edu.tr*

Abstract

PMMA blends were synthesized through atom transfer radical polymerization (ATRP) method under at different concentration ratios. The viscosity characteristics of the structure were investigated to determine the behaviour of macromolecules in blends. The viscosity characterization of the nanoparticles was determined to explain the molecular structure and interactions. The intrinsic viscosity of the blend was calculated with three different models including Huggins, Kraemer, and Rao. All blends were performed to understand the effect of additives concentration on molecular conformations and the intrinsic viscosity of the polymers. The voluminosity (V_E) and the shape factor (υ) were calculated for the blends to understand the miscibility behaviour. From experimental results, it was observed that the intrinsic viscosity was increased with the increase in the amount of substance and the solubility of the system in solution.

1. Introduction

1.1 Molecular weight

Poly(methyl methacrylate) (PMMA)recognized as plexiglass or acrylic glass [1]. The trade names of PMMA are plexiglas, acrylite and lucite. PMMA has the transparent and thermoplastic properties and generally utilized in sheet form [2]. It is a lightweight choice among the glassy materials [3]. whereas molecules or atoms in crystalline materials are linked to one another in a certain order, polymer materials which can be formed by more than one chain have a random sequence.Polymer materials consist of chains, and these chains may vary in number in terms of the monomer which is the building block of polymers.Therefore, it is not possible to mention a single molecular weight in most of polymer materials. [4].
There are 4 kinds of molecular weight in polymers:

1) **Number Average Molecular Weight(Mn)** which can be expressed briefly in Eq-1: it is obtained by dividing the total molecular weight by the total number of molecules. It is obtained by methods based on the measurement of colligative properties such as freezing point descent, boiling point rise, osmotic pressure, vapor pressure drop.

$$M_n = \frac{\sum_i N_i M_i}{\sum_i N_i} \quad : \qquad (1)$$

where Mi is the molecular weight of a chain, Ni is the number of chains of that molecular weight, and i is the number of polymer molecules [5].

2) **Weight Average Molecular Weight(Mw),** the higher the molecular weight of the molecule, the greater the effect of the molecule on the Weight Average Molecular Weight of the polymer. Unlike first kind of molecular weight, molecules forming polymers do not have the same effect in calculating of molecular weight.It can be calculated in Eq-2:

$$M_w = \frac{\sum_i N_i M_i^2}{\sum_i N_i M_i} \tag{2}$$

where M_i is the molecular weight of a chain, N_i is the number of chains of that molecular weight, and i is the number of polymer molecules[6].

3) **Z-Average Molecular Weight(Mz),**it is an uncommon type of molecular weight. It is obtained by ultracentrifugation method.It is used to determine mechanical properties such as toughness.It can be calculated in Eq-3.

$$M_z = \frac{\sum_i N_i M_i^3}{\sum_i N_i M_i^2} \tag{3}$$

where M_i is the molecular weight of a chain, N_i is the number of chains of that molecular weight, and i is the number of polymer molecules[7].

4) **Viscosity Average Molecular Weight(Mv),** Viscosity is the measure of resistance to flow and the viscosity of the solid materials is calculated by dissolving in a suitable solvent. Mv is briefly calculated in this way: the polymer material is diluted in a suitable solvent in different proportions. So, solutions are obtained at different concentrations. The viscosities of these diluted solutions are calculated, and then the molecular weight of the polymer material is calculated. The relationship between viscosity and molecular weight can be explained as follows. Flowing of large chain polymers is difficult due to entanglement and friction between the chains. That makes the solution ticker and these exhibit higher viscosities.
The intrinsic viscosity, η as function of average molecular weight, M is represented by Mark-Houwink Sakurada equation (in Eq-4).

$$[\eta]=KM^{\alpha} \tag{4}$$

where K and α are empirically determined constants for a given polymer solvent temperature system.
As it can be seen in equation 1-2-3, The distribution of molecular weights in a heterogeneous polymer is that **Mz > Mw >Mv>Mn.** This can be easily applied in Figure 1 [8].

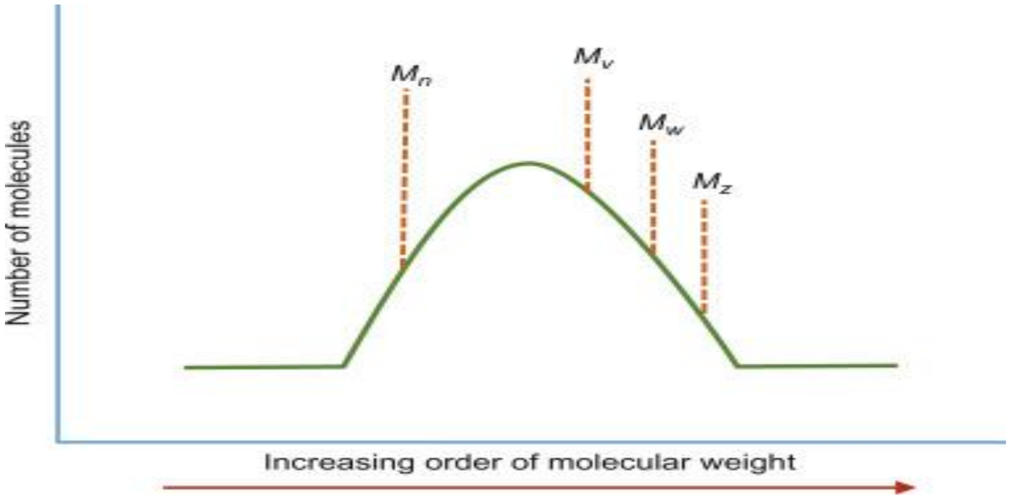

Figure 1. Demonstration of molecular weights in a heterogeneous polymer [8].

1.2 Polydispersity

Monodisperse(some natural polymer)molecular weights of all polymer molecules are same. Polydisperse pronounces for synthetic polymers and the distributed molecules and it is named as Polydispersity Index (PI). It is a measure of heterogeneity within the structure. If PI is 1, then Mw = Mn like some natural polymers. molecular weight is identical in all structure. If PI is more than 1,Mn >Mw and there is heterogeneity within the structure.

One of the most desirable properties of materials used in engineering is the homogeneous structure. As the polydispersity increases, heterogeneity in the structure will increase, and especially mechanical differences will occur within the structure.It must be reduced the heterogeneity of the structure To eliminate these unwanted mechanical differences. In recent years, polymers have been started to produce between 1,0 and 1,2 PI and this rate of heterogeneity has been gradually reduced as molecular weight differences in the structure are requested to be reduced to the minimum level (Figure 2) [9].

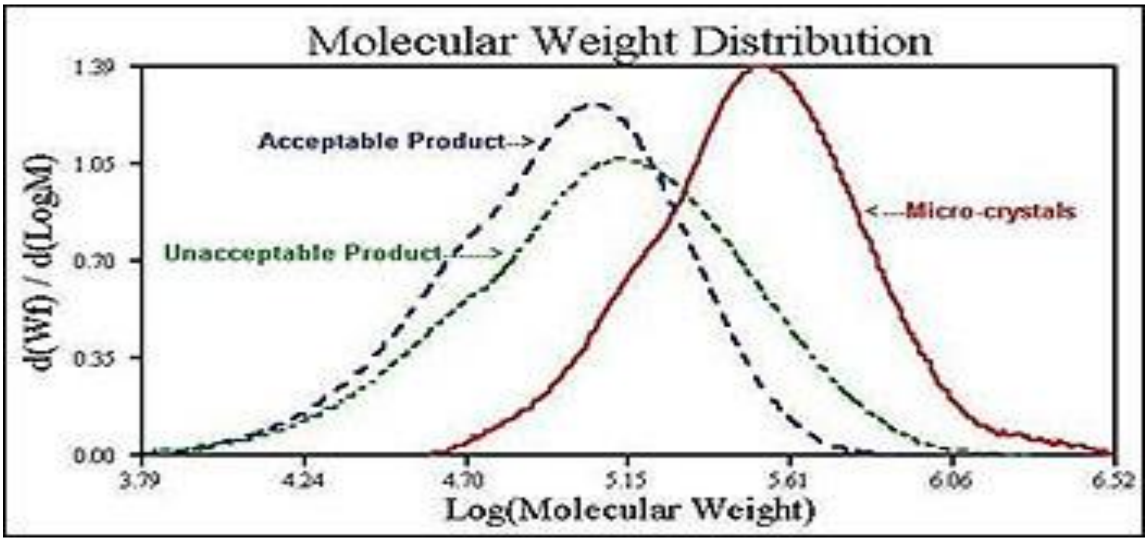

Figure 2. Molecular Weight Distribution [9].

1.3 Relationship between viscosity and mechanical properties

High mechanical values are desirable, however it is observed that it crawl after an approximate value of molecular weight whereas the viscosity exhibits a continuous increase with increasing molecular weight. Since the high viscosity means difficult molding of the material, an optimization is needed between these values. This value of molecular weight is 10000-1000000 g/mol. The above mentioned information is clearly seen in the Figure 3 [10].

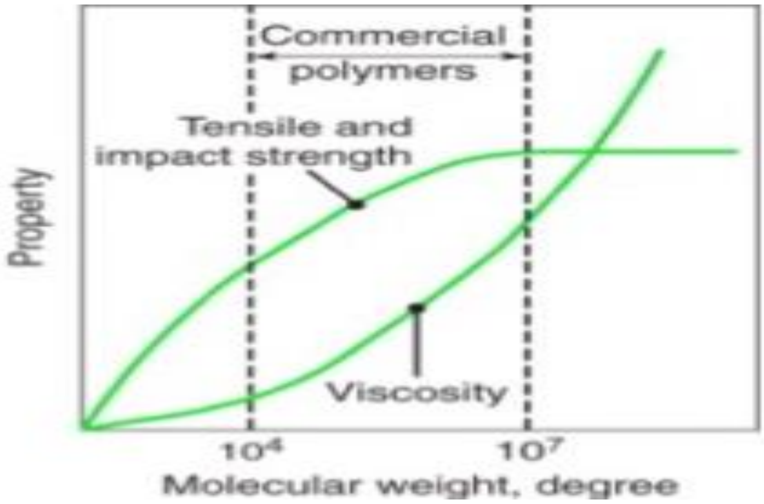

Figure 3. Relationship between viscosity and mechanical properties [10].

2. Experiments

The used chemicals for the synthesis of PMMA produced by ATRP method:

- MMA(C5H802)=50 ml,d=0,939 g/cm3,0,4695 mol
- EBİB(C6H11BrO2) =0,7826 mmol (density=1,329 g/cm3, Vebib= 115,987µl)
- PMDETA(C9H23N3)=0,0004 mol(denstiy =0,830 g/cm3,Vpmdata=164,290 µl)
- Bu4NBr=2,00920 g
- CuBr=0,11176 g

Bu4NBr (Tetra-n-butylammonium Bromide) was used as solvent at the production of PMMA. Bu4NBr concentration was increased double amount in PMMA solution to evaluate the molecular weight variaitons of PMMA by using the maximum amount of the solvent in PMMA solution.

2.1 Measurement of Viscosity for the Determination of Average Molecular Weight

Viscosity average molecular weight test belonging base PMMA by ATRP was performed in the following order to obtain homogeneous solution

Weighing of Polymer Samples by using Sensitive Balance to be Measured Viscosity: The samples (0,1g, 0,3 g, 0,5 g and 0,8 g) belonging base PMMA by ATRP was weighed respectively on the precision scale, whose brand is Radwag AS 220 / C / 2 and whose accuracy is 10^{-4} g .

Preperation of Solvent: 50 ml of toluene was used as solvent in each sample and the used toluene was measured in the measuring cylinder.

Solution Preparation and Measures Taken to Maintain the Amount of Solvent: Measured toluene, PMMAs and magnetic stir bar making the mixture homogeneous are placed in the conical flask. Since toluene is a volatile material, this flask was sealed to be airtight. Any loss in toluene results in a difference between the target concentration and the concentration obtained. This also lead to erroneous results.

The flask was placed on a magnetic stirrer set at 250 revolutions per minute at room temperature to obtain homogeneous solution.

Measuring the Viscosity of the Solution: When the solutions became homogeneous, the flask were taken from the magnetic stirrer and the viscosities of the mixtures were measured by means of a viscometer. The measurements were carried out with AND-SV-10 viscometer. This viscometer has an accuracy with 0.01 cP for the measurements.

When the solutions became homogeneous, the flask were taken from the magnetic stirrer and the viscosities of the mixtures were measured by means of a viscometer. The measurements were carried out with AND-SV-10 viscometer. This viscometer is able to measure with accuracy of 0.01 cP.

Equations and expressions used to measure the viscosity molecular weight of solution: the results were used to obtain relative viscosity and specific viscosity, reduced viscosity, inherent viscosity, intrinsic viscosity. Finally, calculated intrinsic viscosity used in the Mark-Houwink equation. Where η (the intrinsic viscosity), M (Molecular weight) and α, K constants for the particular polymer solvent system. The appropriate solvent for the produce PMMA in this study was toluene and its fixed value was presented in Table 1. The result with viscosimetric molecular weight test was determined and Mark-Houwink equation (Eq-4). η was determined ascut-off point of y axes, k was constant for toluene (0,007 mL/g), α was constant for toluen (0,71) as solvent, M=Avarage Molecular Weight (in Eq 4).

Table 1. Equation constants for various polymer-solvent pairs [15].

Polymer-solvent system	**K x 10^3 mL/g**	**α (Equation constant)**
PMMA-Acetone	7.70	0.700
PMMA-Benzene	5.20	0.760
PMMA-Toluene	***7.00***	***0.710***
Poly vinyl acetate-Acetone	10.20	0.720
Poly vinyl acetate-Benzene	56.30	0.620
Poly vinyl acetate-Acetonitrile	41.50	0.620
Poly vinyl alcohol-Water	45.30	0.640
Poly styrene-Benzene	10.60	0.735
Poly styrene-Toluene	11.00	0.725

The molecular weight of the polymer was measured by using viscometer and the molecular weight called viscosity average molecular weigh tobtained by this technique. The mechanical properties of the polymers which are anisotropic materials can be modified according to the directions, as PMMA molecular weight is livingpolymer. The molecular weight and chain uniformity of the structure will be determined according to $[\eta] = KM^{\alpha}$ (in Eq-4). [η]: intrinsic viscosity, M: molecular weight, K and α are empirically determined constants for a given polymer solvent temperature system, After intrinsic viscosity value was determined by viscometer method, molecular weight was determined [11]. Assesment of intrinsic viscosity [η] was evaluated. For this pupose, the relative viscosity (η_{rel}) (Eq-5)was calculated from the ratio between the flow time of the polymer solution (t) and the flow time of the pure solvent (t_0). Relative viscosity (η_{sp}), [η] and inherent viscosity (η_{inh}) were determined by using Eq. 5-8 [12-14].

Relative viscosity:

$$\eta_{rel} = \frac{t}{t_0} \tag{5}$$

Specificviscosity:

$$\eta_{sp} = \frac{t}{t_0} - 1 = \eta_{rel} - 1 \tag{6}$$

Intrinsic viscosity:

$$[\eta] = \frac{t - t_0}{t_0 * C} = \frac{\eta_{sp}}{C} \tag{7}$$

Inherent viscosity:

$$\eta_{inh} = In\frac{t/t_0}{C} = In\frac{\eta_{rel}}{C} \tag{8}$$

3. Results

Table 2 presents the values to determine the viscosity of the solvent and the solutions at different concentrations. Table 3 shows the viscosities of the solutions at different concentrations used to calculate the instristic viscosity value.

Table 2. Information about base PMMA.

Amount of PMMA (g)	Solvent (Touluen) Amount (ml)	Concentration of Solution (g/ml)	Solvent (Touluen) Viscosity (cP)	Solution Viscosity (cP)
0,1	50	0,002	0,58	0,64
0,3	50	0,006	0,58	0,68
0,5	50	0,01	0,58	0,78
0,8	50	0,016	0,58	0,88

Table 3. Changes in the inherent viscosity of the solutions at different concentrations for base PMMA.

Relative Viscosity (η_r)	Specific Viscosity (η_{sp})	Reduced Viscosity (η_{red})	Inherent Viscosity (η_{inh})
1,103448276	0,103448276	51,72413793	49,22003641
1,172413793	0,172413793	28,73563218	26,51078244
1,344827586	0,344827586	34,48275862	29,62658161
1,517241379	0,517241379	32,32758621	26,05586275

The assesment of intrinsic viscosity for base PMMA was presented in Figure 4. Hence, average molecular weight is determined by using Eq-4. A result of the calculations, the average molecular weight of base PMMA was found to be 274.042 g / mol

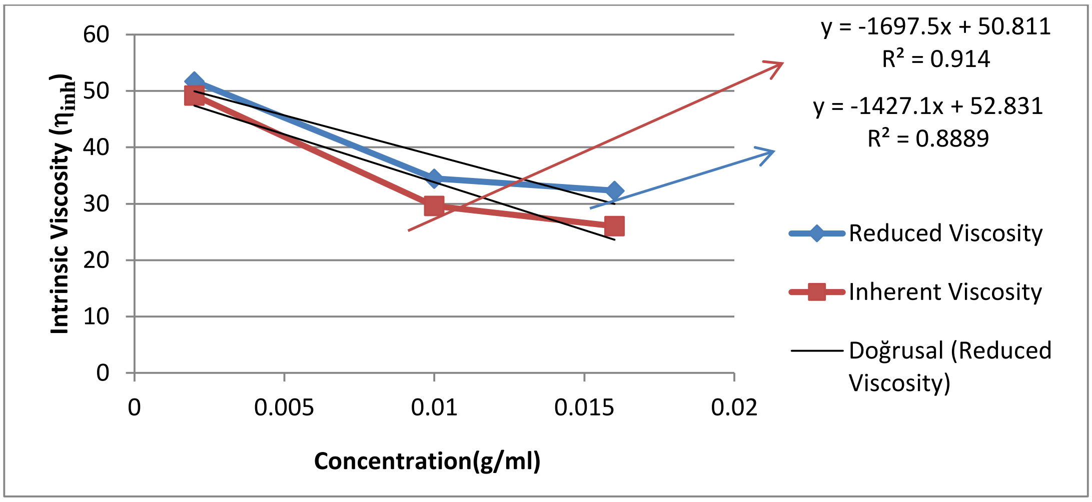

Figure 4. The assesment of intrinsic viscosity of base PMMA

4. Discussions

Synthetic polymers do not consist of the same chains as crystalline atoms or molecules and in them cannot be mentioned a constant molecular weight. In addition to that, the obtained molecular weight values can be influenced by many parameters of production. The molecular weight values of polymer materials are available in a range for several materials in Table 4 [16].

Table 4. Molecular Weight of Various Molecules [16].

Molecules	**cular weight (g/mol)**
Water	18
Alcohol	46
Stearic Acid	384
Polistiren	60.000-100.000
Low Density Polyethylene (LDPE)	30.000-60.000
High Density Polyethylene (HDPE)	30.000-150.000

PMMA synthesized by using different techniques has an average molecular weight in the range of 42.000-130.000. Since, the increase of the value in a controlled manner means improvement of mechanical properties, the average molecular weight was increased by several methods (such as, ATRP, ARGET ATRP). The effect of ATP on molecular weight was clearly examined in Table 5. The average molecular weight of the base PMMA was determined as ~ 270.000 g/mol. The results indicate that the molecular weight has higher than that of industrial PMMAs.

Table 5. Avarage Molecular Weight of base PMMA.

Material	Avarage Molecular Weight (g/mol)
PMMA [17] (by GPC)	120.000
PMMA [18] (PMMA prepared from the block copolymer micelle/homopolymer)	90.000
PMMA [19] (PMMA synthesed by the catalyzed recyclable Ni–Co alloy nanoparticle)	129.500 (Mw/Mn=1,300)
PMMA [20] (ARGET ATRP)	42.500 (PDI=1.36)
PMMA (produced by ATRP method in this study)	274.043

PDI: Polydispersity index.
GPC: A gel permeation chromatography.
ARGET: Activators regenerated by electron transfer.

5. Conclusions

The results of this study indicated that PMMA produced by ATRP method was suitable technique to improve the average molecular weight in this study. PMMA produced by ATRP method named the living polymerization technique has higher the average molecular weight than the molecular weight of the PMMA produced by different techniques in the literature. The molecular weight for the PMMA produced by ATRP method was determined ~270.000 g/mol.

References

1. T. Bel, C. Arslan, N. Baydogan, Materials Chemistry and Physics, 221, p. 58-67 (2019).
2. T. Bel, C. Arslan, N. Baydogan, Journal of the Faculty of Engineering and Architecture of Gazi University, 2018, 18-1 DOI: https://doi.or./ p. 1-18, (2018).
3. T. Bel , H. Cakar , N. Yahya , C. Arslan , N. Baydogan, Defect and Diffusion Forum, 380, p. 227-231, (2017).
4. A. Rudin, Mechanical properties of polymer solids and liquids, in: A. Rudin (Ed.), Elements of Polymer Science and Engineering, second ed., Academic Press, San Diego, 1999, pp. 377_443.
5. M. Chanda, Introduction to Polymer Science and Chemistry: A Problem-Solving Approach, second ed., CRC Press, Boca Raton, FL, 2013, p. 29.
6. L.W. McKeen, Permeability Properties of Plastics and Elastomers, third ed., William Andrew Publishing, Oxford, 2012, pp. 21_37.
7. J.L. Schultz, E.S. Wilks, Nomenclature of Polymers, Encyclopedia of Polymer Science and Technology, Wiley, Hoboken, NJ, 2000.
8. The Effect of Creep and Other Time Related Factors on Plastics and Elastomers (Second Edition), 2009
9. https://www.laboratorynetwork.com/doc/analysis-method-ensures-better-polymer-qualit-0001

10. https://www.chegg.com/homework-help/questions-and-answers/define-molecular-weight-degree-polymerization-graphical-relationship-molecular-weight-poly-q12052059
11. Chuah, H. H., Lin-Vien, D., & Soni, U. (2001). Poly (trimethylene terephthalate) molecular weight and Mark–Houwink equation. Polymer, 42(16), 7137-7139.
12. F. Behrouzian, S. M. Razavi, H. Karazhiyan, Intrinsic viscosity of cress (Lepidium sativum) seed gum: effect of salts and sugars. Food Hydrocolloid. 35 (2014) 100-105.
13. S. M. Razavi, T. M. Moghaddam, B. Emadzadeh, F. Salehi, Dilute solution properties of wild sage (Salvia macrosiphon) seed gum. Food Hydrocoll. 29(1) (2012) 205-210.
14. R. Pamies, J. G. H. Cifre, M. D. C. L. Martínez, J. G. de la Torre, Determination of intrinsic viscosities of macromolecules and nanoparticles. Comparison of single-point and dilution procedures, Colloid Polym. Sci. 286(11) (2008) 1223-1231.
15. https://vlab.amrita.edu/?sub=2&brch=190&sim=603&cnt=1
16. https://www.sciencedirect.com/science/article/pii/0032386177900891?via%3Dihub
17. https://www.sigmaaldrich.com/catalog/product/aldrich/182230?lang=en&region=TR
18. Hyungmin Park, High-throughput preparation of complex multi-scale patterns from block copolymer/homopolymer blend films.
19. Sk Arif Mohammad, Recoverable and recyclable nickel–cobalt magnetic alloy nanoparticle catalyzed reversible deactivation radical polymerization of methyl methacrylate at 25 °C
20. Hyun Jeong Jeon, Synthesis of high molecular weight 3-arm star PMMA by ARGET ATRP

Investigation of superconducting, microstructural and Vickers microhardness properties of $CoFe_2O_4$ doped Y123 superconducting ceramics

O. Ozturk[1], O.Çiçek[1], F. Bulut[2], R. Terzioglu[3], S. Celik[4]

[1]*Kastamonu University, Department of Electrical and Electronics Engineering, 37100 Kastamonu, Turkey*
[2]*Sinop University, Central Research Laboratory 57100 Sinop, Turkey*
[3]*Bolu Abant Izzet Baysal University, Department of Electrical and Electronics Engineering, 14280 Bolu, Turkey*
[4]*Sinop University, Department of Energy Systems Engineering, 57100 Sinop, Turkey*
**Corresponding Author: oozturk@kastamonu.edu.tr*

Different proportions of $CoFe_2O_4$ nanoparticles are substituted with Cu in the Y123 structure produced by classical solid state reaction method ($YBa_2Cu_{3-x}(CoFe_2O_4)_xO_{7-\delta}$, x=0.05 and 0.15). The effects of doping process on the crystal structure were examined by calculating lattice parameters of produced samples by X-ray diffraction (XRD) analysis. The surface morphology and grain orientations of the samples were investigated by scanning electron microscopy (SEM). Vicker's microhardness analysis, was performed by using different loads to the analysis of mechanical properties. The calculated microhardness values were found to increase with the doping ratio. The undoped sample showed Reverse Indentation Size Effect (RISE) behavior, but Indentation Size Effect (ISE) behavior obtained for $CoFe_2O_4$ doped samples. The yield strength and elastic (Young) modulus values were calculated by using the Vickers microhardness test data. In addition, Meyer's law, elastic-plastic deformation (EPD) model and Hays-Kendall (HK) approach were applied to obtain the independent microhardness values.

Keywords: YBCO, Y123, high temperature superconductors, solid state reaction method, $CoFe_2O_4$, Vickers, Meyer's law.

1.Introduction

The YBCO which is a member of high temperature superconductors (HTS) has different phases and each phase has a different critical temperature value. In numerous studies, different elements were added to Y123 phase and their properties were investigated. To use in different technological applications So many features have been investigated such as structural, electrical, mechanical, magnetic and many others [1-5].

The properties of lattice parameters, critical temperature value, magnetic levitation and mechanical properties which vary with the contribution were examined. Investigation of these parameters are important for shaping the material according to the area of use.

Solid state reaction method is one of the most efficient and most preferred methods used in YBCO production. In samples produced using the solid state reaction method, the doping process can increase or decrease the critical temperature value. The additive element and its ratio provide different results. There are also changes in the crystal lattice parameters, magnetic levitation and other properties [6-9].

Some studies examining the effects of the $CoFe_2O_4$ doping in the Y123 phase have shown that the increase in the doping ratio leads to a decrease in the critical temperature value. The changes in lattice parameters and structural defects were examined and it was concluded that Co-Cu and Fe-Cu substitutions caused the decrease in the critical temperature value [10-12].

Slimani et al. [13] discussed the structural changes in mesh parameters and surface morphology in the Y123 system, in which they examined their properties by doping $CoFe_2O_4$ in 2014. In this study, they showed that $CoFe_2O_4$ doping affects the superconductivity properties and the critical temperature value decreases with the increasing of doping ratio. In another study conducted by this group in 2015 [14], the results were similar to the previous study.

In this study, changes in structural and mechanical properties of Cu-($CoFe_2O_4$) substituted Y123 phase were investigated. In addition, different models were used to investigate the mechanical properties.

2.Experimental

Co doped superconducting materials have been prepared by using classical solid state reaction method. For obtaining samples; Y_2O_3 (Yttrium (III) oxide %99.99, purchased from Alfa Aesar), $BaCO_3$ (Barium carbonate %99.95, purchased from Alfa Aesar), CuO (Copper (II) oxide %99.9995, purchased from Alfa Aesar) and $CoFe_2O_4$ (nanopowder, 30 nm particle size (TEM), %99, purchased from Sigma-Aldrich) powders were used. Two different ratios were selected for the doping process (0.05 and 0.15%w) Powders have been grounded for 1 hour in agate mortar to acquire more stable mixing. Samples were calcined 3 times at 850°C for 24 hours in ash furnace. After each calcination powders grounded for 1 hour. Obtained powders were pressed into bulk form (13mm diameter and 2mm thickness). The bulk samples were placed in tube furnace on the alumina crucible for sintering process. Samples sintered at 930°C for 24 hours by heating rate of 5°C/min and then cooled to 500°C in 60 minutes. The samples were kept in the oxygen atmosphere for 5 hours at 500°C. Samples are named as Y123-U, Y123-10 and Y123-15 in accordance with doping ratio.

The XRD analysis of the samples performed by Broker D8 Advance X-ray diffractometer by using CuKα (from 3 to 90^O). Surface morphology investigated by FEI Quanta Feg 250 model scanning electron microscopy. Vicker’s microhardness test performed by using SHIMADZU HMV-2 model microhardness tester. Meyer’s Law, elastic plastic-deformation (EPD) model and Hays-Kendall (HK) approaches applied for obtaining load independent hardness values.

3.Results and discussion

a. Structural analysis

To investigate the crystal structure of samples XRD analysis is one of the important method. The XRD patterns of the samples are represented in Figure 1. In XRD patterns, any peaks which belongs to Co or Fe wasn’t observed. This shows that the doping elements are introduced into the Y123 structure. Some peaks intensities were changed by Co^{+3} and Fe^{+2} ions which introduced in structure, but that didn't corrupt the orthorhombic structure.

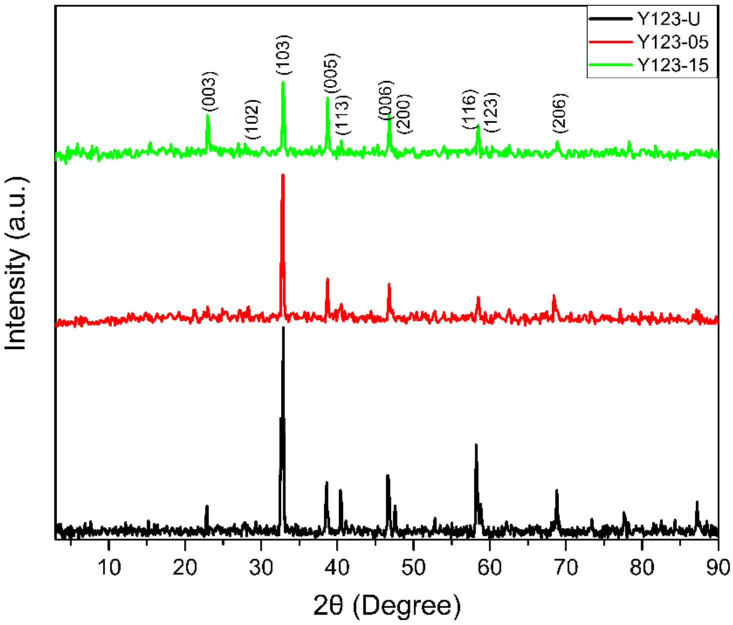

Figure 1: XRD patterns and miller indices of produced samples

Table 1. Lattice parameters and particle size values

Sample	*Grain Size (Å)*	*a (Å)*	*b (Å)*	*c (Å)*
Y123-U	28.95	3.815	3.882	11.683
Y123-05	30.16	3.821	3.872	11.633
Y123-15	32.73	3.826	3.873	11.631

Since Y123 is an orthorhombic structure; d the distance between the planes and the data such as the a, b, and c parameters were calculated by formula,

$$\frac{1}{d^2} = \frac{h^2}{a^2} + \frac{k^2}{b^2} + \frac{l^2}{c^2} \qquad (1)$$

using the indices h, k, l from the XRD. Grain size, D, calculated using formulas

$$D = 0.941\lambda / B\cos\theta \qquad (2)$$

$$B^2 = B_s^2 - B_m^2 \qquad (3)$$

here B_s indicates the FWHM (full width half of maximum) and B_m is 0,000007 [9].

The lattice parameters of Y123 structure are given in the literature as a=3.82Å, b=3.89Å and c=11.7Å respectively. It is seen that the lattice parameters of Y123 for superconducting samples with $CoFe_2O_4$ doping produced by classical solid state reaction method are in accordance with the literature. The grain size values given in Table 1 show that the particle size increases with the increase of $CoFe_2O_4$ doping.

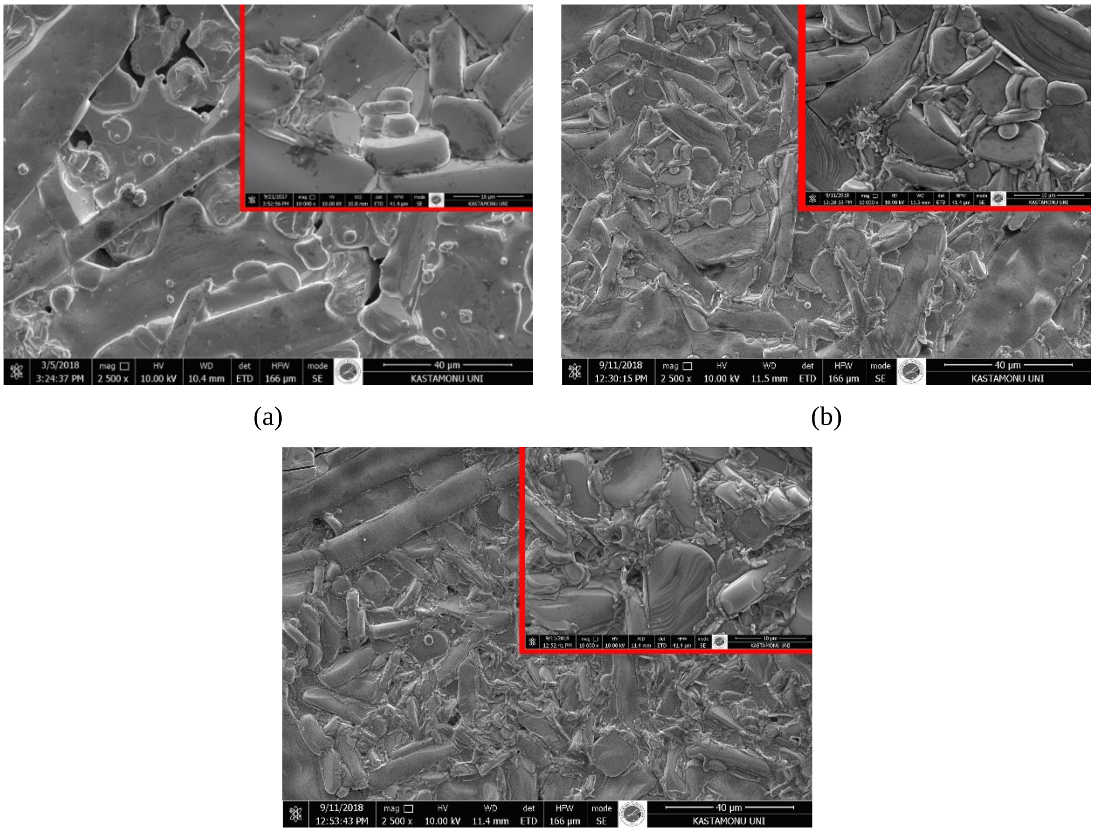

(a)

(b)

(c)

Figure 2. SEM images of $CoFe_2O_4$ doped samples produced by solid state reaction method (a; Y123-U, b; Y123-05, c; Y123-15)

SEM analysis was performed to determine the particle boundaries, inter-particle distance and particle size of $CoFe_2O_4$ doped samples obtained by solid state reaction method. In Figure 2 large images were taken at 2500 magnification, while internal pictures were taken at 10000 magnifications. From the SEM images, it is seen that the particle sizes increase with $CoFe_2O_4$ contribution. This change is in agreement with the particle size values calculated by XRD results. The variation of particle boundaries and inter-particle distance is clearly seen in Figure 2. In addition, the increased particle size with the doping also led to a decrease in porosity.

b. Microhardness and modelling

It is important that investigate mechanical properties of superconductors such as hardness, yield stress and elastic modulus for possible technological applications. Vickers microhardness test is one of the useful method to investigate the mechanical properties of bulk samples [15].

Hardness defines as the resistance of the material to the applied load on surface. Production process of material can effect the sample hardness [16].

In the Vickers microhardness test, the formula,

$$H_V = 1854.4\left(\frac{F}{d^2}\right) \tag{4}$$

is used to calculate the hardness value. The constant value in this formula comes from the top angle of the pyramid tip. Here, F is the load applied to the surface (F= 0.245, 0.490, 0.980, 1.960 and 2.940N), and d is the average of the diagonal lengths of the indenter tip that is left on the material surface.

Elastic modulus (E) and yield stress (Y) values of samples have been calculated by using hardness values obtained from Vickers microhardness test and using empirical formulas,

$$E = 81.9635\, H_V \tag{5}$$

$$Y \approx H_V/3 \tag{6}$$

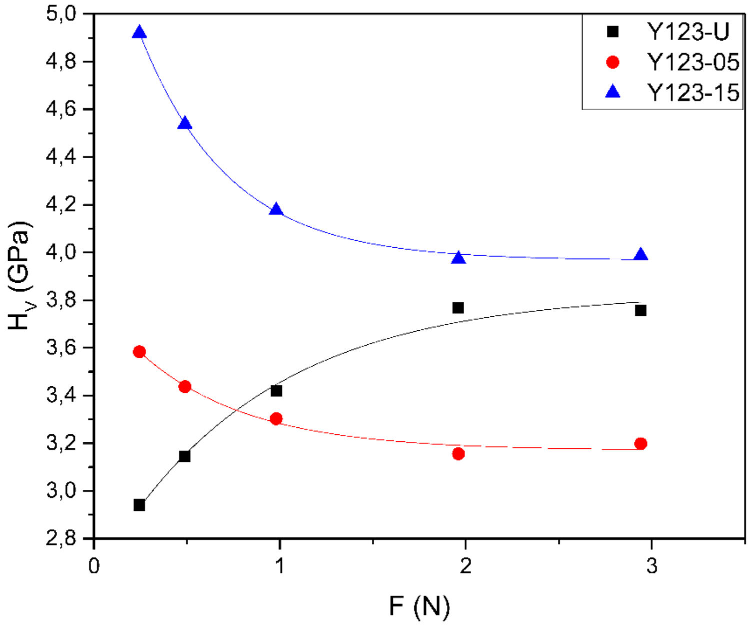

Figure 4. Microhardnes graph of produced samples

The hardness graph of the samples produced obtained from the Vickers microhardness test is given in Figure 4. In the literature, while the behavior of undoped sample is called as Reverse Indentation Size Effect (RISE), doped samples behavior Indentation Size Effect (ISE). In Figure 4, the plateau region of microhardness results decreased with 0.05% doping ration but increased with increasing of doping ratio to 0.15%. Elastic modulus (E) and yield stress (Y) values of samples are calculated and all results are given in Table 2.

Tablo 2. Some calculated parameters of $CoFe_2O_4$ doped samples produced by solid state reaction method

Sample	F (N)	H_V (GPa)	E (GPa)	Y (GPa)
Y123-U	0.245	2.881	236.15	0.960
	0.490	3.143	257.63	1.048
	0.980	3.420	280.28	1.140
	1.960	3.768	308.80	1.256
	2.940	3.755	307.80	1.252
Y123-05	0.245	3.583	293.706	1.194
	0.490	3.437	281.695	1.146
	0.980	3.302	270.670	1.101
	1.960	3.155	258.617	1.052
	2.940	3.198	262.109	1.066
Y123-15	0.245	4.920	403.221	1.640
	0.490	4.538	371.969	1.513
	0.980	4.176	342.311	1.392
	1.960	3.972	325.559	1.324
	2.940	3.902	319.810	1.301

Meyer's law

This is the simple model and usually used to describe the Indentation Size Effect (ISE) behavior. In this method, which is a simple expression between applied force (F) and average diameter of trace (d), the formula

$$F = Ad^n \tag{7}$$

is used. In this formula, Meyer number (n) is the slope of the lnF-lnd graph (Figure 5). Meyer number describes the sample behavior. If the number n is less than 2; sample exhibits ISE behavior, but when n is more than 2 sample exhibits RISE behavior. A describes as the standard hardness constant [15, 16]. Data obtained for this model are given in Table 3.

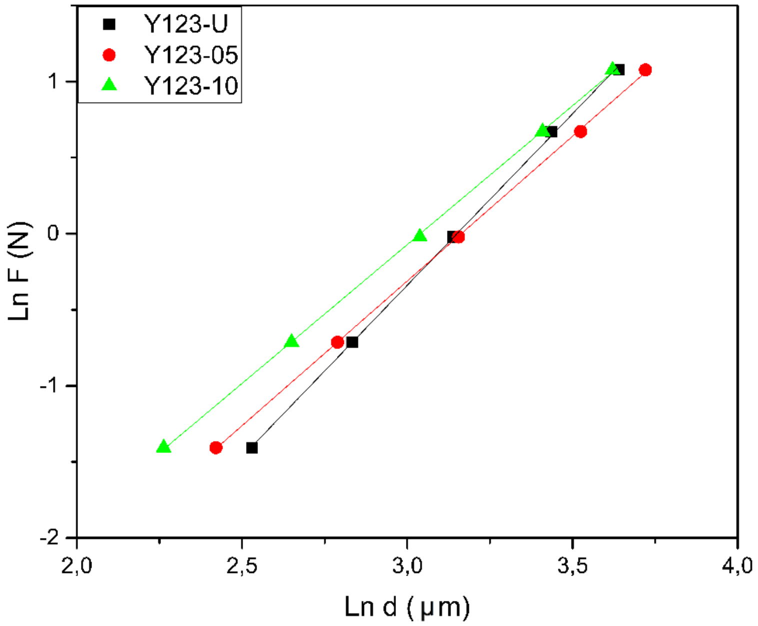

Figure 5. lnF–lnd graph for the samples produced

Table 3. Fit results of data according to Meyer's law

Samples	n	lnA (GPa)	Hv (GPa)
Y123-U	2.26	-7.10	3.420-3.755
Y123-05	1.90	-6.02	3.302-3.198
Y123-15	1.83	-5.55	4.176-3.902

From Table 2, while n>2 obtained for undoped sample with RISE behavior, n<2 obtained for doped samples with ISE behavior.

Elastic-plastic deformation (EPD) model

EPD model is one another model to explain ISE behavior of the samples. [17, 18]. In this model, the load dependence of the indentation size is calculated by the formula,

$$F = A_2\left(d_e + d_p\right)^2 \tag{8}$$

Here, d_p is related with plastic deformation, d_e is related with elastic deformation and A_2 describes as independent hardness constant. By using $F^{1/2}$–d_p graph, A_2 and d_e parameters can obtain. Figure 6 represents the $F^{1/2}$–d_p graph.

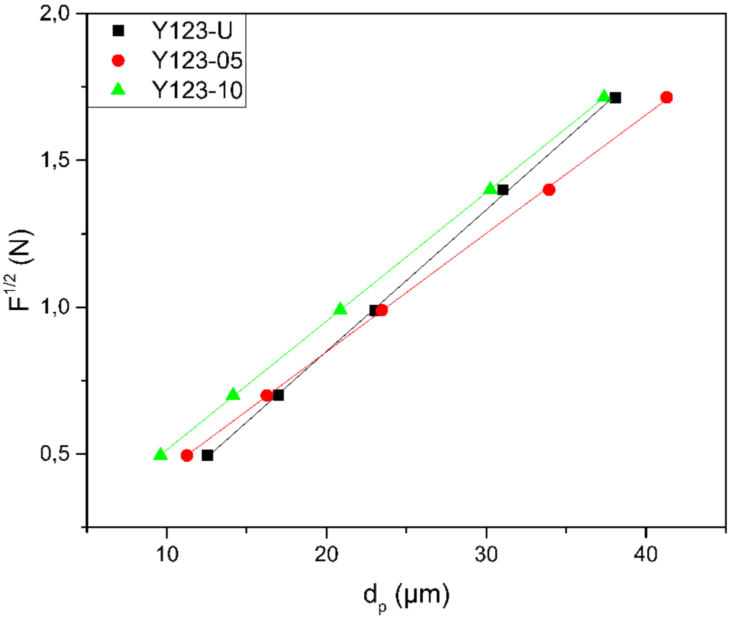

Figure 6. $F^{1/2}$–d_p graph of the samples

In elastic-plastic deformation model the load independent hardness values calculate by following formula,

$$H_{EPD} = 1854.4A_2 \qquad (9)$$

Calculated data are presented in Table 4 for EPD model. d_e is found to be negative for undoped sample and positive for doped samples. Negative d_e means there is no elastic deformation in the material, so we can say for undoped sample did not represent any plastic recovery. By doping, samples gain elastic recovery.

Table 4. Fit results of data according to EPD model

Samples	d_e (µm)	A_2 (N/µm2)	$H_{V(EPD)}$ (GPa)	H_V (GPa)
Y123-U	-0.115	0.00233	4.313	3.420-3.755
Y123-05	0.041	0.00163	3.021	3.302-3.198
Y123-15	0.076	0.00192	3.558	4.176-3.902

Hays-Kendall approach (HK)

In this approach, it is suggested that, to create permanent deformation, the minimum load value (W) is required. The permanent deformation will not occur and only elastic deformation will occur, if the load applied to the surface does not exceed W value, [19].

$$F - W_{HK} = A_{HK}d^2 \qquad (10)$$

Here, A_{HK} is load independent hardness constant. All values are obtained from F–d^2 graph (Figure 7). In this model, the formula,

$$H_{HK} = 1854.4A_{HK} \qquad (11)$$

is used to calculate the load-independent hardness value.

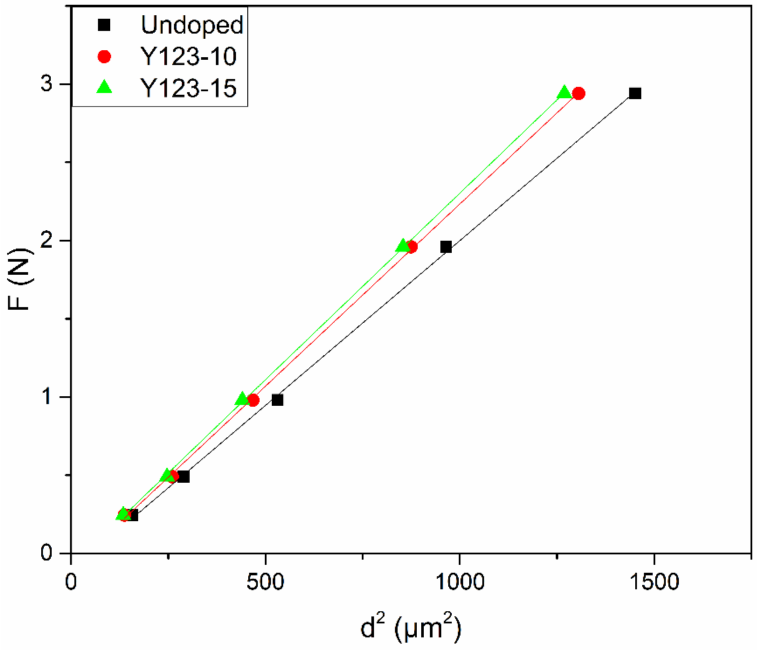

Figure 7. F–d^2 graph of the samples

Table 5 shows the values obtained for HK approach. When data in the table are examined, it is seen that W value is negative for undoped sample, but positive for doped samples. This shows that undoped sample exhibit RISE behavior while doped samples exhibit ISE behavior. This finding supports by the literature [20]. The positive value indicates that there is plastic deformation in the materials as well as elastic deformation. If we compared with the results obtained from the other models, the independent microhardness values determined with regard to HK approach gives closer results to saturation region.

Table 5. Fit results of data according to HK approach

Samples	W(N)	Ax10^{-3}	H_{HK} (GPa)	Hv (GPa)
Y123-U	-0.107	2.107	3.907	3.420-3.755
Y123-05	0.035	1.696	3.144	3.302-3.198
Y123-15	0.072	2.058	3.816	4.176-3.902

Conclusion

In the study, $CoFe_2O_4$ doped YBCO123 samples are produced by solid state reaction method. XRD, SEM and Vickers microhardness measurements are performed for all samples and structural, morphologic and mechanical properties were investigated.

In the XRD results, it was observed that the peaks intensities decreased by increasing of doping ratio. It is predicted that this may be due to the tendency to disrupt the orthorhombic structure. In addition, the decrease in peak intensity with the doping indicates that the crystallinity has deteriorated. From the SEM images it was observed that, surface morphology changed with doping. Increasing of doping ratio decreased the porosity of the samples surface.

The mechanical behavior of the samples was examined by microhardness analysis. It is common in the literature that the undoped sample showing RISE behavior becomes ISE behavior with the additive. This may be a result of the convergence of the particles with decreasing porosity. Experimentally obtained microhardness values were examined theoretically. As a result of these investigations, it was concluded that the HK approach is the most appropriate model for explaining ISE behavior of the doped samples.

References

1. Supadanaison, R., Panklang, T., Wanichayanan, C., Kaewkao, A., Nilkamjon, T., & Udomsamuthirun, P. et al. (2018). Determination of Cu 2+ and Cu 3+ by titration in Y134 and Y145 superconductor. Materials Today: Proceedings, 5(7), 14896-14900. doi: 10.1016/j.matpr.2018.04.026

2. Matskevich, N., & Wolf, T. (2014). Thermochemical investigation of YBa2Cu3O7−δ superconductor doped by lutetium. Journal Of Alloys And Compounds, 614, 415-419. doi: 10.1016/j.jallcom.2014.06.125

3. Dihom, M., Shaari, A., Baqiah, H., Al-Hada, N., Kien, C., & Azis, R. et al. (2017). Microstructure and superconducting properties of Ca substituted Y(Ba1−Ca)2Cu3O7−δ ceramics prepared by thermal treatment method. Results In Physics, 7, 407-412. doi: 10.1016/j.rinp.2016.11.067

4. Ramli, A., Shaari, A., Baqiah, H., Kean, C., Kechik, M., & Talib, Z. (2016). Role of Nd2O3 nanoparticles addition on microstructural and superconducting properties of YBa2Cu3O7-δ ceramics. Journal Of Rare Earths, 34(9), 895-900. doi: 10.1016/s1002-0721(16)60112-6

5. Kurnaz, S., Çakır, B., & Aydıner, A. (2017). The effect of growth temperature on the irreversibility line of MPMG YBCO bulk with Y 2 O 3 layer. Cryogenics, 85, 51-57. doi: 10.1016/j.cryogenics.2017.05.010

6. Guner, S., Gorur, O., Celik, S., Dogruer, M., Yildirim, G., Varilci, A., & Terzioglu, C. (2019). Effect of zirconium diffusion on the microstructural and superconducting properties of YBa2Cu3O7−δ superconductors.

7. Yilmaz, M., & Dogan, O. (2012). Structural and superconducting properties in Y0.6Gd0.4Ba2(Nb)Cu3O7−y cuprates doped with niobium. Journal Of Rare Earths, 30(3), 241-244. doi: 10.1016/s1002-0721(12)60031-3

8. Khalid, N., Kechik, M., Baharuddin, N., Kien, C., Baqiah, H., & Yusuf, N. et al. (2018). Impact of carbon nanotubes addition on transport and superconducting properties of YBa 2 Cu 3 O 7−δ ceramics. Ceramics International, 44(8), 9568-9573. doi: 10.1016/j.ceramint.2018.02.178

9. Pimentel, J., Buitrago, D., Supelano, I., Parra Vargas, C., Mesquita, F., & Pureur, P. (2014). Synthesis and Characterization of the Superconductors Y3Ba5Cu8−x Fe x O18(0.0597 ≤ x ≤ 0.1255). Journal Of Superconductivity And Novel Magnetism, 28(2), 509-512. doi: 10.1007/s10948-014-2742-6

10. Liu, L., Dong, C., Zhang, J., & Li, J. (2002). The microstructure study of Co-doped YBCO system. Physica C: Superconductivity, 377(3), 348-356. doi: 10.1016/s0921-4534(01)01286-2

11. Boudjema, E., Mahtali, M., Chamekh, S., & Taoufik, A. (2010). The effect of Ca co-substitution in (Y1−xCax)Ba2 (Cu0.98Co0.02)3O7−δ (0 ≤ x ≤ 0.35) ceramic. Surface And Interface Analysis, 42(6-7), 996-999. doi: 10.1002/sia.3466

12. Andersen, N., Andersen, J., Börjesson, L., Hadfield, R., Kakihana, M., & McGreevy, R. et al. (1993). Structure and superconductivity in Co doped YBa2Cu3O6+x. Journal Of Alloys And Compounds, 195, 327-330. doi: 10.1016/0925-8388(93)90749-d

13. Slimani, Y., Hannachi, E., Ben Salem, M.K., Hamrita, A., Varilci, A., Dachraoui, W., Ben Salem, M., Ben Azzouz, F., (2014). Comparative study of nano-sized particles CoFe2O4 effects on superconducting properties of Y-123 and Y-358. Physica B, 450, 7–15.

14. Slimani, Y., Hannachi, E., Ben Salem, M.K., Hamrita, A., Ben Salem, M., Ben Azzouz, F., (2015). Excess Conductivity Study in Nano-CoFe2O4-Added YBa2Cu3O7−d and Y3Ba5Cu8O18±x Superconductors. Journal of Superconductivity and Novel Magnetism, 28(10), 3001–3010.

15. Ozturk, O., Erdem, M., Asikuzun, E., Yildiz, O., Yildirim, G., Varilci, A., & Terzioglu, C. (2012). Investigation of indentation size effect (ISE) and micro-mechanical properties of Lu added Bi2Sr2CaCu2Oy ceramic superconductors. Journal Of Materials Science: Materials In Electronics, 24(1), 230-238. doi: 10.1007/s10854-012-0722-9

16. Safran, S., Kılıç, A., Kılıçarslan, E., Ozturk, H., Alp, M., Asikuzun, E., & Ozturk, O. (2015). Mechanical, microstructural and magnetic properties of the bulk BSCCO superconductor prepared by two different methods. Journal Of Materials Science: Materials In Electronics, 26(4), 2622-2628. doi: 10.1007/s10854-015-2733-9

17. Kucukomeroglu, T., Bacaksiz, E., Terzioglu, C., & Varilci, A. (2008). Influence of fluorine doping on structural, electrical and optical properties of spray pyrolysis ZnS films. Thin Solid Films, 516(10), 2913-2916. doi:10.1016/j.tsf.2007.05.075

18. Biju, A., Sarun, P., Aloysius, R., & Syamaprasad, U. (2008). Flux pinning properties of Yb substituted (Bi,Pb)-2212 superconductor. Journal of Alloys and Compounds, 454(1-2), 46-51. doi:10.1016/j.jallcom.2006.12.100

19. Ozturk, O., Asikuzun, E., Tasci, A.T. et al. J Mater Sci: Mater Electron (2018) 29: 3957. https://doi.org/10.1007/s10854-017-8336-x
20. Turkoz, M. B., Nezir, S., Ozturk, O., Asikuzun, E., Yildirim, G., Terzioglu, C., & Varilci, A. (2013). Experimental and theoretical approaches on mechanical evaluation of Y123 system by Lu addition. Journal of Materials Science: Materials in Electronics, 24(7), 2414-2421. Doi:10.1007/s1085

Carbon based films with extraordinary properties

R.Esen, W.Abusaid and B.Ozkan
Physics Dept. Univ. of Çukurova Adana/Turkey

Abstract

In this work we present some carbon based films obtained from ECR plasma decomposition of methane and graphitic carbon films obtained by cathodic vacuum arc deposition method. The films produced by ECR plasma using methane gas as a starting material showed a definite transmission window near 320 nm which is an unusual property one expects more absorption as wavelength decreases.

Second group of unusual optical property is observed at carbon nanowalls obtained by pulsed vacuum arc deposition method using graphite as starting material.

Keywords: ECR, PVACD, Carbon nanowall, SiC, DLC.

1. Inroduction:

Main Process for Carbon Coating

During the last decades, the methods of carbon coating have increased significantly. Coating processes and deposition technologies are changing rapidly to keep pace with developed film materials and applications.('New developments and applications in chemical reaction engineering' 2007). Figure 1 summarizes the classification of coating process.

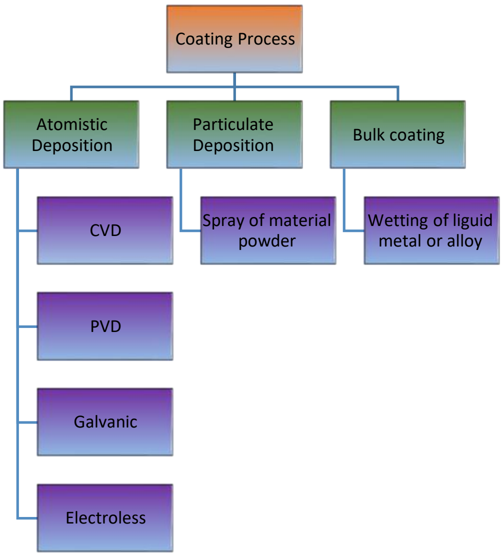

Figure 1 summarizes the classification of coating process

2.Experimental results

We used ECR (Electron Cyclotron Resonance) plasma system with ultrapure methane gas as a starting material. **Major Components of ECR Plasma Sources**

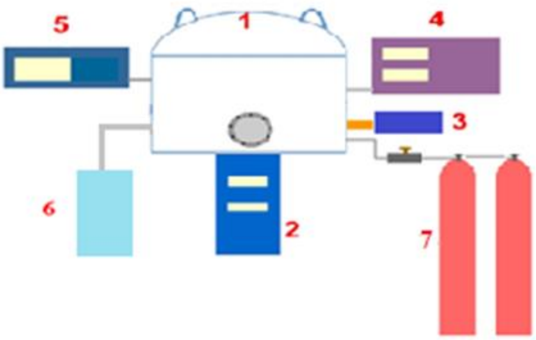

Figure 2. A schematic diagram of ECR-CVD system

ECR system consists of the following basic components:

ECR system consists of the following basic components:

1. Reaction chamber
2. turbo molecular pump and rotary pump
3. Plazma source
4. Microwave source and extraction voltage source
5. Gas flow indicator
6. Cooling Unit
7. Nitrogen Tube
8. Methane Tubes

With this system at room temperature 10^{-3} Torr pressure 3-5 cm separation with ion source and substrate (soda lime glass microscope slide) we produce carbon films and measure their optical transmission with a spectrometer and present the result below graphic.

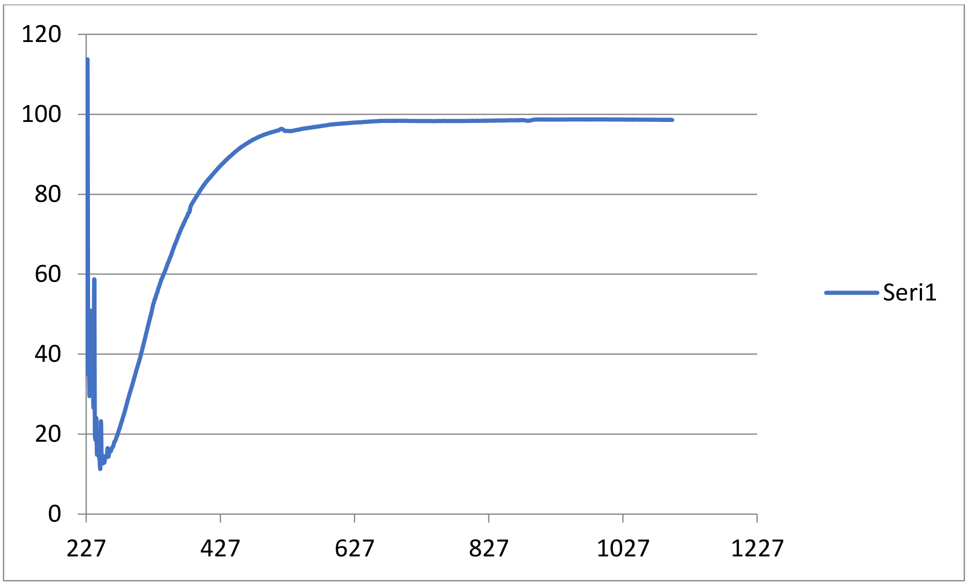

Figure 3. Unusual optical transmission of a carbon film.

Here one expects transmission to have smaller values as wavelength decreases. But for this group of samples we observed that unstochiometric silicon carbide film produced instead of DLC (diamond like carbon) film. We backed our proposal with Raman analysis. This property diminishes as film thickness takes higher values than 300 nm.

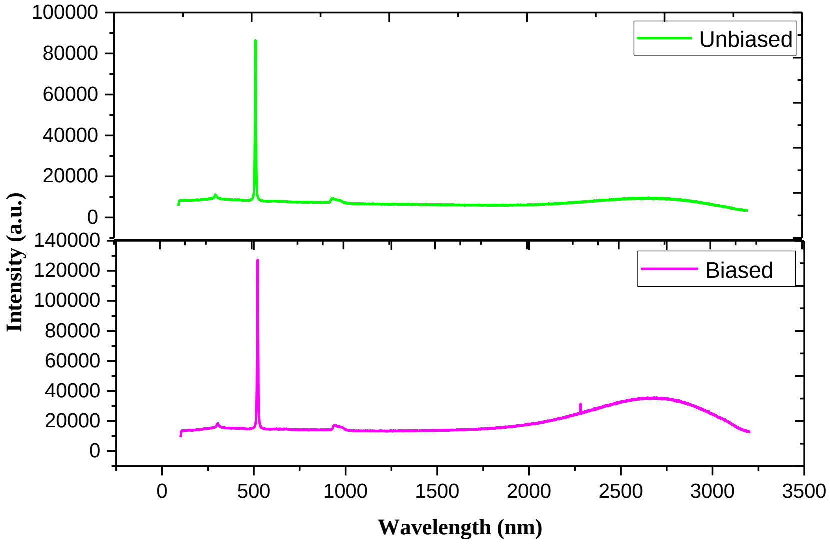

Figure 4. SiC films produced on top of crystalline silicon.

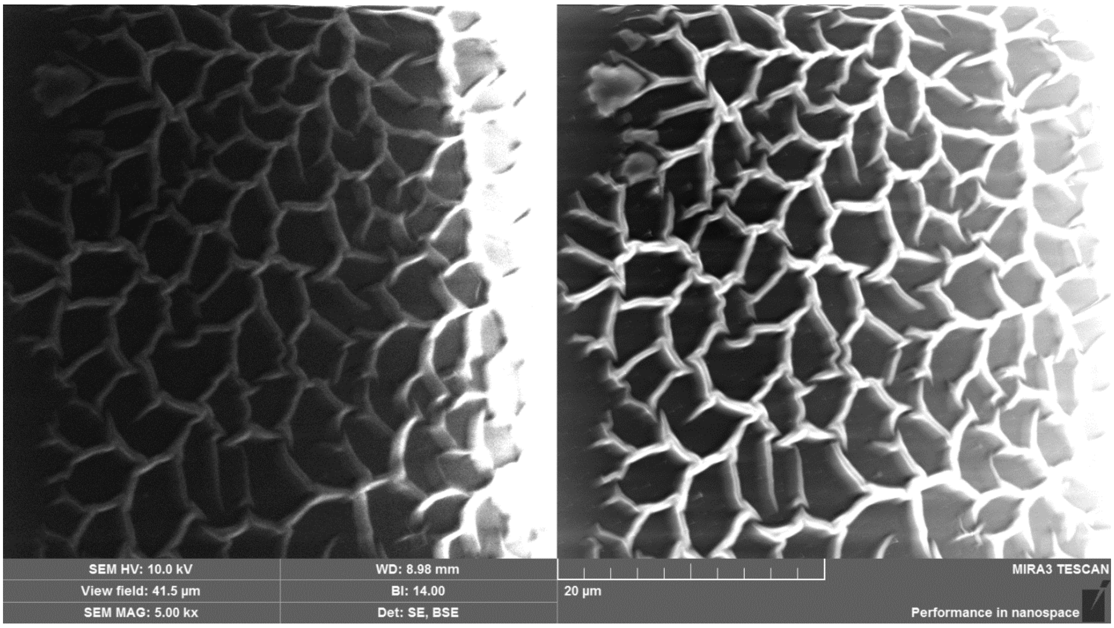

Figure 5. Carbon nanowalls produced by PVCAD technique

These group of films showed a blackbody type reflection at 400-700 nm interval. Which is a perfect absorber and reflection value is lowered by multiple reflections on the walls.

Acknowledgement: This work supported by C.U. BAP project FBA-2019-12021.

REFERENCES

[1] M. S. and Dresselhaus, "G. Intercalation compounds of graphite," Advanced Physics, volume 51, pp. 1-186, 2002.

[2] K. S. et al, Novoselov, "Electric field effect in atomically thin carbon films," Science, volume 306, pp. 666-669, 2004.

[3] C. et al, Berger, "Electronic confinement and coherence in patterned epitaxial grapheme, "Science, volume 312, pp. 1191-1196, 2006.

[4]D. Muller, Li, M. B., Gilje, S., Kaner, R. B. and Wallace G. G, "Processable aqueous dispersions of graphene nanosheets," Nature Nanotech, volume 3, pp. 101-105, 2008.

[5] Geim, A. K. & Novoselov, K. S. "The rise of graphene," Nature Mater, volume 6, pp. 183-191, 2007.

[6] M. I. Katsnelson, "Graphene: Carbon in Two Dimensions," Materials Today, volume 10, pp. 1-2, 2007.

[7] A. Yoshimura, S. Kurita, M. Tachibana, K. Kojima, P. Molina-Morales and H. Nakai, "Fabrication of Carbon Nanowalls by DC Plasma Enhanced Chemical Vapor

Deposition and Characterization of Their Structures," Proceedings. 5th IEEE Conference. on Nanotechnology, Nagoya, 2005

[8] K. Jurewicz, E. Frackowiak, F. Beguin, "Towards the Mechanism of Electrochemical Hydrogen Storage in Nanostructured Carbon Materials," Applied Physics, volume 78, pp. 981-987, 2004.

[9] J. Geng, H. Li, V. B. Golovko, D. S. Shephard, D. A. Jefferson, and B. F. G. Johnson, "Nickel Formate Route to the Growth of Carbon Nanotubes," J. Phys. Chem. B,volume 108, pp. 18446-18450, 2004.

[10] C. Yu, S. C.Wang, M. Sosnowski and Z. Iqbal, "Plasma Enhanced Chemical Vapor Deposition of Polyperinephtalene Thin Films," Synthetic Metals, pp. 1, 2008.

[11] M. Hori, M. Hiramatsu, K. Shiji and H. Amano, "Fabrication of Vertically Aligned Carbon Nanowalls using Capacitively Coupled Plasma Enhanced Chemical Vapor Deposition Assisted by Hydrogen Radical Injection," Applied Physics Letters,volume 84, number 23, pp. 1-3, 2004.

[12] Z. H. Ni, H. M. Fan, Y. P. Feng, Z. X. Shen, B. J. Yang, and Y. H. Wu "Raman spectroscopic investigation of carbon nanowalls," Journal of Chemical Physics, volume 124, pp. 204703, 2006

Electrochemical hydrogen production by using G/Ni/Ag cathode

R. Yıldız[1], B. Doğru Mert[2], S. Toprak Döşlü[1]

[1]*Mardin Artuklu University, School of Health, 47200,Mardin, Turkey*

[2]*Adana Alparslan Turkes Science and Technology University, Dept. of Energy Systems Engineering, 01250, Adana, Turkey*

Corresponding Author: ryildiz80@gmail.com

In this study graphite (G) electrode was coated with nickel and decorated with silver (G/Ni/Ag) and we used this modified electrode as cathode in alkaline water electrolysis system. The electrochemical characterization of G, G/Ni and G/Ni/Ag was achieved via cyclic voltammetry technique. Hydrogen evolution performance of electrodes was investigated via chronoamperomety, cathodic polarization curves and electrochemical impedance measurements. Results showed that hydrogen production efficiency significantly increased and charge transfer resistance of electrodes decreased via Ni/Ag multilayer.

Keywords: Hydrogen production, Alkaline electrolysis, G/Ni/Ag cathode

1. Introduction

The demand for energy increases all around the world, day by day with the help of increasing industrial consumption and increasing the world population which means personal consumption. We need an alternative, renewable and sustainable energy sources. In order to decrease CO_2 emission, hydrogen is a suitable and alternative fuel for us. We have many alternative hydrogen production methods such as thermochemical processes (ie; steam methane reforming, coal gasification, biomass gasification etc.), direct solar water splitting processes, biological processes (from bacteria and microalgae), alkaline water electrolysis, etc. [1]-[13]. The alkaline water electrolysis is a simple technique and we can produce pure hydrogen on cathode of this system. In alkaline electrolysis systems, the main handicap is over potential values of electrode materials. Researchers have achieved many studies in order to diminish over potential values of electrodes. Results showed that Ni based cathode materials have tremendous advantages because of higher conductivity and lower overpotential values [14, 15]. Yuvaraj et al. [16] used graphite cathode and investigated the influence of electrolyte concentration, temperature, voltage and reaction time on the amount of hydrogen gas produced. The applied voltage was varied from 4.5 to 12 V. Results showed that graphite cathode produced 75 mL $H_{2(g)}$ at 10 V during 600 s in 0.03 M KOH. Koca et al. [17] deposited nickel Ni and low amount of gallium (Ga) on carbon felt electrodes (CF/Ni and CF/NiGa) and they determined hydrogen evolution performance in 1 M KOH. They declared that Ni modification decreased overpotential value of CF cathode and hydrogen production performance was enhanced via Ga. The CF/NiGa electrode produced 28.9 mL $H_{2(g)}$ in 1 M KOH for 30 min. Döner et al. [18] coated graphite electrode with CoZn-Pt coating which had a rough structure and presented good stability and high durability as cathode during alkaline electrolysis. The cathodic Tafel constant of G/CoZn-Pt was varied from 149 to 171 mV/dec during long term stability tests.

In this study, 10 μm Ni coating deposited galvanostatically on graphite rod electrode then 10 μg cm^{-2} Ag decorated on the surface, it (G/Ni/Ag electrode) was used as cathode material in

25% KOH solution for hydrogen production.

2. Methods and Materials

A cylindrical graphite rod with a 0.5 cm diameter used as a working electrode. Before electrodeposition treatments, the surface of electrode was abraded by emery paper down to 1200 grade. Then, it was washed by acetone/ethanol mixture and pure water. The electrodeposition of nickel and silver was performed by galvanostatically using Iviumstat Electrochemical Interface with a three-electrode configuration. In this system, graphite was used as working electrode, nickel as counter electrode and an Ag/AgCl (3 M KCl) electrode was used as the reference electrode. The nickel deposition bath composition was 30% $NiSO_4.7H_2O$, 1% $NiCl_2.6H_2O$, 1.25% H_3BO_3 deposition current density is 10 mA cm^{-2}. The silver deposition bath is 0.75 mM and deposition current density is 0.25 mA cm^{-2}. The electrochemical measurements were carried by using CHI 660D A.C. electrochemical analyzer at room temperature, open to atmosphere. A platinum sheet (with 2 cm^2 surface area) was used as the counter electrode and Ag/AgCl (3 M KCl) electrode was used as the reference electrode for electrochemical analysis such as cathodic polarization curves, cyclic voltammetry and impedance measurements. The electrolyte in all measurements was 25% M KOH aqueous solution. The cyclic voltammetry measurements were obtained in the potential ranges between −1.4 V and 0.8 V (vs. Ag/AgCl) with a scan rate of 0.1 V s^{-1}. The chronoamperometric measurements were employed at -1.3 V (vs. Ag/AgCl). The polarization curves were obtained with a scan rate of 0.001 Vs^{-1}. The EIS experiments were conducted in the frequency range with a high limit of 100 kHz and the low limit of 0.01 Hz. The amplitude was 0.005 V. The EIS results were presented using a Zview software.

3. Results and discussion

The cyclic voltammograms of G, G/Ni and G/Ni/Ag were presented in Fig. 1. The measurement presents information not only about the characterization of electrochemically deposited metallic coatings but also gives information about HER activity of electrodes when we compare the initial part of the cathodic potential region [19].

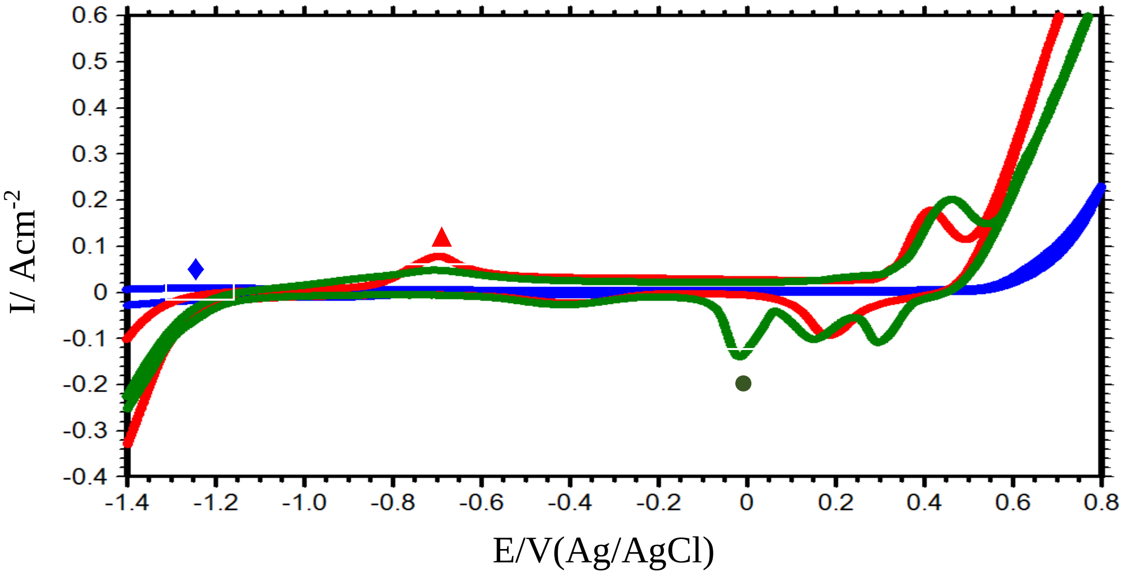

Fig. 1: *The cyclic voltammograms of G (♦), G/Ni (▲) and G/Ni/Ag(●) in KOH solution.*

As seen in Fig. 1. There was no significant peak detected for G until 0.6 V during forward scan and during a backward scan, cathodic peak was not detected. Another side for G/Ni and G/Ni/Ag peaks were detected at -0.7 V which was Ni/Ni^{2+} oxidation, the transformation of α-$Ni(OH)_2$ to β-$Ni(OH)_2$ was seen between the potential ranges of −0.6 to 0.4 V (vs Ag/AgCl). The peak centered at 0.45 V was Ni^{2+}/Ni^{3+} transition and the cathodic peak at almost 0.5 V, corresponded to the Ni^{3+}/Ni^{2+} reduction [19]. For G/Ni/Ag electrode during the forward scan the peak between 0.1 V and 0.35 V attributed to the oxidation of Ag (Ag/Ag_2O and Ag_2O/AgO) [20]. The reduction peaks for these reactions were detected in the backward scan in Fig. 1. The chronoamperometric measurements were given in Fig.2.

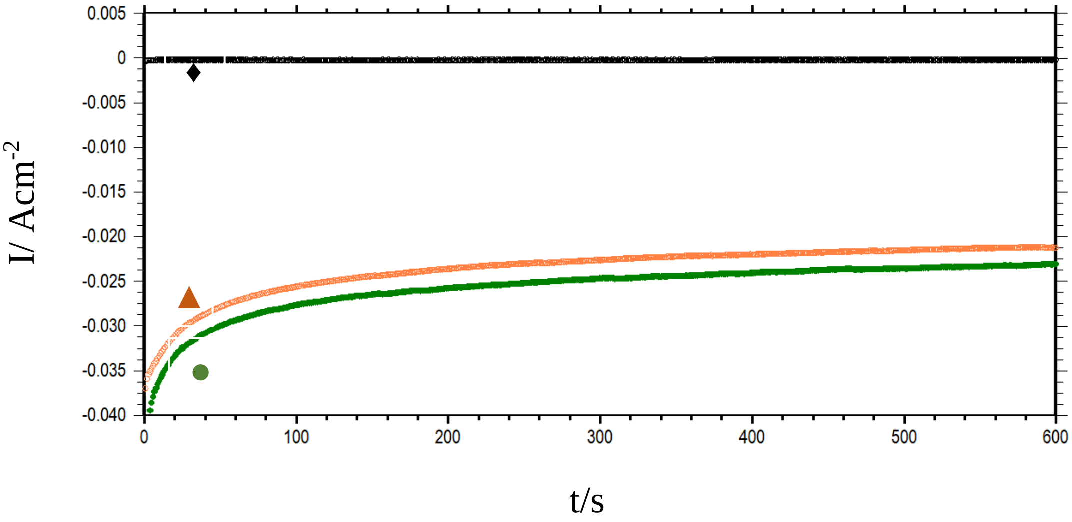

Fig. 2: *The I-t curves of G (♦), G/Ni (▲) and G/Ni/Ag(●) in KOH solution.*

In Fig.2, during 600s significant current was not detected for graphite electrode (G) but Ni and Ni/Ag modified electrodes (G/Ni and G/Ni/Ag) produced hydrogen which was detected with necked eyes and further cathodic current density values were proved that. As seen from Fig.2 G/Ni/Ag electrode presented higher hydrogen performance than G/Ni.

The cathodic polarization curves for all electrodes were given in Fig. 3. The wide oxygen reduction peak was seen for graphite electrode between -1.2 V and -1.4 V (vs. Ag/AgCl). Then the hydrogen evolution process continued. For G/Ni/Ag higher current density values were detected and the polarization data supported the chronoamperometric results. Results were summarized in Table 1, the G/Ni/Ag presented higher hydrogen evolution performance.

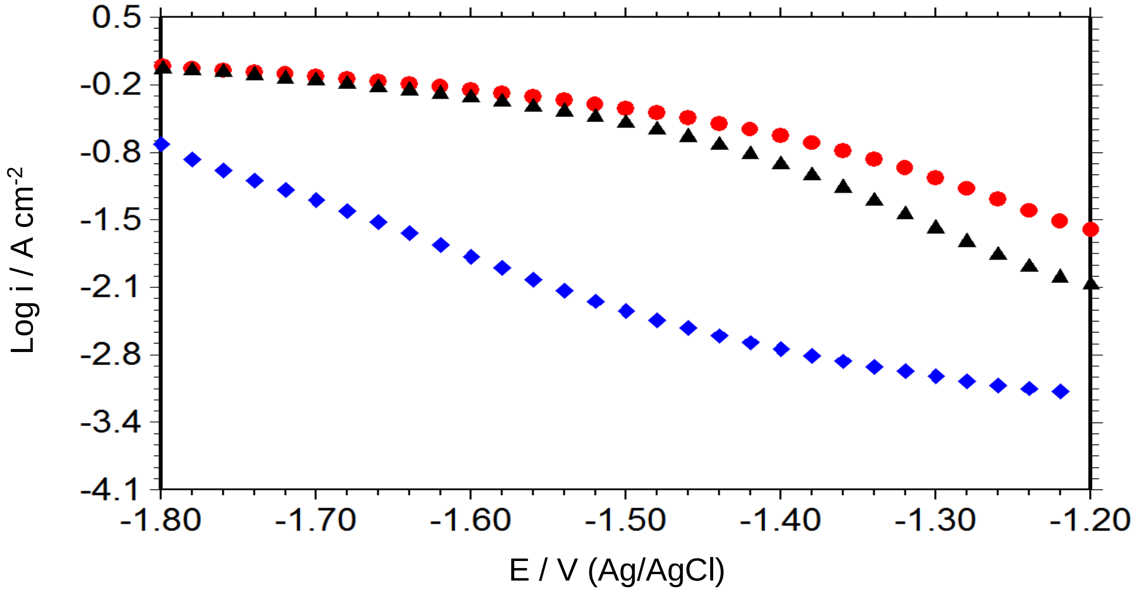

Fig. 3: The cathodic polarization curves of G (♦), G/Ni (▲) and G/Ni/Ag(●) in KOH solution.

Table 1. Electrochemical parameters determined from cathodic current-potential curves.

Electrode	i /mA cm^{-2} @ -1.3 V	i /mA cm^{-2} @ -1.4 V	i /mA cm^{-2} @ -1.5 V	η /V -100 mA cm^{-2}
G	1.201	2.179	5.061	-1.751
G/Ni	30.86	126.0	312.3	-1.382
G/Ni/Ag	93.32	235.3	429.6	-1.307

As seen in Table 1, the current density at -1.3 V increased almost 78 times by Ni/Ag treatment on graphite surface.

The Nyquist plots for all electrodes at varied cathodic potentials, which were determined from cathodic polarization measurements, were given in Figs. 4-6.

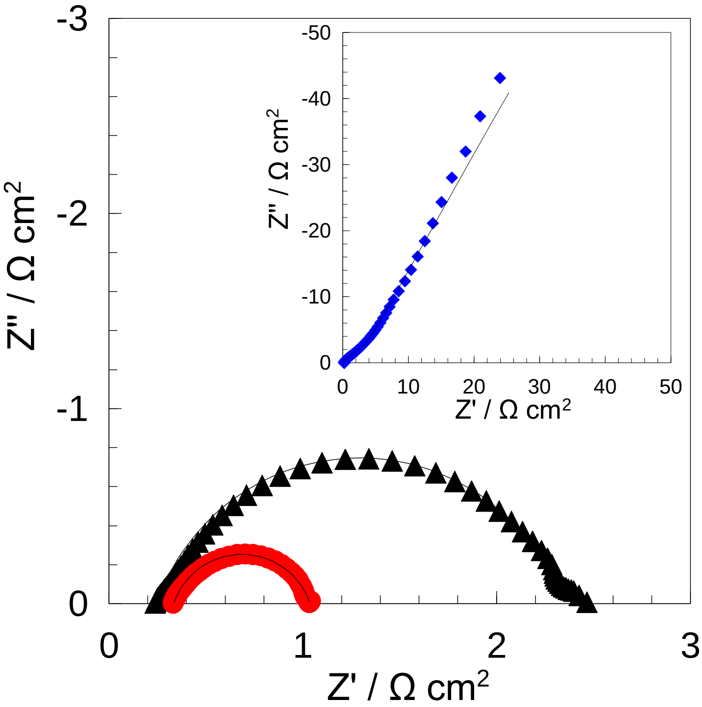

Fig. 4: *The Nyquist plots of G (♦), G/Ni (▲) and G/Ni/Ag(●) at -1.3 V (vs. Ag/AgCl) in KOH solution.*

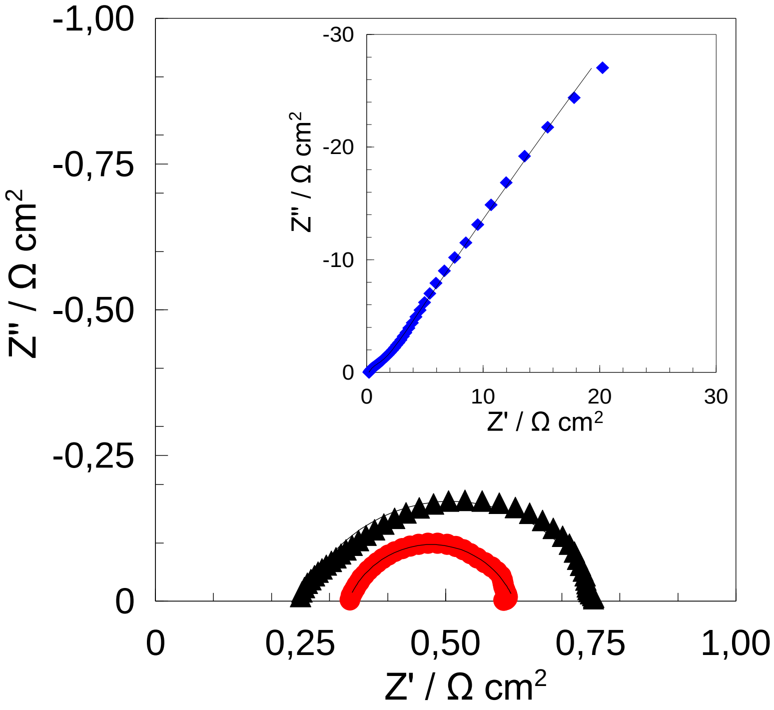

Fig. 5: *The Nyquist plots of G (♦), G/Ni (▲) and G/Ni/Ag(●) at -1.4 V (vs. Ag/AgCl) in KOH solution.*

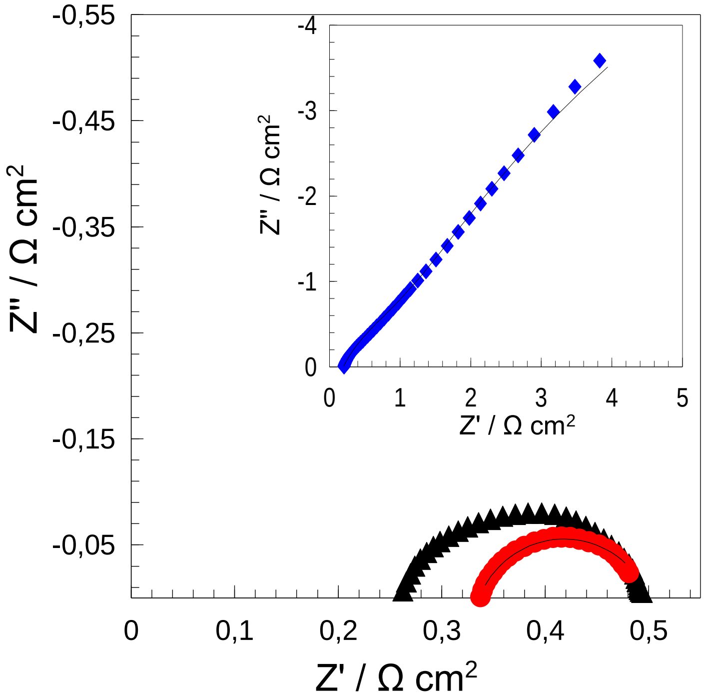

Fig. 6: *The Nyquist plots of G (♦), G/Ni (▲) and G/Ni/Ag(●) at -1.4 V (vs. Ag/AgCl) in KOH solution.*

The equivalent circuits for electrochemical impedance measurements was given in Fig. 7 and related table was presented as Table 2.

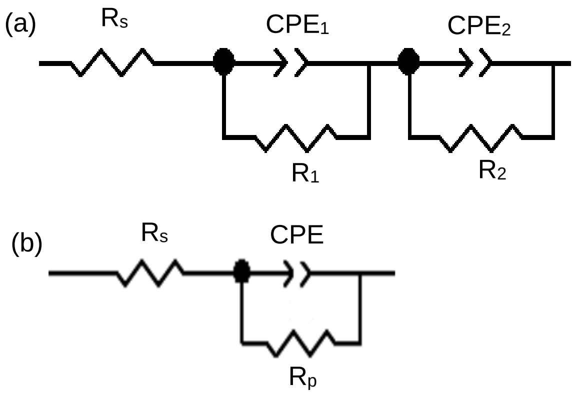

Fig. 7: The equivalent circuits of G(a), G/Ni and G/Ni/Ag (b). CPE: Constant phase element, Rs: Solution resistance, Rp: Polarization resistance (R1+R2)

As seen from Figs. 4-6, Nyquist plots of G presented two time constants but G/Ni and G/Ni/Ag presented one time constant. Therefore, related equivalents for these electrodes were different and presented in Fig. 7. As seen from Table 2, for all electrodes polarization resistance values decreased with increasing cathodic potential. The lower R_p values were detected for G/Ni/Ag.

Table 2. Electrochemical parameters determined from the EIS measurements.

Electrodes	E / V	R_1 (Ω cm^2)	CPE_1 (Ω^{-1}s^n cm^{-2})	n_1	R_2 (Ω cm^2)	CPE_2 (Ω^{-1} s^{n}cm^{-2})	n_2	R_p (Ω cm^2)
G	-1.3	2.23	0.035	0.75	3551	0.108	0.68	3553.2
	-1.4	0.91	0.050	0.75	1068	0.122	0.64	1068.9
	-1.5	0.68	0.093	0.67	20.38	0.134	0.66	21.1
G/Ni	-1.3	2.09	0.0109	0.79	-	-	-	2.09
	-1.4	0.51	0.0115	0.75	-	-	-	0.51
	-1.5	0.24	0.0131	0.71	-	-	-	0.24
G/Ni/Ag	-1.3	0.70	0.0093	0.79	-	-	-	0.70
	-1.4	0.29	0.0102	0.76	-	-	-	0.29
	-1.5	0.16	0.0109	0.76	-	-	-	0.16

As shown in Table 2, the R_p values of Ni and Ag coated graphite electrodes were significantly lower than bare graphite. That is, when graphite is coated with Ni or Ag, a decrease in R_p values is observed. Among these three types of electrodes, the lowest R_p values were obtained in G/Ag electrode. Therefore, a low R_p value means that the catalytic effect of the electrode is high. Furthermore, as the catalytic effect increases, an increase in CPE values is expected. When the CPE values are compared among themselves, it is seen that the highest CPE values are obtained at G/Ag electrode. From these results, it can easily be said that G/Ag electrode is the most effective or highest activity electrode for hydrogen output (HER).

4. Conclusions

The electrocatalytic performance of the graphite electrode for hydrogen production reaction was enhanced via deposition of thin Ni coating on the surface and further activity increased via Ag decoration on it. We aimed to extend usage of a graphite electrode for hydrogen production by alkaline electrolysis because of its reasonable price and some mechanical properties (lightness, high electrical conductivity, resistivity against corrosive solvents, etc.). Results showed that G/Ni/Ag performed higher hydrogen production activity. The polarization resistance of graphite at -1.3 V (vs. Ag/AgCl) decreased almost 5075 times with the help of Ni/Ag deposition on surface.

Acknowledgements

The authors are greatly thankful to Mardin Artuklu University Research Fund for financial support (Project Number: MAÜ.BAP.18.SYO.021).

References

1. B. Yazici, G. Tatli, H. Galip, M. Erbil, Int. J. Hydrogen Energy **20**,(1995).
2. A. Döner, F. Tezcan, G. Kardaş, Int. J. Hydrogen Energy **38**, (2013).
3. L. Elias, A. C. Hegde, Materials Today: Proceedings **5**, (2018).
4. A. Döner, R. Solmaz, G. Kardaş, Int. J. Hydrogen Energy **36**, (2011).
5. A. Döner, Int. J. Hydrogen Energy **43**, (2018).
6. H. Zhuang, Z. Cai, W. Xu, X. Zhang, M. Huang, X. Wang, Catal. Commun. **120**, (2019).
7. A. Döner, G. Kardaş, Int. J. Hydrogen Energy **40**, (2015).
8. Z.R. Ismagilov, E.V. Matus, I.Z. Ismagilov, O.B. Sukhova, S.A. Yashnik, V.A. Ushakov, M.A. Kerzhentsev, Catal. Today **323**, (2019).
9. A. Ongun Yüce, A. Döner, G. Kardaş, Int. J. Hydrogen Energy **38**, (2013).
10. G. Xu, Z. Wang, J. Chen, J. Lv, J. Huang, P. Zhang, Y. Qin, Y. Wu, J. Solid State Chem. **246,** (2017).
11. H. Yüksel, A. Özbay, M. Kahraman, R. Solmaz, Int. J. Hydrogen Energy **43**, (2018).
12. R. Solmaz, Int. J. Hydrogen Energy **38**, (2013).
13. M. Farsak, G. Kardaş, J. Hydrogen Energy **44**, (2019).
14. A.J.Vizcaíno, A.Carrero, J.A.Calles, Int. J. Hydrogen Energy **32**, (2007).
15. C. Wu, P. T.Williams, Appl. Catal. B Environ. **87**, (2009).
16. A.L. Yuvaraj, D. Santhanaraj, Materials Research 17, (2014).
17. M. B. Koca, G. Gümüşgöz Çelik, G. Kardaş, B. Yazici, Int. J. Hydrogen Energy **44**, (2019).
18. A. Döner, E. Taşkesen, G. Kardaş, Int. J. Hydrogen Energy **39**, (2014).
19. M. E. Mert, B. Doğru Mert, G. Kardaş, B. Yazici, Appl. Surf. Sci. **423**, (2017).
   E. Baran, B. Yazici, Int. J. Hydrogen Energy **41**, (2016)

International Conference on Condensed Matter and Materials Science
ICCMMS-2019
14-19 October 2019
ADANA, TURKEY

The Effect of Calcination Conditions on Luminescence Efficiency of BeO Ceramics Synthesized Using Co-Precipitation Method

V. Altunal*, V. Guckan, A. Ozdemir, and Z. Yegingil

Department of Physics, Faculty of Art and Sciences, Cukurova University, Adana 01330, Turkey

BeO ceramics were synthesized by co-precipitation method. The luminescent behaviors of the BeO ceramics prepared under different reaction conditions were investigated for radiation dosimetry applications. The appropriate calcination temperature and time for the sol-gel synthesis of BeO was determined as 1000 °C for 4 hours by analyzing optically stimulated luminescence (OSL), thermoluminescence (TL) sensitivities and radioluminescence (RL) emissions of the products. While similar characteristic broad emission peak of BeO ceramics between 200 and 500 nm was obtained in RL spectra, an unexpected peak between 650 and 800 nm which may be associated with the anion defects in BeO was observed. While highly sensitive two TL peaks were observed up to 250 °C, low sensitive four TL peaks were found up to 650 °C. The results showed that luminescent signals from the BeO pellets produced at appropriate synthesis conditions were suitable for radiation measurement applications in personal dosimetry.

Keywords: Beryllium oxide (BeO), Precipitation synthesis, Calcination Conditions, Radiation Dosimetry, Luminescence

*Corresponding author: valtunal@cu.edu.tr

Introduction

New and rapidly developing applications in physics and medicine encourage researchers to produce new materials. The synthesis process is very important as it affects the general properties of the produced materials. Moreover, the ceramic preparation process has to incorporate a variety of production techniques (for micro and nano structures). Micro or nano structures, synthesis conditions (calcination and sintering) and particle size change the luminescence properties of ceramics [1]. Another factor affecting luminescence properties of ceramics is the synthesis method. For example, narrow particle size distribution and high homogeneity are provided in the sol-gel method, while low cost, controllable and small particle size in the precipitation method provide an easy synthesis process. Luminescent emitting ceramics are used in many areas such as lighting, display, radiation dosimeters [2, 3]. Specifically, the use of ceramic materials in radiation dosimetry is increasing day by day with the discovery of materials (Al_2O_3, BeO, MgO etc.) having unique physical, chemical, and luminescence properties. BeO Thermalox995 chip (from Materion Corporation), together with Al_2O_3:C (Al_2O_3:C from Landauer Inc.) nanoDot dosimeter, is one of the ceramic materials commonly used in OSL dosimetry. It has been known for over 50 years that the material exhibits TL and OSL signals [4-8]. Being a tissue-equivalent material (Z_{eff} ~7.1) [9], not losing radiation dose for about 6 months[10], thermal stability and light sensitive dosimeter attracted researchers [8], and recently produced BeO-based OSL dosimetry system as a product of ongoing studies [10-12].

In this study, BeO ceramics were synthesized using precipitation method. To obtain more stable luminescent signals from the surface of ceramics, BeO samples were prepared in pellet form from the nano-powders. The effects of calcination temperature and duration on luminescence signals were investigated using TL, OSL, and RL techniques. We investigated whether the usage of appropriate calcination conditions in BeO precipitation synthesis is a good starting operation to achieve a promising OSL dosimeter with high luminescent efficiency, or not.

Material and Method

All reagents, polyethyleneimine solution, ammonium hydroxide solution (NH_4OH) and beryllium sulfate tetra-hydrate ($BeSO_4 \cdot 4H_2O$) with high purity used in synthesis were purchased from Sigma Aldrich. The synthesis process began with the complete dissolution of beryllium sulfate salts in distilled water. On the other hand, the polyethyleneimine solution was stirred in distilled water for a certain period of time and added to the main solution slowly. Thus, the precipitation process started. The pH control of the solution was carried out by adding a certain amount of ammonia to the solution. During the ongoing stirring, precipitate was observed and the solution in the beaker was transferred to a suitable crucible. Then the temperature of the main solution in the crucible was increased to 200 °C, and the water in the solution was removed. The calcination process was carried out to remove the organics from the final product and to form BeO. In this study, while calcination temperatures were selected as 800, 900, 1000, 1100 and 1200 °C, the duration times were 2, 4, 6, 8, 10 and 24 hours. After the calcination process, BeO samples were prepared in pellet form by using pure BeO powders for easily handling and to obtain stable luminescent signals from the surfaces of BeO. Here, applied pressure was 500 kgforce/cm^2 and duration time was 1 min. Finally, to correct trap structures and achieve a uniform crystal structure, prepared pellets were sintered at 1600 °C, for 4 h. The photo of the BeO ceramics synthesized by precipitation method was shown in Fig. 1.

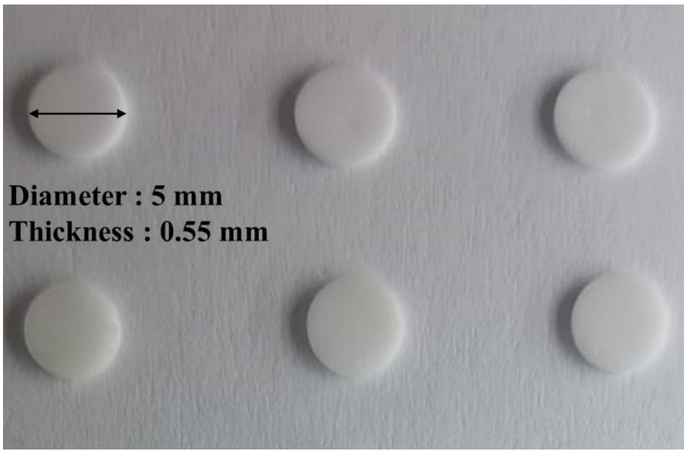

Figure 1. The produced BeO pellets

After the sample preparation, TL and OSL measurements were performed using DA-20 model RisØ TL/OSL reader system equipped with ^{90}Sr-^{90}Y beta radiation source with the energy of 2.27 MeV and bialkali model 9235 QA photomultiplier tube. Light stimulations were used in continuous wave OSL mode by blue LEDs (λ ~ 470 nm). TL and OSL signals were detected using a Hoya U-340 nm UV pass filter in front of PMT. RL emissions of the BeO pellets were obtained from a homemade X-ray Luminescence system equipped with an 4-40 kV X-ray tube and USB-2000 model Ocean Optics fiber spectrometer which is produced for low sensitivity applications.

Results and Discussion:

RL emissions

RL emissions obtained from the BeO pellets calcinated at different calcination temperature of 800, 900, 1000, 1100 and 1200 °C for 4 h in Fig. 2. According to RL emissions, since the maximum intensity was obtained from the BeO pellets calcinated at 900 °C, the appropriate calcination temperature was selected as 900 °C. After the determination of the appropriate calcination temperature, BeO materials were synthesized in similar way and calcinated at 900 °C for different calcination durations of 2, 4, 6, 8, 10, and 24 hours. RL emissions for different durations were presented in Fig. 3. According to RL emissions in Fig. 3., the maximum intensity was obtained from the BeO pellets calcinated at 900 °C for 4 h. The appropriate calcination duration was selected as 4 h.

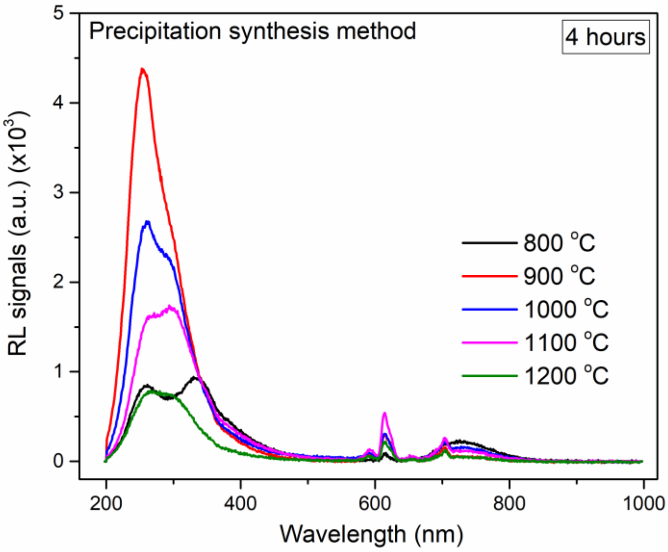

Fig. 2. RL emissions of BeO pellets which was calcinated at different temperatures for 4 h.

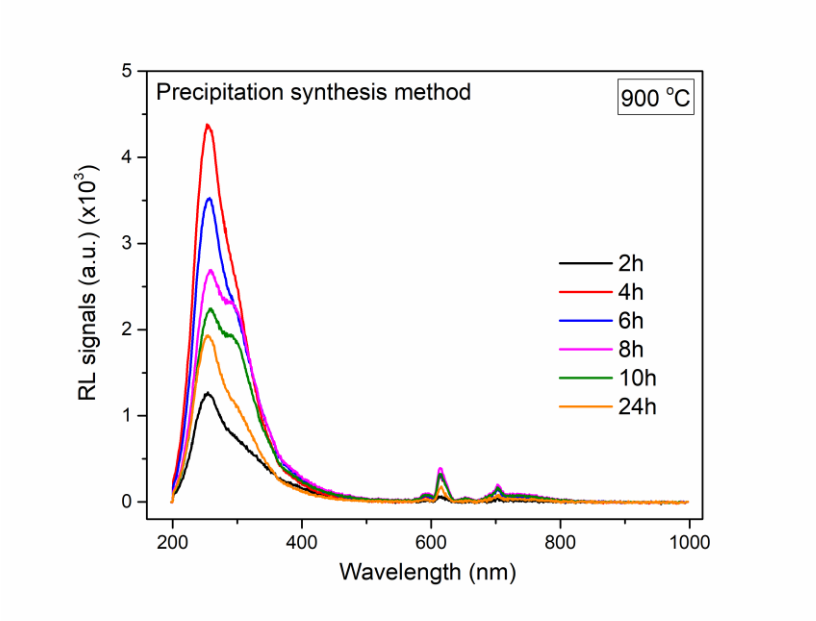

Fig. 3. RL emissions of BeO pellets which was calcinated at 900 °C for different durations.

On the other hand, all the obtained RL emissions shows the same broad highly sensitive emission peak located between 200 and 500 nm. This characteristic luminescence emission (3-4 eV and 4.9 eV) is associated with the radiative annihilation of the self-trapped excitons in BeO [13, 14]. Additionally, the emission peaks located at 590, 620 and 640 nm are originated from the background signals of the RL system. Unexpected emissions located between 700 and 800 nm is associated with the oxygen defects in BeO may act as anion defects in the structure. It is known that such anion defects occurring during synthesis in the structure may show large emissions at high wavelengths in RL measurements.

TL Glow Curves

Fig. 4. shows TL glow curves obtained from the BeO pellets calcinated at different calcination temperature of 800, 900, 1000, 1100 and 1200 °C for 4 h. As seen from the Fig 4., BeO pellets exhibited three TL peaks located at 170, 260 and 440 °C. Similar TL trap distribution was presented by Altunal et al. [13]. Due to maximum intensity at 900 °C, the appropriate calcination temperature was selected as 900 °C. After the determination of the appropriate calcination temperature, BeO materials were synthesized in similar way and calcinated at 900 °C for different calcination durations of 2, 4, 6, 8, 10, and 24 hours. TL glow curves for different durations were presented in Fig. 5. Finally, the maximum trapped charge population was obtained from the BeO pellets calcinated at 900 °C for 4 h. Considering all the TL glow curves of BeO samples, the total charge population gave the maximum value for the sample calcined at 900 °C for 4 h because different calcination conditions do not change the structure of TL traps in BeO.

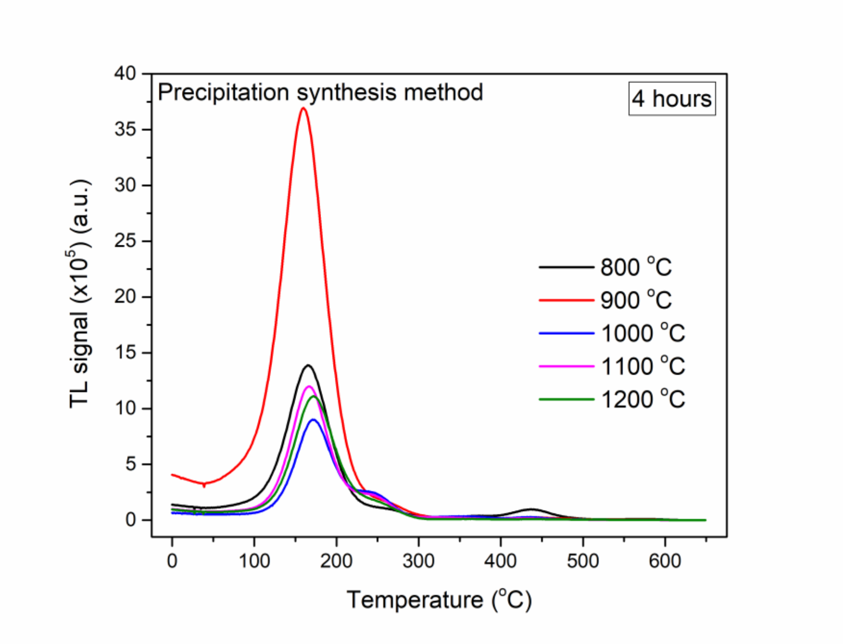

Fig. 4. TL glow curves of BeO pellets calcinated at different temperatures for 4 h.

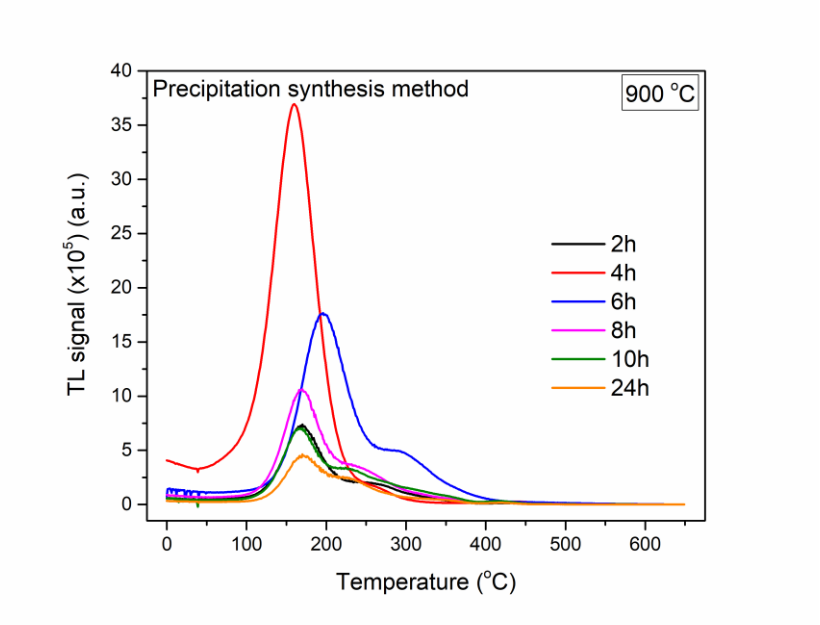

Fig. 5. TL glow curves of BeO pellets calcinated at 900 °C for different durations.

OSL Decay Curves

Fig. 6. shows OSL decay curves of 0.5 Gy irradiated BeO pellets which was calcinated at different temperature of 800, 900, 1000, 1100 and 1200 °C for 4 h. After a preheat treatment of 100 °C for 10s, the OSL decay curves were obtained with blue light stimulations throughout 200 s. As seen from the Fig. 6., the maximum OSL signal intensity was obtained from the BeO pellets calcinated at 900 °C as for RL and TL signals. In order to see more clearly the total trapped charge population, inset Fig. 6. provides integrated OSL signals obtained by collecting data from 0 to 200 s against the calcination temperature. As results obtained from the maximum OSL signals, the total charge population gave the maximum value for the sample calcined at 900 °C because the structure of the OSL decay curves did not change. In addition to calcination temperature study, OSL decay curves were obtained from the BeO pellets calcinated at 900 °C for different durations of 2, 4, 6, 8, 10, and 24 h (see Fig. 7). As seen from the Fig. 7., the maximum OSL signal intensity was obtained from the BeO pellets calcinated at 1000 °C for 4 h. Considering the total trapped charge population from a different perspective, the integrated OSL signals were presented in inset Fig.7. against the calcination durations. Considering all the OSL decay curves of BeO samples, the total charge population gave the maximum value for the sample calcined at 900 °C for 4 h because different calcination conditions do not change the structure of OSL traps in BeO.

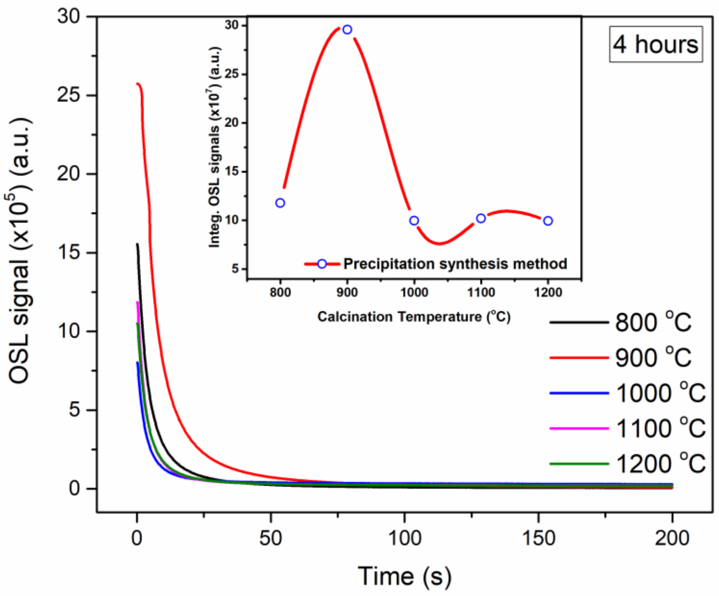

Fig. 6. OSL decay curves of BeO pellets calcinated at different temperatures for 4 h. Inset: Integrated OSL signals of BeO pellets calcinated at different temperatures for 4 h.

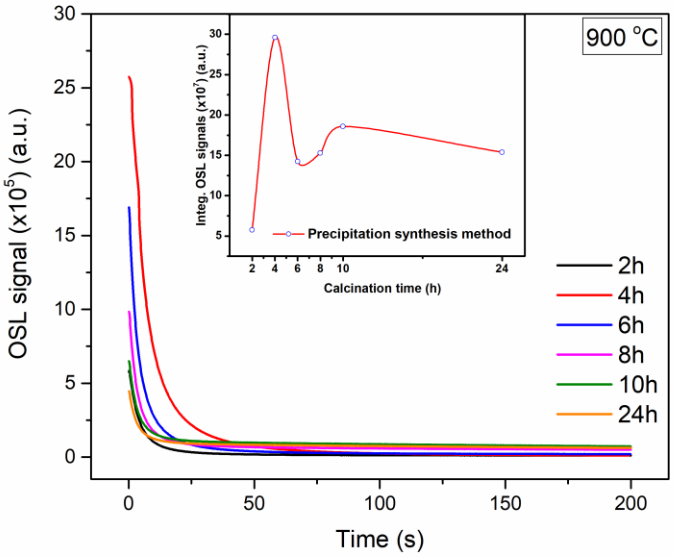

Fig. 7. OSL decay curves of BeO pellets calcinated at 900 °C for different durations. Inset: Integrated OSL signals of BeO pellets calcinated at 900 °C for different durations.

Conclusions

Undoped BeO powders were synthesized using precipitation method and prepared as ceramic pellet. All the RL emissions are in well agreement with previously reported emissions. It was clearly demonstrated that TL and OSL signals can be used in radiation dosimetry applications. In future studies, more dosimetric properties of the material should be examined using TL and OSL methods for different calcination conditions.

References:

[1] T. Rivera, Synthesis and thermoluminescent characterization of ceramics materials, Advances in ceramics–synthesis and characterization, processing and specific applications. InTech, Rijeka, Croatia (2011) 127-164.

[2] P. Boch, J.-C. Niepce, Ceramic Materials: Processes, Properties, and Applications, John Wiley & Sons2010.

[3] C.B. Carter, M.G. Norton, Ceramic materials: science and engineering, Springer2007.

[4] H.O. Albrecht, C.E. Mandeville, Storage of Energy in Beryllium Oxide, Physical Review 101(4) (1956) 1250-1252.

[5] C.R. Rhyner, W.G. Miller, Radiation dosimetry by optically-stimulated luminescence of BeO, Health Phys 18 (1970) 681-684.

[6] E. Tochilin, N. Goldstein, W. Miller, Beryllium oxide as a thermoluminescent dosimeter, Health Phys 16(1) (1969) 1-7.

[7] S.W. McKeever, M. Moscovitch, P.D. Townsend, Thermoluminescence dosimetry materials: properties and uses, (1995).

[8] E. Bulur, H.Y. Goksu, OSL from BEO ceramics: New observations from an old material, Radiation Measurements 29(6) (1998) 639-650.

[9] A.J.J. Bos, High sensitivity thermoluminescence dosimetry, Nucl Instrum Meth B 184(1-2) (2001) 3-28.

[10] M. Sommer, J. Henniger, Investigation of a BeO-based optically stimulated luminescence dosemeter, Radiat Prot Dosimetry 119(1-4) (2006) 394-7.

[11] M. Sommer, A. Jahn, J. Henniger, Beryllium oxide as optically stimulated luminescence dosimeter, Radiation Measurements 43(2-6) (2008) 353-356.

[12] A. Jahn, M. Sommer, W. Ullrich, M. Wickert, J. Henniger, The BeOmax system – Dosimetry using OSL of BeO for several applications, Radiation Measurements 56 (2013) 324-327.

[13] V. Altunal, V. Guckan, A. Ozdemir, A. Sotelo, Z. Yegingil, Effect of sintering temperature on dosimetric properties of BeO ceramic pellets synthesized using precipitation method, Nuclear Instruments and Methods in Physics Research Section B: Beam Interactions with Materials and Atoms 441 (2019) 46-55

[14] V. Altunal, V. Guckan, A. Ozdemir, N. Can, Z. Yegingil, Luminescence characteristics of Al-and Ca-doped BeO obtained via a sol-gel method, J Phys Chem Solids (2019).

Structure characterization and luminescence studies of MgO:Li calcinated at different temperatures via solution combustion and sol-gel methods

V. Guckan[1*], V. Altunal[1], A. Ozdemir[1] and Z. Yegingil[1]

[1]*Department of Physics, Faculty of Art and Sciences, 01330 Balcali Saricam, Adana, Turkey*
Corresponding E-mail: veysiguckan@gmail.com

In the present study, lithium (Li) doped magnesium oxide (MgO) samples were prepared using Solution Combustion Synthesis (SCS) and Sol-Gel (SG) methods. Their photoluminescence (PL) and thermoluminescence (TL) behaviors were determined after the different calcination temperatures. The aim of this study is to investigate the effect of different calcination temperatures on the PL and TL sensitivities of lithium doped MgO (MgO:Li) samples in pellet and powder forms prepared by SCS and SG methods. The structural characterization analysis of MgO:Li powder and pellets were carried out using X-ray diffraction (XRD) and scanning electron microscope (SEM) methods. The results of these structure analysis showed that MgO:Li samples have different crystal properties when changing calcination temperatures were applied during the preparation of the samples. Luminescence properties of the MgO samples which were synthesized at different calcination temperatures were investigated by the Photoluminescence (PL) and TL techniques. The maximum TL intensity of the samples was obtained at calcination temperature of 800 and 1000 °C for the SCS and SG methods, respectively. Uncontrolled chromium impurities were observed in MgO samples by using PL measurements. On the PL spectrum, peaks indicating chromium (III) (Cr^{3+}) transmission in the red portion of the spectrum at 672, 698 and 721 nm are clearly evident. We investigated high dose sensitivity in these samples. Therefore, we suggest this material as a new high dose thermoluminescence dosimeter.

Introduction

Magnesium oxide (MgO) is a wide band-gap (E_g=7.8 eV) insulator under ambient pressure. MgO has high chemical and thermal stability, and high surface reactivity. These properties make it a promising material for application in sensors, catalysis, paints and additives [1]. MgO has a high melting point about 2800 °C. Its density is about 3.58 g/cm^3 and the Mg ions occupy the octahedral sites within the anion close-packed structure [2].

MgO has long been accepted as a luminescence dosimetry material, mainly for use with the thermoluminescence (TL) technique. In order to increase the number of materials suitable for optically stimulated luminescence (OSL) dosimetry, many researchers have investigated the luminescence characteristics of this material [3-5]. There are many reports of MgO doped with lanthanides or transitions metal ions to increase the TL or OSL signals and to improve its dosimetric characteristics [4, 6, 7].

In this study, the effect of calcination conditions on TL and OSL intensities of MgO phosphors produced by the SCS and SG methods were presented. Li ion were doped into the MgO phosphors during synthesis process as dopants and different calcination temperature and times were performed to obtain high sensitivity MgO luminophors that can be for TL and CW-OSL dosimeters. Structure and morphology of the synthesized materials were checked by

XRD and SEM methods. The TL and OSL curves of Li doped MgO phosphors calcinated at different temperature and times were compared with each other.

Materials and Methods

Material Preparation

This study presents the calcination effect on MgO samples in pellet form prepared by SCS and SG methods. All chemicals were supplied from Sigma Aldrich. Li was used as the dopant with 0.1% mol for both methods. The calcination temperatures and times used in both production methods are 800, 900, 1000, 1100 and 1200 ^{o}C for 2, 4, 6, 8, 10 and 24 hours. After the bulk material was produced, the material was divided into 5 equal parts and then calcined at different temperatures, keeping the time constant for 4 h. In this work, MgO samples were studied in pellet form for having more settled PL and TL signals and for easy handling. MgO pellets were performed as a 6 mm diameter and 0.6 mm thickness as a shape of disk form using 25 milligrams calcinated powders. In all TL measurements, readings were taken after sintering of all types of pellets at 1600 ^{o}C for 4h. The calcination temperature giving the best TL signal was selected and time experiment was performed. The same process was repeated for the time experiment.

Characterization

A few characterization analyses of MgO samples obtained by SCS and SG methods were performed. All of the analysis was performed at the room temperature. The phase evaluation and crystal structure characteristics of pellet-shaped MgO samples were studied by means of XRD technique. The measurements were performed using XRD PANalytical EMPYREAN branded diffractometer equipped a copper and cobalt X-ray tube, and copper Kα radiation wavelength was 0.1541 nm. Diffraction angles were adjusted from 20° to 90° (scan mode, $\Delta 2\theta = 0.02°$). Qualitative phase analyzes were performed by comparison of the experimental diffraction patterns with the standard ones from the International Centre for Diffraction Data (ICDD). The surface morphology of the samples and microstructures of MgO pellets were examined using a FEI branded Quanta 650 model field-emission SEM with 30–100 kV accelerating voltage and 100nA probe current.

Luminescence measurements

PL measurements were performed using a monochromatized xenon lamp as the excitation source. All PL spectra were obtained at room temperature. The PL and PLE spectra were measured using a Horiba/Jobin-Yvon Fluorolog-3 spectrofluorimeter. It has a continuous xenon lamp (450 W) and a photomultiplier tube (Hamamatsu R928P). The measured PLE spectra were corrected by the xenon lamp emission spectrum.

TL measurements were carried out using a Risø TL/OSL reader model DA-20 (Risø National Laboratory, Denmark). Luminescence emission were measured in the VIS region using a Schott BG-39 filter (300–700 nm) and UV region using a bandpass filter (Hoya, U-340, transmittance range from 250 to 390 nm, max 340 nm) in front of the PM tube. In order to the detection of light, a bialkali photomultiplier tube (PMT) was used (model 9235QB, Electron Tubes Ltd., Uxbridge, UK). Samples were irradiated at room temperature using an in situ

^{90}Sr/^{90}Y beta source. This ionizing irradiation source emits beta particles with a maximum energy of 2.27 MeV. All TL measurements were performed at a heating rate of 5 ^{o}C/s.

Results and Discussion

Crystallographic characterization and morphology of the samples were studied by XRD and SEM. The XRD pattern of Li doped MgO pellets are given in Fig. 1. Fig. 1 shows that the pattern matched well with ICDD 98-064-2714 in terms of peak positions indicating the formation of single phase. It has cubic structure with lattice parameters of a =b=c=4.2080 Â. XRD spectra of all MgO:Li pellets having the diffraction peaks (111), (200), (220), (311) and (222) located at 2theta = 36.9°, 42.9°, 62.3°, 74.7°and 78.7°, respectively. It was observed that the different calcination temperatures applied did not cause any difference in the phase in the crystallographic structure.

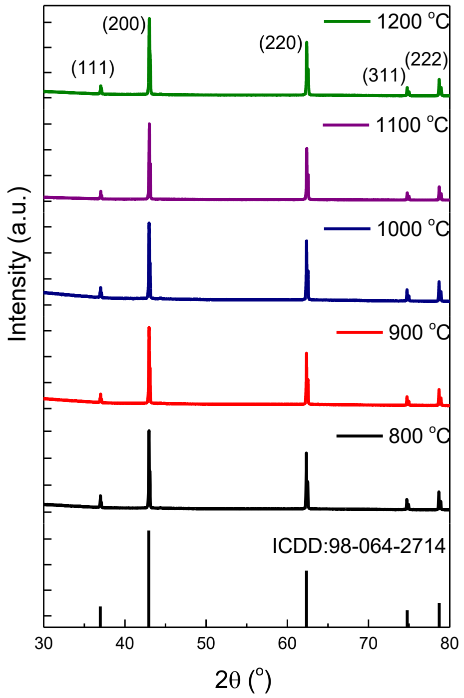

Figure 1. *XRD analysis of MgO:Li pellets calcinated at different temperatures.*

The SEM images revealed the morphological characteristics of Li doped MgO pellets produced by sol-gel methods. The SEM images of produced samples are shown in Fig. 2. There are homogeneous distribution among particles for all the MgO:Li pellets. These images do not clearly show us how the calcination temperature creates differences in the morphology of the MgO pellets. It needs further studies.

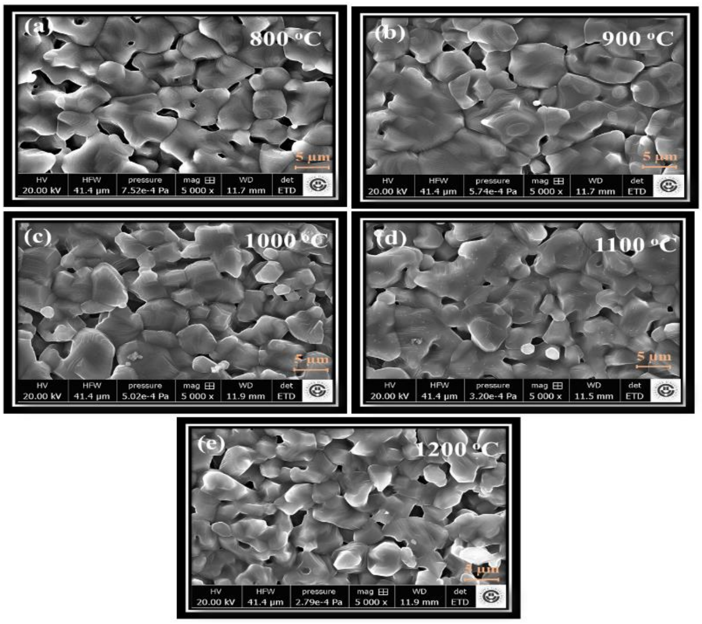

Figure 2. *The typical SEM images of MgO:Li pellets calcinated at; (a) 800 °C, (b) 900 °C, (c) 1000 °C, (d)1100 °C and (e) 1200 °C for 4 h*

The room temperature photoluminescence emission spectrum of MgO:Li pellets prepared by combustion and sol-gel methods excited with a wavelength 330 nm were shown in Fig. 3. MgO:Li pellets prepared using SCS method have a broad emission peak centered at ~660 nm (1.88 eV, orange region). The pellets produced using the sol-gel method have both a relatively narrow peak at 660 nm and a peak at 720 nm in some of the samples. Interestingly, uncontrolled chromium impurities were observed in MgO samples. When the samples excited with 440 nm, peaks indicating chromium (III) (Cr^{3+}) transmission in the red portion of the spectrum at 672, 698 and 721 nm are clearly evident (see Fig. 4) [1, 2].

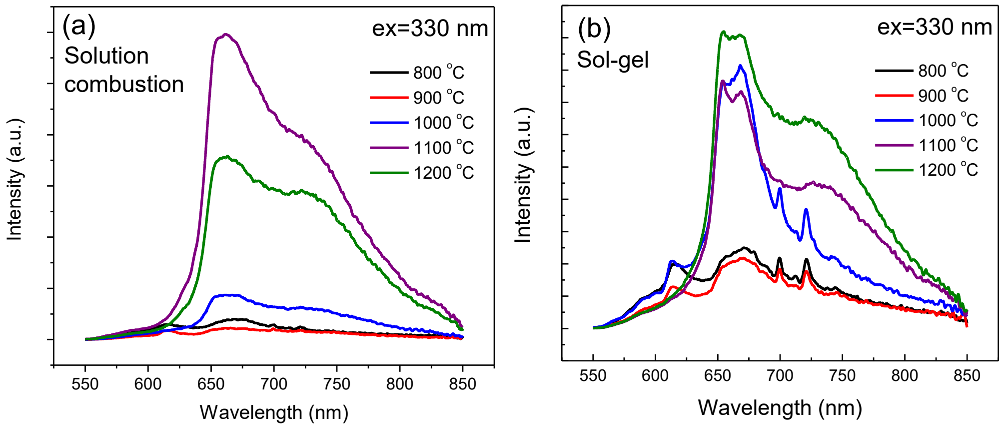

Figure 3. *The PL spectra of the MgO:Li pellets*

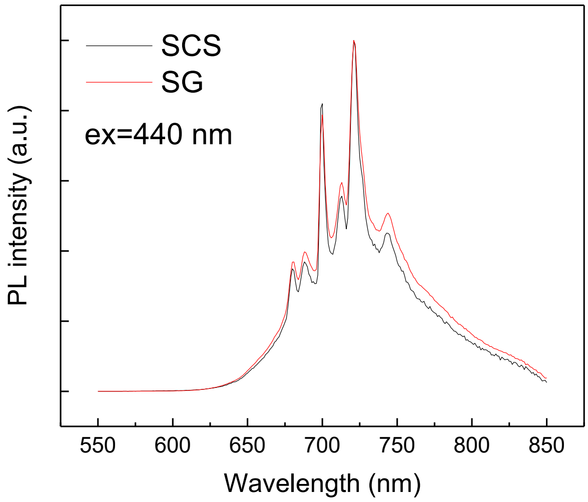

Figure 4. *The PL spectra of the MgO:Li pellets under 440 nm excitation.*

Fig. 4 shows the TL glow curves from MgO:Li pellets after 2 Gy beta irradiation in comparison with calcinated samples at different temperatures. TL readouts were performed by heating each sample from room temperature up to 450 °C with a heating rate of 5 °C/s. As is seen in Fig. 4a, maximum trapped charge populations were obtained from MgO:Li pellets prepared using SCS method with calcination temperature at 800 °C for 4 h. Fig. 4b shows that the maximum intensities of MgO:Li pellets were recorded from samples calcinated at 1000 °C for 4 h.

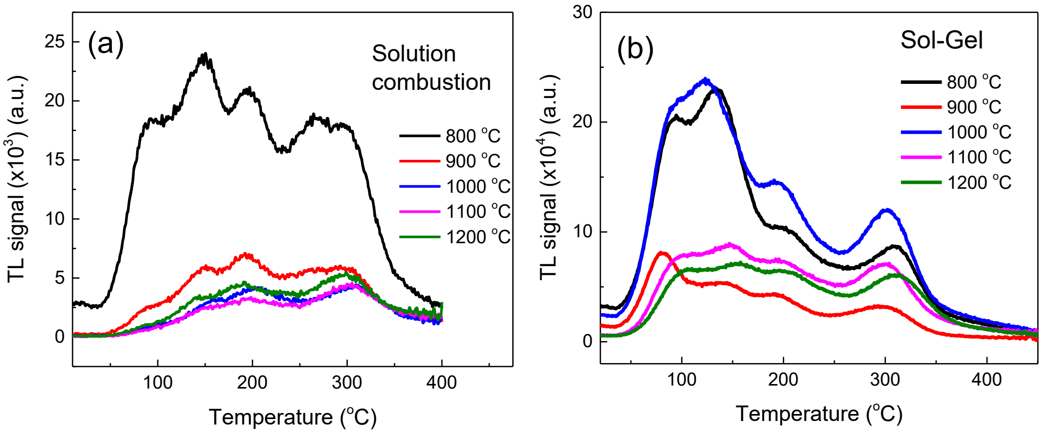

Figure 4. *The TL glow curves from MgO:Li pellets prepared using (a) solution combustion method and (b) sol-gel method calcinated at 800 °C, 900 °C, 1000 °C, 1100 °C and 1200 °C for 4 h.*

Conclusions

Li doped MgO pellets produced using solution combustion synthesis and sol-gel methods were verified by XRD measurements. MgO samples did not contain different phases were highly compatible with the reference number ICDD 98-064-2714 in terms of peak positions. SEM images showed that all samples were homogeneous with no hollow structure between the grains. According to TL measurements, for the Li doped MgO samples prepared using SCS and SG methods, the maximum trapped charge populations were obtained from MgO:Li pellets with calcination conditions of 800 ^{o}C. and the maximum intensities of MgO:Li pellets were recorded from samples calcinated at 1000 ^{o}C, respectively. However, it is evident that the trap structures formed in the material could not be formed at high energy levels by the dopants. Therefore, TL peaks were obtained at temperatures lower than desired. It was observed that the change in calcination temperature did not affect the TL glow curve. It is clear that the effect of calcination temperature on TL signals needs further study.

References

1. Shukla, S., et al., *Nano-like magnesium oxide films and its significance in optical fiber humidity sensor.* Sensors and Actuators B: Chemical, 2004. **98**(1): p. 5-11.
2. Klein, C. and C. Hurlbut Jr, *Manual of Mineralogy. John Wiley & Sons.* Inc., New York, 1999.
3. Oliveira, L., E. Milliken, and E. Yukihara, *Development and characterization of MgO: Nd, Li synthesized by solution combustion synthesis for 2D optically stimulated luminescence dosimetry.* Journal of Luminescence, 2013. **133**: p. 211-216.
4. Oliveira, L., B. Doull, and E. Yukihara, *Investigations of MgO: Li, Gd thermally and optically stimulated luminescence.* Journal of Luminescence, 2013. **137**: p. 282-289.
5. Bos, A., M. Prokić, and J. Brouwer, *Optically and thermally stimulated luminescence characteristics of MgO: Tb3+.* Radiation protection dosimetry, 2006. **119**(1-4): p. 130-133.
6. Yukihara, E., et al., *Systematic development of new thermoluminescence and optically stimulated luminescence materials.* Journal of Luminescence, 2013. **133**: p. 203-210.
7. Oliveira, L., E. Yukihara, and O. Baffa, *Lanthanide-doped MgO: A case study on how to design new phosphors for dosimetry with tailored luminescent properties.* Journal of Luminescence, 2019.

Investigation of Radiation Absorption Parameters for elements between 50≤Z≤65 using 59.5 keV Gamma-Ray Photons

Nuray Kup Aylikci*[1]

[1]*Iskenderun Technical University-İSTE, Faculty of Natural Sciences and Engineering, Energy Systems Engineering, Hatay;* nuray.aylikci@iste.edu.tr

Abstract

The radiation absorption capability of materials is one of the most important properties in scientific areas such as radiation physics, nuclear physics, dosimetry and elemental analysis of materials. There are different methods to determine the radiation absorption properties of materials but energy dispersive X-ray fluorescence is the practical, easy and non-destructive method for photon absorption investigation and quantitative analysis of materials. In this study, K-shell absorption jump factors and jump ratios were calculated semi-empirically using the calculated total atomic photo-effect cross section and the measured K_α X-ray production cross-sections. For experimental measurements, the elements were irradiated by 59.5 keV gamma rays from ^{241}Am annular radioactive source. The emitted K X-rays were counted by an Ultra-LEGe detector with a resolution of 150 eV at 5.9 keV. The semi-empirical parameters were compared with the data in the literature and it was found that the semi-empirical values were compatible within experimental error limits (1%–6%).

Keywords: Photo-effect cross-sections, K-shell absorption jump ratio, K-shell absorption jump factor, ^{241}Am radioactive source

1. INTRODUCTION

The interaction of electromagnetic radiation with matter occurs with different process called photo-electric absorption, incoherent scattering, coherent scattering and pair production. But the energy range studied is not capable of pair production process and so this effect can be eliminated in the calculation of absorption parameters. The absorption parameters can easily be obtained by using energy dispersive X-ray fluorescence system using fundamental parameters. The fundamental X-ray fluorescence parameters are sensitive tools for the investigations of complex shell structures of any atom and radiation absorption capability o any material. Mass attenuation coefficient, total absorption cross-section, absorption jump ratio and jump factor are called as the absorption parameters in EDXRF. These parameters are important for the determination of X or gamma ray interaction with matter in different scientific areas (medical physics, nuclear engineering, material science, radiation shielding and etc.).

For low photon energies below 100 keV, the most probable process is the photo-electric absorption with high atomic numbered elements and the determination of the total atomic photo-effect cross-section is probable using energy dispersive system. The gamma or X-ray attenuation method, the Compton peak attenuation method, the energy dispersive X-ray fluorescence method and the Bremsstrahlung transmission method were explained as the calculation methods of absorption parameters [1].In the gamma or X-ray attenuation process, secondary sources are generally used to acquire different photon energies around the K absorption edge of the target. In the Compton attenuation method, the scattered photons which have different energies as a function of scattering angles were used for the attenuation experiments. On the other hand, for Bremsstrahlung attenuation process, a weak beta source was used for absorption measurements. In the literature, it can be found different studies about K shell absorption parameters for pure elements [2–7] and different materials [8–13] using absorption experiments.

In this study, energy dispersive X-ray fluorescence method was used for the calculation of absorption parameters measuring K_α X-ray production cross-section values. The obtained data in this study will shed light for the development of new radiation shielding, radiation attenuation and dosimetric materials and also theoretical models to understand the complexity structure of atomic shells.

2. MATERIAL AND METHODS

2.1. Experimental Measurements

The thin films examined in this study were prepared by distributing powder samples as homogeneous as possible to 1.44 cm^2 area on the Mylar film. The prepared thin films were placed in the experimental geometry to be stimulated by radioactive source and to count the characteristic X-rays that occurred. The geometry of experimental set-up is the same as in our previous study [14] and the produced thin films were irradiated with 59.5 keV energy X-rays released from a filtered ^{241}Am radioactive source. The energy of released X-rays was determined to be larger than K shell absorption edge. The emitted X-rays from the irradiated thin films were counted by an Ultra-LEGe detector whose FWHM was 150 eV at 5.9 keV.

The obtained K shell spectra were analyzed by using Origin Company software program using least square fitting module.

2.2. Data Analysis

The absorption parameters were semi-empirically determined measuring K_α X-ray production cross-section values and calculated by the following relation,

$$\sigma_{K\alpha} = \frac{N_{K\alpha}}{I_0 G \varepsilon_{K\alpha} \beta_{K\alpha} m_i} \tag{1}$$

In which $N_{K\alpha}$ is the measured intensity (area under the photo-peak) corresponding to the K_α X-rays, I_0 is the intensity of the incident radiation, G is the geometric factor, $\varepsilon_{K\alpha}$ is the detection efficiency for the K_α X-rays, $\beta_{K\alpha}$ is the self-absorption correction factor for the target material, which accounts for the absorption in the target of the incident photons and the emitted characteristic X-rays and m_i is the thickness of the target in g/cm^2.The detailed information about the detector geometry, detector efficiency and self-absorption correction factor were explained as in our previous study [14].

K shell absorption jump factors (J_K) and jump ratios (r_K) were semi-empirically calculated as,

$$J_K = \frac{\sigma_{K\alpha}}{\tau_{pe}\omega_K F_{K\alpha}} \tag{2}$$

$$r_K = (1 - J_K)^{-1} \tag{3}$$

where $\sigma_{K\alpha}$ is K_α X-ray production cross-section calculated by Eq. 1 in which the results were published as Ref. [15]. K shell fluorescence yields (ω_K) were taken from Krause [16]. $F_{K\alpha}$ is the probability of K_α X ray emissions in which the values taken from Broll [17] and finally τ_{pe} is total atomic photo-effect cross-sections calculated theoretically by Scofield [18].

3. RESULTS AND DISCUSSIONS

The semi-empirical absorption jump-factors and absorption jump-ratios were shown as Table 1with the theoretical values in the literature and also the fitted values. The fitting polynomials were written on Figs 1 and 2 which showed the change of the absorption parameters against to the atomic number. According to the experimental results, K shell absorption jump factors were changed within experimental error limits versus atomic number when the values compared with the studies of Broll [17] and McMaster [19]. Also, a linear fitting polynomial was obtained for K shell absorption-jump factors as also written below;

$$J_K = 1.04084 - 0.00363\, Z \tag{4}$$

It was obtained that, the fitted values show the best compatibility (changes between 0.03% and 2%) with the values of Broll [17]. When the fitted values were compared with the values of McMaster [19] it was seen that the compatibility ratio was change between 1% and 4%. On the other hand, K-shell absorption jump ratios show different tendency in consideration with the linear fitting polynomial defined K shell absorption jump factors (Figure 2).

Table 1.K shell absorption jump factors (J_K) and jump ratios (r_K)

Elements	J_K				r_K			
	Semi-empirical	Theoretical [17]	Theoretical [19]	Fitted	Semi-empirical	Theoretical [17]	Theoretical [19]	Fitted
$_{50}$Sn	0.866±0.044	0.845	0.830	0.859	7.45±0.38	6.45	5.88	7.05
$_{51}$Sb	0.836±0.043	0.843	0.826	0.856	6.11±0.31	6.37	5.75	6.87
$_{52}$Te	0.843±0.043	0.839	0.822	0.852	6.36±0.32	6.21	5.62	6.69
$_{53}$I	0.869±0.044	0.838	0.821	0.848	7.64±0.39	6.20	5.59	6.53
$_{56}$Ba	0.855±0.044	0.828	0.808	0.838	6.90±0.35	5.95	5.21	6.09
$_{57}$La	0.815±0.042	0.835	0.815	0.834	5.41±0.28	6.07	5.41	5.96
$_{58}$Ce	0.849±0.043	0.830	0.812	0.830	6.61±0.34	5.88	5.32	5.84
$_{59}$Pr	0.822±0.042	0.828	0.809	0.827	5.61±0.29	5.81	5.24	5.72
$_{60}$Nd	0.809±0.041	0.833	0.812	0.823	5.23±0.27	5.99	5.32	5.61
$_{62}$Sm	0.814±0.042	0.827	0.805	0.816	5.38±0.27	5.77	5.13	5.41
$_{63}$Eu	0.839±0.043	0.824	0.804	0.812	6.22±0.32	5.68	5.10	5.31
$_{64}$Gd	0.806±0.041	0.827	0.802	0.809	5.16±0.26	5.78	5.05	5.23
$_{65}$Tb	0.791±0.040	0.819	0.795	0.805	4.78±0.24	5.52	4.88	5.14

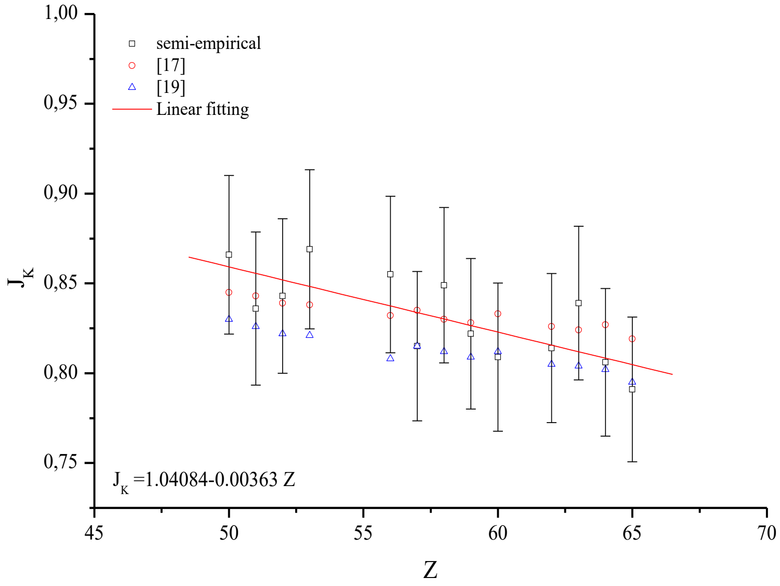

Figure 1. The semi-empirical K-shell absorption jump factors versus atomic number

According to Figure 1, it can easily be seen that the semi-empirical values change within experimental error limit but in verse K shell absorption jump ratios show different tendency. These semi-empirical values are 0%-16% compatible with the values of Broll [17] and 0%-37% compatible with the values of McMaster [19]. The biggest compatibility ratio was obtained for iodine element and the smallest compatibility ratio was obtained for Sb and Pr element. When the fitted values are compared with the other theoretical values, it can be concluded that K shell absorption jump ratios are 0%-10% different from Broll and 0%-20% different from McMaster.

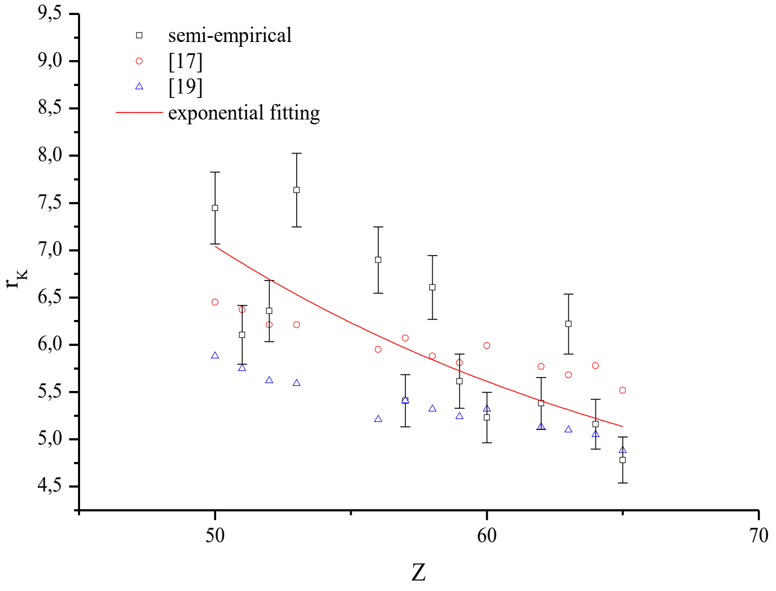

Figure 2. The semi-empirical K-shell absorption jump ratios versus atomic number

According to Figure 2, it can be easily seen that the fitting polynomial is appropriate with the exponential growth as written below.

$$y = A_1 e^{(x/t_1)} + y_0 \tag{5}$$

In which the vertical (y) and horizontal (x) components define K shell absorption jump-ratios and atomic number of elements respectively. In exponential fitting polynomial (r^2=0.55 and χ^2=4.33), all constants are showed as Table 2.

Table 2. The constant values of exponential fitting

Constants	**Values**
y_0	3.7175±2.65168
A_1	56.45878±150.92434
t_1	-17.6687±21.3092

The overall estimated errors are calculated as the quadrature sums of uncertainties obtained as 6% causing from the counting statistic (≤3%), efficiency determination (≤2%), the absorption coefficient (≤2) and non-uniform thickness (≤3).

Finally, K- shell X-ray production cross-section values are useful for the determination of radiation absorption parameters defined as K shell absorption jump-ratio and jump factor. These reported data will supply more semi-empirical and fitted data for studied parameters and it is needed more studies about the calculation and measurement of K shell absorption-jump ratio and jump factor for further checking of reliability of the studied parameters by using EDXRF and other experimental methods.

4. REFERENCES

1. Kacal, M.R., Han, I., Akman, F. 2015. Measurements of K shell absorption jump factors and ratios using EDXRF technique. Eur. Phys. J. D, 69, 103-109.

2. Tursucu, A., 2019. K shell absorption jump ratios and jump factor measurements for some elements in the range of 40 ≤ Z ≤ 50. Can. J. Phys., 97, 786-790.

3. Kaya, N., Tirasoglu, E., Apaydin, G., Aylikci, V., Cengiz, E. 2007. K shell absorption jump factors and jump ratios in elements between Tm(Z=69) and Os(Z=76) derived from new mass attenuation coefficient measurements. Nucl. Instrum. Meth. B, 262, 16-23.

4. Sidhu, B.S., Dhaliwal, A.S., Mann, K.S., Kahlon, K.S. 2011. Measurement of K shell absorption edge jump factors and jump ratios of some medium Z-elements using EDXRF technique. Radiat. Phys. Chem., 80, 28-32.

5. Kaya, N., Tirasoglu, E., Apaydin, G. 2008. K shell absorption jump factors and jump ratios in elements between Tm(Z=69) and Os(Z=76) by measuring K shell fluorescence parameters.Nucl. Instrum. Meth. B, 266, 1043-1048.

6. Kacal, M.R., Han, I., Akman, F. 2015. Determination of K shell absorption jump factor and jump ratios of 3d transition metals by measuring K shell fluorescence yields. Applied Radiation and Isotopes, 95, 193-199.

7. Kaya, N., Tirasoglu, E., Apaydin, G. 2011. Measurement of K shell jump ratios and jump factors for some elements in 76 ≤ Z ≤ 92 using EDXRF spectrometer. Radiat. Phys. Chem., 80, 677-681.

8. Akman, F., Durak, R., Turhan, M.F., Kaçal, M.R. 2015. Studies on effective atomic numbers, electron densities from mass attenuation coefficients near the K edge in some samarium compounds. Applied Radiation and Isotopes, 101, 107-113.

9. Akman, F., Durak, R., Kaçal, M.R, Bezgin, F. 2016. Study of absorption parameters around the Kedge for selected compounds of Gd. X Ray spectrom., 45, 103-110.

10. Akman, F., Durak, R., Kaçal, M.R. 2016. Chemical effect on the K shell absorption parameters of some selected cerium compounds. J.Inst., 11, P08006.

11. Akman, F., Gecibesler, I.H., Kumar, A., Sayyed, M.I., Zaid, M.H.M. 2019. Evaluation of radiation absorption characteristics in different parts of some medicinal aromatic plants in the low energy region. Results in Physics, 12, 94-100.

12. Oto, B., Yıldız, N., Akdemir, F., Kavaz, E. 2015. Investigation of gamma radiation shielding properties of various ores. Progress in Nuclear Energy, 85, 391-403.

13. Sayyed, M.I., Akman, F., Kacal, M.R., Kumar, A. 2019. Radiation protective qualities of some selected lead and bismuth salts in the wide gamma energy region. Nuclear Engineering and Technology, 51, 860-866.

14. Aylikci, N.K., Aylikci, V., Kahoul, A., Tirasoglu, E., Karahan, I.H., Cengiz, E. 2011. Effect of pH treatment on K-shell X-ray intensity ratios and K-shell X-ray production cross-sections in ZnCo alloys. Phys. Rev. A, 84, 042509.

15. Aylikci, V. 2015. K shell and L shell photoeffect cross-sections of some elements in the atomic range 50<=Z<=65. Spectropy and Spectral Analysis, 35, 29-33.

16. Krause, M.O., 1979. Atomic Radiative and Radiationless yields for K and L shells. J. Phys. Chem. Ref. Data, 8, 307-327.

17. Broll, N., 1986. Quantitative X-ray Fluorescence analysis, Theory and Practice of the Fundamental Coefficient Method. X-ray Spectrom., 15, 271-285.

18. Scofield, J.H. TheoreticalPhotoionization Cross Sectionsfrom*1 to 1500 keV*. United States. doi:10.2172/4545040.

19. Mc Master, W.H., Kerr Del Grande, N., Malett, J.H., Hubbell, J.H., 1969. Report UCRL-50174, Section II, Rev.1. Lawren

K-shell Photo-effect Cross-Sections of elements between the range 29≤Z≤74 using 123.6 keV Gamma-Ray Photons

Nuray Kup Aylikci†[1], **T. Depci**[2]
[1]*Iskenderun Technical University-ISTE, Dept. of Energy Systems Engineering, 31200, Iskenderun, Hatay, Turkey*
[2]*Iskenderun Technical University-ISTE, Dept. of Engineering Sciences, 31200, Iskenderun, Hatay, Turkey*
Corresponding Author: nuray.aylikci@iste.edu.tr

Abstract

Determination of the gamma or X-ray absorption ability of materials has gain popularity due to technological developments in different scientific areas such as nuclear energy materials, radiation dosimetry, health physics, and etc. It is possible to determine them using energy dispersive X-ray fluorescence. This method is an easy, practical and non-destructive method. In this study, X-ray florescence method was used to calculate total atomic K-shell photo-effect cross sections and photo-effect cross-sections using experimental K_α X-ray production cross-section values. For experimental measurements, the elements were irradiated by 123.6 keV gamma rays from ^{57}Co annular radioactive source. The emitted K X-rays were counted by an Ultra-LEGe detector with a resolution of 150 eV at 5.9 keV. The semi-empirical calculated values were compared with the data in the literature. The uncertainties in the measurements were calculated to be less than 6% for K_α X-ray production cross-section values and good agreement was obtained.

Keywords: Total atomic photo-effect cross-sections, K shell photo-effect cross-sections, ^{57}Co radioactive source

---

1. INTRODUCTION

Photo-electric effect or photo-effect is defined as the photon absorption by a target atom resulting in an atomic electron emission or an excited state of an atom. Especially for low photon energies, the most probable process is photoelectric absorption and the values of atomic absorption cross-sections for inner shells are necessary for the radiation physics, nuclear physics, dosimetry, shielding materials, elemental analysis of materials using X-ray fluorescence methods.

It can be found different studies about the calculation or measurement photo-effect cross-section values at different energies for different elements. For rare earth elements, a method was explained which not required any knowledge of the other process contributions. K shell photo-effect cross-sections were determined by using log-log plot of the measured total attenuation cross-sections for varying energy ranges between 52 and 84 keV [1]. Using the experimental mass attenuation coefficient values of beryllium, carbon, silicon and copper, atomic photo-effect cross-sections were derived for different energies. The results were compared with the theoretical values of Scofield and it was emphasized that the total atomic photo-electric absorption cross-section values could be measured by using energy dispersive methods [2]. From Tb to U, K shell, L shell and sub-shell, M shell and sub-shell photo-effect cross-sections were determined from the measured K X-ray production cross-sections at 123.6 keV [3]. For twenty four elements between the atomic region Z=40 and Z=68, K and L shell photo-effect cross-sections were measured at 59.537 keV photon energy [4]. Total atomic attenuation, total atomic photoelectric and total atomic scattering cross-sections were investigated for Gd, Tb, Dy and Er elements at 60 keV using Si(Li) semi-conductor detector [5]. Apart from these studies, several investigations can be found related with the photon absorption of elements or materials in different energy ranges [6-10].

In this study, energy dispersive X-ray fluorescence method was used for the calculation of total K shell photo-effect absorption cross section and K shell photo effect cross sections were determined semi-empirically by using the measured K_α X-ray production cross-section values. These data will provide more information about the absorption behavior of any materials against radiation exposure and also theoretical models to understand the complexity structure of atomic shells.

2. MATERIAL AND METHODS

2.1. Experimental Measurements

The thin films examined in this study were prepared by distributing powder samples as homogeneous as possible on the Mylar film at different thicknesses (20-40 mg/cm^2). The prepared thin films were placed in the experimental geometry to be stimulated by radioactive source and to count the characteristic X-rays that occurred. The geometry of experimental set-up is the same as in our previous study [11] and the produced thin films were irradiated with

123.6 keV energy X-rays released from a filtered ^{57}Co radioactive source. The energy of released X-rays was determined to be larger than K shell absorption edge. The emitted X-rays from the irradiated thin films were counted by an Ultra-LEGe detector whose FWHM was 150 eV at 5.9 keV. The obtained K shell spectra were analyzed by using Origin Company software program using least square fitting module.

2.2. Data Analysis

The absorption parameters were semi-empirically determined measuring K_α X-ray production cross-section values and calculated by the following relation,

$$\sigma_{K\alpha} = \frac{N_{K\alpha}}{I_0 G \varepsilon_{K\alpha} \beta_{K\alpha} m_i} \tag{1}$$

In which $N_{K\alpha}$ is the measured intensity (area under the photo-peak) corresponding to the K_α X-rays, I_0 is the intensity of the incident radiation, G is the geometric factor, $\varepsilon_{K\alpha}$ is the detection efficiency for the K_α X-rays, $\beta_{K\alpha}$ is the self-absorption correction factor for the target material, which accounts for the absorption in the target of the incident photons and the emitted characteristic X-rays and m_i is the thickness of the target in g/cm^2.The detailed information about the detector geometry, detector efficiency and self-absorption correction factor were explained as in our previous study [11].

The total atomic photo-effect cross-sections $\tau_{pe}(i)$ were calculated by the following equation:

$$\tau_{pe} = \frac{\sigma_{K\alpha}}{(1-1/r_K)\omega_K}\left(1+\frac{I_{K\beta}}{I_{K\alpha}}\right) \tag{2}$$

in which $\sigma_{K\alpha}$ is taken from the experimental values of Ref [12]. r_K, ω_K and $I_{K\beta}/I_{K\alpha}$ are absorption jump ratio, fluorescence yield and intensity ratio values, respectively. r_K values were calculated from the mass attenuation coefficient values from XCOM [13],

ω_K is the K shell fluorescence yield values taken from Krause [14] $I_{K\beta}/I_{K\alpha}$ is the theoretical intensity ratio values taken from Scofield [15]. The photo-effect cross-section values were calculated with using the following relation:

$$\tau_K = \tau_{pe}(1-1/r_K)$$

In this relation is calculated by using Eq.1 and r_K values were taken from Broll's values [16] in which the fit equation was determined as;

$$J_K = 0{,}915 - 0{,}0014Z \tag{4}$$

3. RESULTS AND DISCUSSIONS

The semi-empirical, theoretical and fitted values of studied pure elements in the range of $29 \leq Z \leq 74$ at 123.6 keV were given in Table 1. The fitted values were calculated by fourth-order polynomial obtained from the plot of the parameters versus atomic number (Figs 1 and 2). According to the results, the semi-empirical total atomic absorption photo-effect cross-section (τ_{pe}) values agree to within 3-6% and the fitted values are 0-10% compatible with the theoretical values of Scofield [17]. As for K shell photo-effect cross-sections (τ_K), the semi-empirical and the fitted values agree to within 0.7-7% and 0.1-7% respectively. In this study, compatibility ratio will be explained as a percentage change of the semi-empirical and the fitted values according to the theoretical values in the literature. The comparison of these values is important for testing the reliability of semi-empirical calculation method. Also, to test the reliability of the results, the semi-empirical values were plotted as function of atomic number and two new fitting polynomials were obtained in which the r^2 values equal to 0.99.

Table 1. The semi-empirical values of total atomic absorption photo-effect cross-sections (τ_{pe}) and K shell photo-effect cross section (τ_K) values of pure elements

Elements	τ_{pe}			τ_K		
	Semi-empirical	Theoretical [17]	Fitted	Semi-empirical	Theoretical [17]	Fitted
$_{29}$Cu	0.1474±0.0075	0.1200	0.1475	0.1288±0.0066	0.1352	0.1286
$_{33}$As	0.2149±0.0110	0.2235	0.2146	0.1850±0.0094	0.1991	0.1861
$_{44}$Ru	0.5521±0.0282	0.5556	0.5229	0.4704±0.0240	0.4858	0.4551
$_{48}$Cd	0.6791±0.0346	0.7133	0.6928	0.5745±0.0293	0.6193	0.5963
$_{52}$Te	0.9122±0.0465	0.8681	0.8956	0.7653±0.0390	0.7480	0.7601
$_{56}$Ba	1.1314±0.0577	1.0835	1.1290	0.9368±0.0478	0.9262	0.9450
$_{60}$Nd	1.4059±0.0717	1.3524	1.3890	1.1711±0.0597	1.1466	1.1484
$_{64}$Gd	1.6476±0.0840	1.5915	1.6693	1.3625±0.0695	1.3374	1.3670
$_{68}$Er	1.9459±0.0992	1.8843	1.9611	1.5917±0.0812	1.5689	1.5962
$_{72}$Hf	2.2558±0.1150	2.1845	2.2538	1.8417±0.0939	1.8012	1.8309
$_{74}$W	2.4096±0.1229	2.3492	2.3966	1.9386±0.0989	1.9250	1.9485

Figs. 1 and 2 show the plot of total atomic absorption photo-effect cross-section and K shell photo-effect cross section values versus atomic number respectively. The bars in the figures show the experimental error limits. In this study, the uncertainties in the measurements are estimated to be less than 6% for the measurement of K_α X-ray production cross-section and also semi-empirical total atomic photo-effect cross-section values. The experimental error limits (or uncertainties) of K shell photo-effect cross-section values are estimated to be less than 11% that come from the semi-empirical τ_{pe} calculation. As seen in Figs. 1 and 2, the semi-empirical values change within the experimental error limits in the case of comparison with the theoretical values of Scofield [17]. And so, it can be concluded that, the semi-empirical calculations of total atomic absorption photo-effect cross-section and K shell photo-effect cross-section values are probable measuring only K_α X-ray production cross-section values of elements.

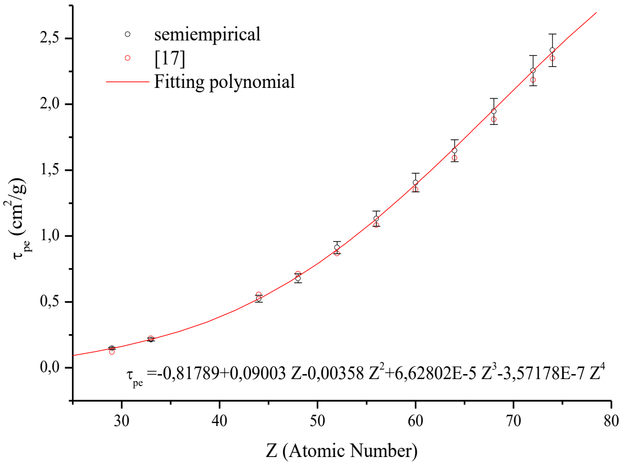

Figure 1. Total atomic absorption photo-effect cross section values versus Z

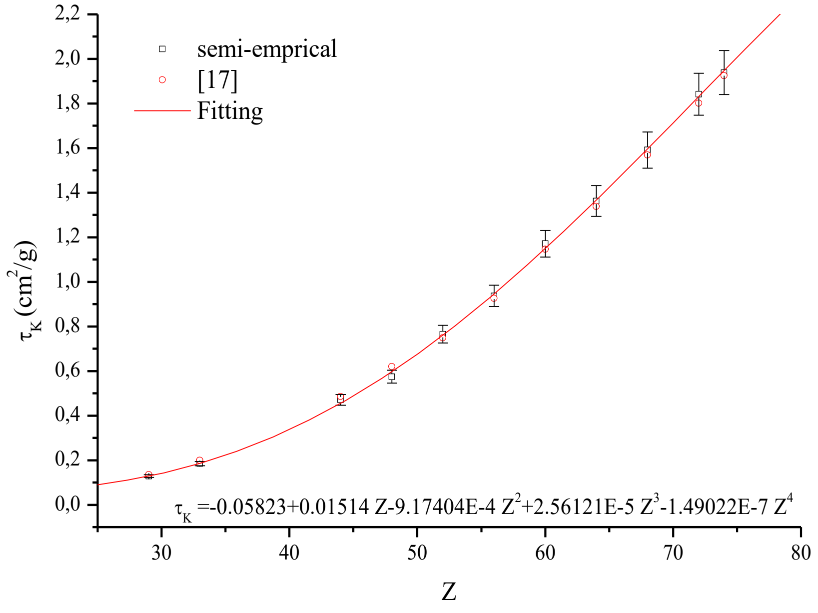

Figure 2. K shell photo-effect cross-section values versus

Finally, it should be noted that, the photoelectric effect occur with lower probability for low-atomic-number elements due to its lower binding energies of electrons to the energy levels. The probability of photoelectric absorption will increase with the increment of atomic number. The relationship between the photoelectric absorption and the atomic number is generally explained as follows;

$$\tau = \frac{C.Z^{4.5}}{E_\gamma^{\ 3}} \qquad (5)$$

In this relation C is a constant, Z is atomic number and E_γ is the incident photon energy. According to this relation, photoelectric absorption is inversely proportional to the incident photon energy. This means that the photoelectric absorption is dominant for low photon energies. In this study, the incident photon energy is selected as a constant value and so the fitting polynomial obtained for the total atomic absorption photo-electric cross-section is also compatible with Eq. 5.

The obtained data in this study will shed light for the development of new materials having radiation shielding property and also theoretical models to understand the complexity structure of atomic shells. To test the reliability of different theoretical and experimental studies, more data about these parameters should be included to the literature.

4. REFERENCES

1. Mallikarjuna, M.L., Appaji Gowda, S.B., Ganesh, K.E., Gowda, R., Umesh, T.K. 2004. A method to determine the K-shell photoeffect cross sections of some rare earth elements. Nucl. Instrum. Meth. B, 215, 4-8.

2. Gerward, L. 1989. Atomic photoeffect cross sections for beryllium, carbon, silicon and copper from 5 to 20 keV. J. Phys. B: At. Mol. Opt. Phys., 22, 1963-1969.

3. Kaya, N., Apaydin, G., Aylikci, V., Cengiz, E., Tirasoglu, E. 2008. K shell, L shell–subshell and M shell–subshell photoeffect cross-sections in elements between Tb and U at 123.6 keV. Radiat. Phys. Chem., 77, 101-106.

4. Karabulut, A., Gürol, A., Budak, G., Ertugrul, M. 2005. K shell and L subshell and L shell photoeffect cross-sections in the atomic region $40\leq Z\leq 52$ and $58\leq Z\leq 68$ keV. Nucl. Instrum. Meth. B, 227, 485-489.

5. Ertugrul, M., Simsek, O., Dogan, O., Turgut, U. 1996. Direct Determination Of Total Atomic Attenuation, Total Atomic Photoelectric And Total Atomic Scattering Cross Sections Of Gd, Tb, Dy And Er At 60 keV. J.Radioanal.Nucl.Chem. Letters, 213, 37-44.

6. Umesh, T.K., Anasuya, S.J., Shylaja Kumari, J., Gowda, C., Gopinathan Nair K.P., Gowda, R. 1992. Photoeffect cross sections of several rare-earth elements for 323-keV photons. Phys. Rev. A, 45, 2101-2103.

7. Chantler C.T. 2000. Detailed Tabulation of Atomic Form Factors, Photoelectric Absorption and Scattering Cross Section, and Mass Attenuation Coefficients in the Vicinity of Absorption Edges in the Soft X-Ray (Z=30–36, Z=60–89, E=0.1 keV–10 keV), Addressing Convergence Issues of Earlier Work. J. Phys. Chem. Ref. Data, 29, 597-1048.

8. Angelone, M., Bubba, T., Espasito, A. 2001. Measurement of the mass attenuation coefficient for elemental materials in the range $6\leq Z\leq 82$ using X-rays form 13 up to 50 keV. Applied Radiation and Isotopes, 55, 505-511.

9. Alam, M.N., Miah, M.M.H., Chowdhury, M.I., Kamal, M., Ghose, S., Rahman, R. 2001. Attenuation coeffcients of soils and some building materials of Bangladesh in the energy range 276-1332 keV. Applied Radiation and Isotopes, 54, 973-976.

10. Mallikarjuna, M.L., Appaji Gowda, S.B., Krishnaveni, S., Gowda R., Umesh, T.K. 2002. Studies on Photon Interaction Around the K-Edge of Some Elements. Nuclear Science and Engineering, 140, 96-102.

11. Aylikci, N.K., Aylikci, V., Kahoul, A., Tirasoglu, E., Karahan, I.H., Cengiz, E. 2011. Effect of pH treatment on K-shell X-ray intensity ratios and K-shell X-ray production cross-sections in ZnCo alloys. Phys. Rev. A, 84, 042509.

12. Aylikci, N.K. 2019. Semi-empirical determination of $K_{\alpha 1,2}$, $K_{\beta 1,3}$, and $K_{\beta 2,4}$ X-ray natural line widths for various elements between $29 \leq Z \leq 74$ at 123.6keV. Spectrosc. Lett., 52, 346-355.

13. Berger M.J. and Hubbell J.H., XCOM: Photon cross-sections on a personel computer (version 1.2), NBSIR85-3597, National Bureau of Standarts, Gaithersburg, MD, USA, for version 3.1, 1999, see http://physics.nist.gov/.

14. Krause, M.O., 1979. Atomic Radiative and Radiationless yields for K and L shells. J. Phys. Chem. Ref. Data, 8, 307-327.

15. Scofield, J.H., 1974. Relativistic Hartree-Slater Values for K and L X-ray Emission Rates. At. Data Nucl. Data Tables., 14, 121-137.

16. Broll, N., 1986. Quantitative X-ray Fluorescence analysis, Theory and Practice of the Fundamental Coefficient Method. X-ray Spectrom., 15, 271-285.

17. Scofield, J.H. Theoretical Photoionization Cross Sections from *1 to 1500 keV*. United States. doi:10.2172/4545040.

International Conference on Condensed Matter and Materials Science
ICCMMS-2019
14-19 October 2019
ADANA, TURKEY

Synthesis and Characterization of a Quinoxaline and Benzodithiophene Comprising Multifunctional Polymer

Serife O. Hacioglu[1*], Mustafa Yasa[2], Tolga Depci[1], Seza Goker[3], Levent Toppare[2,3,4,5]

[1]*Iskenderun Technical University, Department of Engineering Science, 31200, Hatay, Turkey*
[2]*Department of Polymer Science and Technology, Middle East Technical University,06800 Ankara, Turkey*
[3]*Department of Chemistry, Middle East Technical University, 06800 Ankara, Turkey*
[4]*Department of Biotechnology, Middle East Technical University, 06800 Ankara, Turkey*
[5]*The Center for Solar Energy and Applications, Middle East Technical University,06800 Ankara, Turkey*
Corresponding author: serife.hacioglu@iste.edu.tr

Abstract

Conducting polymers have gained great interest recently due to their fascinating properties such as; solution processability, easy band gap alternation via structural modification, low cost and flexibility. Conducting polymers have variety of application fields like solar cells (OPVs), electrochromic devices, biosensors and light emitting diodes. Up to date, the donor-acceptor (D-A) approach is verified to be the most efficient strategy in the synthesis of conducting polymers to obtain low band gap polymers for desired applications. Recently, quinoxaline and benzodithiophene units are widely used for donor and acceptor type aromatic heterocycles to achieve low band gap polymers. Herein, a novel multifunctional quinoxaline and benzodithiophene comprising polymer, namely poly[5-(5-(4,8-bis ((2-ethylhexyl)oxy) benzo[1,2-b:4,5-b']dithiophen-2-yl) selenophen-2-yl)-2,3-bis (3,4-bis(octyloxy)phenyl)-8-(selenophen-2-yl)quinoxaline], with selenophene-bridge was synthesized. The resulting polymer was characterized with electrochemical, spectroelectrochemical and electrochromic studies. The polymer exhibited low oxidation potential at 0.76 V with 1.74 eV optical band gap and multichromic redox states. These properties make the polymer a good candidate for electrochromic applications.

Keywords: Quinoxaline, benzodithiophene, copolymer, electrochromism

1. INTRODUCTION

Conducting polymers are glamorous materials which attract so many researchers due to numerous advantages like processability, low cost, lightweight, and ease of structural modifications [1-4]. These fascinating behaviors make these materials applicable in the next generation electronics such as; electrochromic devices, optoelectronic applications, biosensors and thin film transistors [5-8]. Band gap (E_g), redox behaviors, switching times and HOMO-LUMO energy levels are crucial parameters that affect the application performances of these functional materials and so the synthesis of novel low band gap conducting polymers by tailoring electrochemical and optical properties is the main purpose of the researchers in the field. Although different methodologies were applied by researchers for the synthesis of conducting polymers with desired and controllable optical behaviors namely; bond length alternation, planarity, interchain variance, resonance effect, various pendant groups and donor-acceptor approach, the latter one has obvious advantages and widely used in literature

[9]. Donor-acceptor theory based on the assembling of an electron rich donor unit with a high HOMO level and an electron deficient acceptor unit with a low LUMO level in the polymer chain tailors the physicochemical characters [10].

Molecular engineering is an emerging field of study for the synthesis of promising and multifunctional polymers. Up to now, carefully designed D-A type polymers comprising electron rich carbazole, fluorene, dithienopyrrole and benzodithiophene (BDT) and containing electron poor benzothiadiazole (BT), thienopyrroledione (TPD), benzotriazole (BTz) and quinoxaline derivatives (Qx) exhibited attractive physicochemical behaviors [11-14]. Between these units, quinoxaline have tremendous advantages namely, stable quinoid form, strong electron-withdrawing ability, easy preparation and functionalization which increase its popularity in the field [15,16]. Furthermore, with its excellent electron donating behavior, planar structure, easy π-π stacking ability and the low-lying HOMO energy levels, BDT comprising polymers exhibited desired optical properties [17,18]. In the light of these knowledge, Qx and BDT bearing multifunctional copolymer bearing selenophene as π-bridge was designed and synthesized via Stille coupling reaction. Optical, electrochemical and electrochromic studies were performed by means of UV-Vis-NIR spectrophotometer and cyclic voltammetry (CV) techniques and the resulting copolymer exhibited low oxidation potential at around 0.75 V with 1.74 eV optical band gap and multichromic behaviors.

2. MATERIAL AND METHODS

2.1. Experimental Measurements and Characterizations

All chemicals were purchased from Sigma Aldrich and used without any purification. Electrochemical studies were performed in a three-electrode cell consisting of an indium tin oxide (ITO)-coated glass slide as the working electrode (WE), platinum wire as the counter electrode (CE), and Ag wire as the reference electrode (RE). Gamry Reference 600 Potentiostat and Varian Cary 5000 UV-Vis Spectrometer were used for electrochemical, spectroelectrochemical and electrochromic switching studies in 0.1 M tetrabutylammonium hexafluorophosphate ($TBAPF_6$), acetonitrile (ACN) electrolytic medium.

2.2. Synthesis

The syntheses of 2,3-bis (3,4-bis(octyloxy)phenyl)-5,8-bis (5-bromoselenophen-2-yl) quinoxaline **(M)** was previously reported [19]. Synthetic pathway for the polymer is illustrated in Scheme 1.

2.3. Synthesis of the polymer [Poly (5-(5-(4,8-bis((2-ethylhexyl)oxy)benzo[1,2-b:4,5-b']dithiophen-2-yl)selenophen-2-yl)-2,3-bis(3,4-bis(octyloxy)phenyl)-8-(selenophen-2-yl)quinoxaline)]

In a two-necked flask under argon atmosphere and charged with a magnet bar, **M** (0.2 g, 0.165 mmol), **BDT** (0.13 g, 0.165 mmol), $Pd_2(dba)_3$ (5 %) and P(o-tolyl) (12 %) were dissolved in dry toluene (15 mL). Reaction mixture was stirred at 100 °C for 6 days. Chlorobenzene (0.2 mL) and tributyl(selenophen-2-yl) stannane (0.4 mL) were added as end cappers. The mixture was cooled to ambient atmosphere and solvent was removed under reduced pressure. After addition of cold methanol, the mixture was kept in refrigerator overnight. Sodium diethyl-dithiocarbamate trihydrate (10 mg) as Pd scavenger was added and left to stir for 1h. Following the filtration, crude product was washed in a Soxhlet extractor with acetone and hexane in order to remove low molecular weight fractions. The polymer was collected with chloroform fraction. Solvent was removed under reduced pressure. The polymer was recrystallized from cold methanol to obtain dark indigo crystals. Yield: 55 mg, 22 %.

^{1}H NMR (400 MHz, $CDCl_3$): δ: 7.52 (Qx), 7.31(Phenyl group), 6.96-6.76 (Qx, Fused Thiophene), 4.07-3.84(-OCH_2), 2.17-1.83(EH), 1.32-1.10(-CH_2-), 0.89-0.81(-CH_3)

Mn: 20000 Da, Mw: 30000 Da, PDI: 1.5

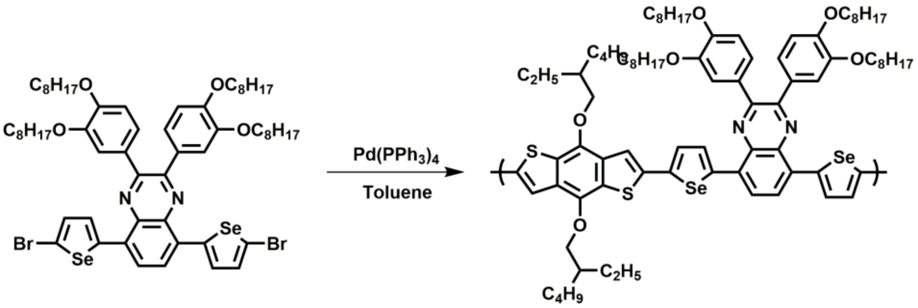

Scheme 1. Synthetic pathway for the polymer

3. RESULTS AND DISCUSSIONS

3.1. Electrochemical studies:

Optimum band gap and proper alignment of HOMO (the highest occupied molecular orbital) and the LUMO (the lowest occupied molecular orbital) energy levels are crucial parameters for conducting polymers to be applicable in different fields such as; solar cell, ECD and OLED applications. Cyclic voltammetry (CV) is a practical and eligible technique that was widely used for electrochemical characterizations.

Therefore, CV measurements were performed to explore the redox properties and HOMO–LUMO energy levels of the resulting polymer. The polymer was dissolved in chloroform (5 mg. mL^{-1}) and spray processed onto the indium tin oxide (ITO) coated glass slides. The measurements were conducted in three-electrode system where a polymer coated ITO electrode was used as the working electrode, a platinum (Pt) wire and a silver (Ag) wire electrodes were served as the counter and reference electrodes, respectively. During measurements, 0.1 M $TBAPF_6$/acetonitrile (ACN) electrolyte/solvent couple was used at a scan rate of 100 mV.s^{-1} and corresponding oxidation and reduction voltammograms were depicted in **Fig. 1**. As seen, synthesized polymer exhibits an ambipolar character in other words it has both p-type doping and n-type doping behaviors which make it a possible candidate for variety of applications. It has two well defined oxidation potentials in the anodic region of voltammogram at 0.76 V and 1.08 V with p-type de-doping potentials at 0.50 V and 0.84 V. Furthermore, two reversible reduction potentials were recorded at -1.44 V and -1.94 V in the cathodic region.

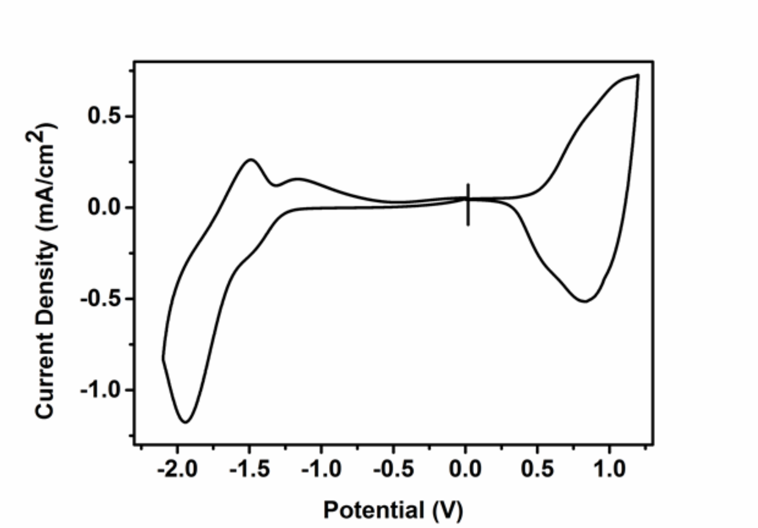

Figure 1. Single scan cyclic voltammogram of the polymer in a 0.1 M TBAPF$_6$, ACN solution at a scan rate of 100 mV.s^{-1}

As mentioned before, HOMO/LUMO energy levels are another important property for conducting polymers and they were calculated from the onsets of the corresponding oxidation/reduction potentials with Eqn. 1 and Eqn. 2 and reported as -5.22 eV and -3.23 eV, respectively.

$$\mathrm{HOMO} = -(4.75\ \mathrm{eV} + \mathrm{E}_{\mathrm{onset}}^{\mathrm{ox}}) \qquad \text{Eqn. 1}$$

$$\mathrm{LUMO} = -(4.75\ \mathrm{eV} + \mathrm{E}_{\mathrm{onset}}^{\mathrm{red}}) \qquad \text{Eqn. 2}$$

Scan rate studies were performed by recording the single scan CVs at four different scan rates (50 mV.s^{-1}, 100 mV.s^{-1}, 150 mV.s^{-1}, 200 mV.s^{-1}) and corresponding current density/scan rate relations were reported in **Fig. 2b**. Scan rate studies are important to test the effective charge injection-rejection process for the polymer film at different scan rates. As depicted in **Fig. 2b**, a linear correlation between the current density and the scan rate pointing out a non-diffusional controlled redox process with existence of the well adhered polymer films on the working electrode surface.

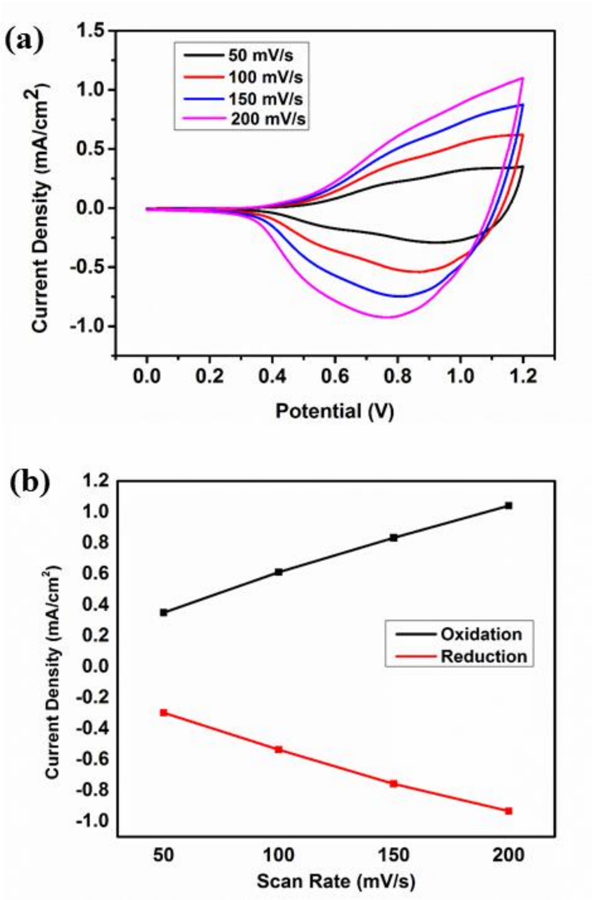

Figure 2. a) Single scan cyclic voltammograms and b) current density vs scan rate graph of the polymer in 0.1 M TBAPF$_6$/ACN solution

3.2. Spectroelectrochemical Characterizations:

Electronic and optical changes of synthesized polymer upon stepwise oxidation were determined via spectroelectrochemical experiments by using in situ UV–Vis-NIR spectrophotometer and potentiostat. To observe the optical changes at different doped states, the polymer was dissolved in chloroform (5 mg. mL^{-1}) and spray coated onto ITO substrate and analyses were performed by using 0.1 M TBAPF$_6$ as the supporting electrolyte in ACN. The optical band gap (Eg), λ_{max} and formation of polaronic bands which were important to characterize the conducting polymers and test their applicability in different fields were examined from electronic absorption spectra.

The polymer was initially reduced to its neutral state to record the true neutral state absorption and then oxidation was performed step wisely during spectroelectrochemical studies. The absorption maxima revealed at 600 nm with a shoulder at 630 nm for the resulting polymer and the corresponding optical band gap was calculated as 1.74 eV from the onset of this neutral state absorption. Furthermore, another absorption maximum was exhibited in the visible region at around 400 nm and existence of two absorption peaks in the red and blue regions of the visible spectrum resulted in a neutral state green polymer, which is a rare and desired property for electrochromic polymer.

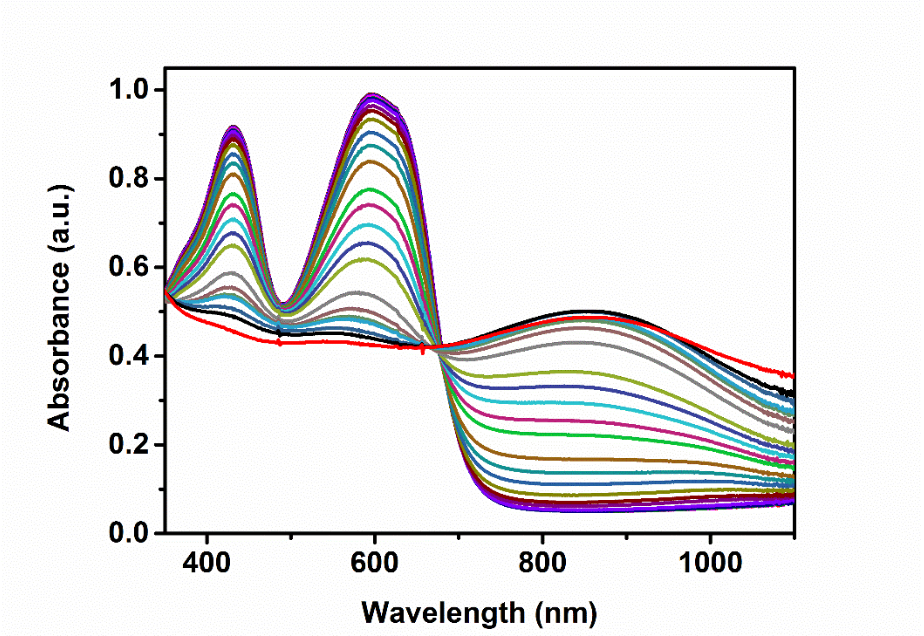

Figure 3. Change in the electronic absorption spectra of the polymer in 0.1 M TBAPF$_6$/ACN solution upon oxidative doping at potentials between 0.0 V and 1.2 V.

TABLE 1. Summary of electrochemical and spectroelectrochemical properties of the polymer

	$E_{p\text{-doping}}$ (V)	*$E_{p\text{-dedoping}}$ (V)*	*$E_{n\text{-doping}}$ (V)*	*$E_{n\text{-dedoping}}$ (V)*	*HOMO (eV)*	*LUMO (eV)*	*E_g^{ec} (eV)*	*λmax (nm)*	*E_g^{op} (eV)*
Polymer	**0.76/ 1.08**	**0.50/ 0.84**	**-1.44/ -1.94**	**-1.15/ -1.48**	**-5.22**	**-3.23**	**1.99**	**600/630**	**1.74**

Upon stepwise oxidation, while these peaks were decreased simultaneously in the visible region, new absorption band evolved at 850 nm as a result of charge carrier formation namely, polarons. Quinoxaline and BDT comprising copolymer exhibited an electrochromic property both in the p-doped and n-doped states. The polymer switched between green and gray colors in the neutral and oxidized states, respectively. As mentioned before, synthesized polymer showed a multichromic behavior in the n-doped state which is a rare property for these type of materials and increase their application fields. While the neutral state green color turned to orange after reduction via applying -2.0 V, the blue colored intermediate state was recorded at -1.8 V. Colors of the polymer in the neutral and oxidized/reduced states were depicted in **Fig. 4** with corresponding L, a, b values reported in Table 2. L, a, b values were reported according to CIE (Commission Internationale de l'Eclairage) coordinates which were widely used to report the colors of materials in a more scientific way. In CIE coordinates, 'L', 'a' and ‘b’ represent the brightness of the color, the color between red-green and the color between yellow-blue in the colorimetric measurements, respectively.

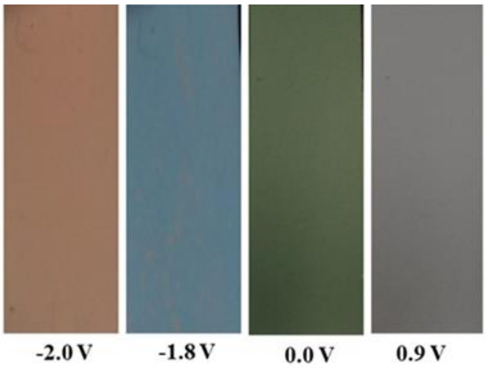

Figure 4. Colors of the polymer at neutral/oxidized states with intermediate colors.

TABLE 2. Colorimetric measurements of the polymer films at neutral/oxidized states.

Potential (V)	***L***	***a***	***b***
-2.0 V	54.44	18.42	22.33
-1.8 V	42.27	-12.07	-13.74
0 V	38.54	-11.51	12.98
0.9 V	50.01	0.250	1.391

3.3. Electrochromic Switching Studies:

Finally, electrochromic switching studies were performed to calculate and report other important parameters for ECDs applications namely, optical contrast and switching times. For the analysis, the polymer was dissolved and coated on an ITO electrode as described before and a square-wave potential method was conducted in 0.1 M TBAPF$_6$ / ACN solution by applying 0.0 V and 1.2 V potentials with 5 s intervals at maximum absorbance values determined from electronic absorption spectra as 600 nm and 850 nm. As summarized in Table 3 and depicted in **Fig. 5**, the polymer revealed 31 % (at 600 nm) and 18 % (at 850 nm) optical contrast values upon doping/de-doping processes. Finally, switching time which is the time required for one full switch of the polymer between two extreme states were calculated as 1.8 s and 1.3 s in the visible and NIR regions, respectively. These promising electrochemical and electrochromic results make the polymer a good candidate for ECD applications and as a future study this multifunctional polymer will be used for different applications.

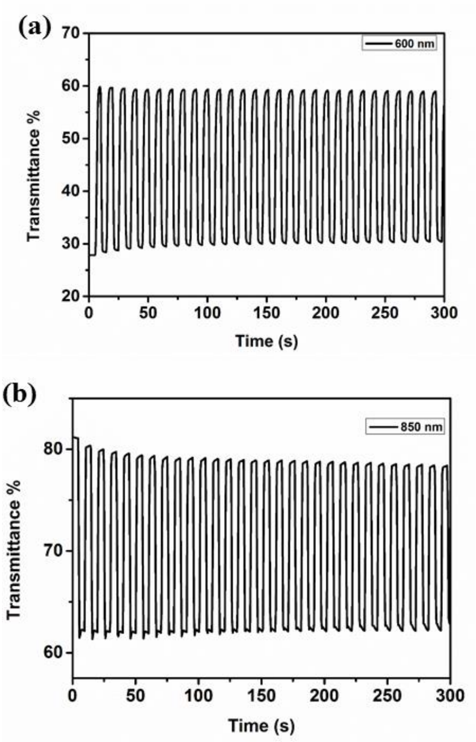

Figure 5. Kinetic studies of the polymer at a) 600 nm and b) 850 nm

4. CONCLUSIONS

In this study, a novel quinoxaline and benzodithiophene based D–A–D type copolymer with selenophene π-bridge was designed and synthesized via Stille coupling reaction. Optical, electrochemical and electrochromic properties were investigated with cyclic voltammetry and UV-Vis-NIR spectrophotometry. Summary of results showed that synthesized polymer exhibited ambipolar character with low oxidation potential at 0.76 V. Corresponding HOMO and LUMO energy levels were calculated as -5.22 eV and -3.23 eV, respectively. The polymer displayed electrochromic property and switched between green and gray colors in the neutral and oxidized states, respectively. Furthermore, multichromic behavior in the n-doped state which is a rare property for these type of materials was observed and the neutral state green color turned to orange after reduction via applying -2.0 V, the blue colored intermediate state was recorded at -1.8 V. Finally, as a result of kinetic studies, the polymer revealed 31 % (at 600 nm) optical contrast with a switching time of 1.8 s.

TABLE 3. Summary of kinetic studies of the polymer

	Optical Contrast (Δt %)		*Switching Times (S)*
Polymer	31	600 nm	1.8
	18	850 nm	1.3

5. REFERENCES

[1] Kumar, A., Welsh, D.M., Morvant, M.C., Piroux, F., Abboud, K.A., Reynolds, J.R., 1998, Conducting Poly(3,4-alkylenedioxythiophene) Derivatives as Fast Electrochromics with High-Contrast Ratios, Chem. Mater., 10, 896–902.

[2] Balan, A., Gunbas, G., Durmus, A., Toppare, L., 2008, Donor−Acceptor Polymer with Benzotriazole Moiety: Enhancing the Electrochromic Properties of the “Donor Unit”, Chem. Mater. 20, 7510–7513.

[3] Sapp, S. A., Sotzing, G.A., Reynolds, J.R., 1998, High Contrast Ratio and Fast-Switching Dual Polymer Electrochromic Devices, Chem. Mater. 10, 2101–2108.

[4] Roncali, J. 2007, Molecular engineering of the band gap of π-conjugated systems: Facing technological applications, Macromol. Rapid Commun., 28, 1761−1775.

[5] Schmidt, G. C., Höft, D., Haase, K., Hübler, A. C., Karpov, E., Tkachov, R., Stamm, M., Kiriy, A., Haidu, F., Zahn, D. R. T., Yan, H., Facchetti, A., 2014, Naphtalenediimide-based donor–acceptor copolymer prepared by chain-growth catalyst-transfer polycondensation: evaluation of electron-transporting properties and application in printed polymer transistors, J. Mater. Chem. C, 2, 5149 -5154.

[6] Soylemez, S., Hacioglu, S. O., Kesik, M., Unay, H., Cirpan, A., Toppare, L., 2014, A novel and effective surface design: Conducting polymer/β-cyclodextrin host-guest system for cholesterol biosensor, ACS Appl. Mater. Interfaces, 6, 18290−18300.

[7] Grimsdale,A.C., Chan, K.L., Martin, R.E., Jokisz, P.G., Holmes, A.B., 2009, Synthesis of light emitting conjugated polymers for applications in electroluminescent devices, Chem. Rev., 109, 897–1091.

[8] Thompson, B. C., Schottland, P., Zong, K., Reynolds, J. R., 2000, In situ colorimetric analysis of electrochromic polymers and devices, Chem. Mater., 12, 1563−1571.

[9] Wang, X., Chen, S., Sun, Y., Zhang, M., Li, Y., Li, X., Wang, H., 2011, A furan-bridged D-π-A copolymer with deep HOMO level: synthesis and application in polymer solar cells, Polym. Chem., 2, 2872 -2877.

[10] Havinga, E. E., Hoeve, W., Wynberg, H., 1993, Alternate donor-acceptor small-band-gap semiconducting polymers; Polysquaraines and polycroconaines, Synth. Met., 55, 299–306.

[11] Blouin, N., Michaud, A., Gendron, D., Wakim, S., Blair, E., Neagu-Plesu, R., Belletete, M., Durocher, G., Tao, Y., Leclerc, M., 2008, Toward a Rational Design of Poly(2,7-Carbazole) Derivatives for Solar Cells, J. Am. Chem. Soc., 130 (2)
732-742.

[12] Dou, L., Gao, J., Richard, E., You, J., Chen, C.-C., Cha, K.C., He, Y., Li, G., Yang, Y., 2012, Systematic Investigation of Benzodithiophene- and Diketopyrrolopyrrole-Based Low-Bandgap Polymers Designed for Single Junction and Tandem Polymer Solar Cells, J. Am. Chem. Soc.,134 (24), 10071-10079.

[13] Yang, J., Uddin, M.A., Tang, Y., Wang, Y., Wang, Y., Su, H., Gao, R., Chen, Z-K., Dai, J., Woo, H.Y., Guo, X., 2018, Quinoxaline-Based Wide Band Gap Polymers for Efficient Nonfullerene Organic Solar Cells with Large Open-Circuit Voltages, ACS Appl. Mater. Interfaces, 10, 23235-23246.
[14] Azeri, O., Aktas, E., Istanbulluoglu, C., Hacioglu, S. O., Cevher, S. C., Toppare, L., Cirpan, A., 2017, Efficient benzodithiophene and thienopyrroledione containing random polymers as components for organic solar cells, Polymer, 133,60−67.
[15] Zhang, Y., Kong, L., Du, H., Zhao, J., Xie, Y., 2018, Three novel donor-acceptor type electrochromic polymers containing 2,3-bis(5-methylfuran-2-yl)thieno[3,4-b]pyrazine acceptor and different thiophene donors: low-band-gap, neutral green-colored, fastswitching materials, J. Electroanal. Chem., 830-831, 7–12.
[16] Keshtov, M. L., Godovsky, D. Y., Kuklin, S. A., Nicolaev, A., Lee, J., Lim, B., Lee, H. K., Koukaras, E. N., Sharma, G. D., 2016, Synthesis and photophysical properties of semiconductor molecules D1-A-D2-A-D1-type structure based on derivatives of quinoxaline and dithienosilole for organics solar cells, Org. Electron. 39,361–370.
[17] Tessarolo, M., Gedefaw, D., Bolognesi, M., Liscio, F., Henriksson, P., Zhuang, W., Milita, S., Muccini, M., Wang, E., Seri, M., Andersson, M. R., 2014, Structural tuning of quinoxaline-benzodithiophene copolymers via alkyl side chain manipulation: synthesis, characterization and photovoltaic properties, J. Mater. Chem. A, 2, 11162–11170.
[18] Liu, D., Zhao, W., Zhang, S., Ye, L., Zheng, Z., Cui, Y., Chen, Y., Hou, J., 2015, Highly Efficient Photovoltaic Polymers Based on Benzodithiophene and Quinoxaline with Deeper HOMO Levels, Macromolecules, 48, 5172–5178.
[19] Yasa, M., Goker, S., Toppare, L., 2019, Selenophene-bearing low-band-gap conjugated polymers: tuning optoelectronic properties via fluorene and carbazole as donor moieties, Polym. Bull., https://doi.org/10.1007/s00289-019-02872-2

Sol-Gel Synthesis and Electron Paramagnetic Resonance (EPR) Spectroscopy of Cu^{2+} and Co^{2+} Doped $PbTiO_3$ Perovskites

Ebru Erünal
Cukurova University, Dept. of Chemical Engineering, 01330, Adana, Turkey
Email: eerunal@cu.edu.tr

Abstract

$PbTiO_3$ perovskites are widely used in many applications due to their ferroelectric and photocatalytic properties. In order to enhance these properties and provide sustainable usage of the materials, doping with certain transition metals is a very common method. By this way, defects are created in order to compensate the lattice charge equilibrium as a result of replacement of doping ion with the host ion. In this study, undoped and doped $PbTiO_3$ materials were synthesized through sol-gel method. The crystal structure was analyzed with XRD. Formation of perovskite structure was verified while decrease in crystal sizes after doping was observed. Moreover, X-Band Electron Paramagnetic Resonance (EPR) spectroscopy measurements were conducted to verify the incorporation of Co^{2+} and Cu^{2+} ions on Ti^{4+} sites. This shows a probable oxygen vacancy formation accompanying this substitution to provide the lattice charge balance.

Keywords: Perovskite, $PbTiO_3$, Oxygen Vacancy, EPR Spectroscopy

1. Introduction

The chemical and electronic properties of $PbTiO_3$ perovskite materials make them one of the most popular materials that are used in different applications [1-11]. For example, by doping with Zr dense materials with very good ferroelectric properties are obtained and widely used in industry. $PbTiO_3$ has also been used itself in different electronic devices like nonvolatile memories, infrared or ultrasonic sensors, surface acoustic wave filters, transducers, acoustic amplifiers, actuator applications [1-5]. Moreoever, due to Ti in the structure, the semi-conductor properties and ability to absorb visible solar light -unlike TiO_2 which absorbs light in UV region- make them attractive for photocatalytic purposes [11].

Lead titanate has tetragonal ferroelectric phase below the Curie temperature [1]. According to ABO_3 perovskite type, the 12-coordinated A ion with larger diameter corresponds to Pb^{2+} and 6-coordinated B ion with smaller ion corresponds to Ti^{4+}. The perovskite is shown in Figure 1.

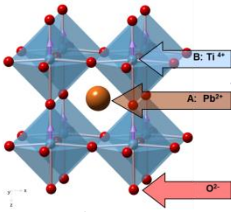

Figure 1. $PbTiO_3$ Perovskite: Larger ion Pb^{2+} neighboring with 12 oxygen atoms, smaller ion Ti^{4+} neighboring with 6 oxygen atoms

In order to get better material properties, a common strategy is doping the material with transition ions. By this way, in order to maintain the charge balance of the perovskite crystal structure is provided through the formation of oxygen vacancies, which lead to enhancement of ferroelectric, piezoelectric or catalytic properties. Generally, either A or B site is occupied by the dopant ions. Similar effective atomic radii are selected if A site or B site doping is aimed. In general, if lower charge ion is replaced by higher charge ion, formation of oxygen vacancies (V_O**) is observed while for opposite case cation vacancies are formed [12].

In case of doping the materials with paramagnetic ions, electron paramagnetic resonance (EPR) spectroscopy is an advantageous method to track the first coordination sphere of the paramagnetic dopant ion. Depending on the spin Hamiltonian parameters, each paramagnetic ion shows characteristic signals. However, powders might be hard to resolve the spectra due to their polycrystalline nature which will appear as the superposition of each crystalline that can be found in different orientations in a powder. At a fixed frequency, EPR signals are collected according to electronic and/or nuclear interaction of the varying magnetic field [13]. For example, in case of unpaired $3d^9$ electron like Cu^{2+}, the spin Hamiltonian with spin S = ½ interacting with N magnetic active nuclei of arbitrary spin I = 3/2 can be written as

$$H = \beta_e \mathbf{B}_0 \cdot \mathbf{g} \cdot \mathbf{S} - \beta_n \sum_{i=1}^{N} g_{n,i} \mathbf{B}_0 \cdot \mathbf{I}_i + \sum_{i=1}^{N} \mathbf{S} \cdot \mathbf{A}_i \cdot \mathbf{I}_i \qquad (1)$$

with g_n is the nuclear g-factor, β_e and β_n are the Bohr and nuclear magnetons, respectively. B_0 denotes the applied external magnetic field. The first and second terms represent the electronic and nuclear Zeeman interactions, where the last term is due to the copper hyperfine interaction with I^{Cu} = 3/2 for both copper isotopes with natural abundances ^{63}Cu (69.09%) and ^{65}Cu (30.91%). On the other hand, in case of unpaired $3d^7$ electron like Co^{2+}, the spin Hamiltonian with spin S = 3/2 interacting with N magnetic active nuclei of arbitrary spin I = 7/2 (high spin) with natural abundance ^{59}Co (100%). The general spin Hamiltonian of Co(II) ions in HS configuration is given by equation

$$H = \beta_e \mathbf{B}_0 \cdot \mathbf{g} \cdot \mathbf{S} + \sum_{i=1}^{N} \mathbf{S} \cdot \mathbf{D}_i \cdot \mathbf{S} - \beta_n \sum_{i=1}^{N} g_{n,i} \mathbf{B}_0 \cdot \mathbf{I}_i + \sum_{i=1}^{N} \mathbf{I}_i \cdot \mathbf{Q}_i \cdot \mathbf{I}_i + \sum_{i=1}^{N} \mathbf{S} \cdot \mathbf{A}_i \cdot \mathbf{I}_i \qquad (2)$$

Differently from other equation the D term refers to zero field splitting that appears for high spin systems [13].

2. Experimental

2.1 Materials

The metal precursors were used as following: $Pb(CH_3COO)_2.3H_2O$ (extra pure, MERCK) for lead, $Ti(OCH(CH_3)_2)_4$ (98%, Acros Organics) for titanium, $Co(II)(NO_3)_2.6H_2O$ (Carlo Erba) for cobalt, $Cu(CH_3COO)_2.H_2O$ (Carlo Erba) for copper. Acetate Tetrahydrate Citric acid (99%, Sigma Aldrich) was used as gelation agent. Ethanol (Merck, absolute for analysis), Acetic acid glacial (Merck) was used to dissolve materials. All materials were used without further purification.

2.2 Sol-Gel Synthesis

The synthesis procedure is shown in Figure.1. At room temperature, $Pb(CH_3COO)_2.3H_2O$ and $Ti(OCH(CH_3)_2)_4$ were dissolved in acetic acid glacial and a mixture of acetic acid glacial and ethyl alcohol, respectively in separate beakers. To obtain $Pb(Ti_xCo_{(1-x)})O_3$, Co precursor was added to Pb solution. Similarly, for $Pb(Ti_xCu_{1-x)})O_3$, Cu precursor was added. Then both solutions were mixed together under vigorous stirring. After complete dissolution, a solution of citric acid and ethanol is added to form the gel. Then, still at room temperature gel was kept under stirring and then transferred to hot plate which is kept around 50ºC. Cobalt containing gel turned into pink in color while copper containing gel turned into green-blue. After around 1 hour, the solidified gels were calcined at 100°C overnight. Finally, samples were placed into furnace at 650°C for 3 hours.

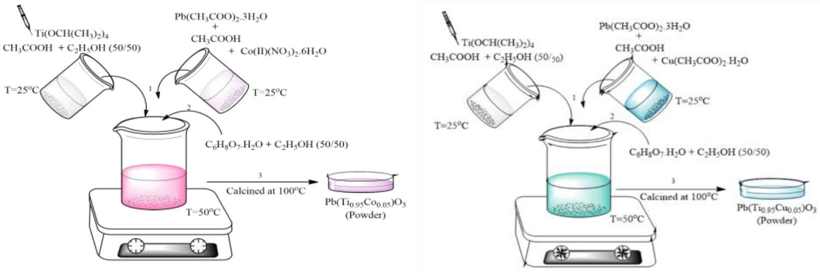

(a) (b)

Fig. 1. Sol-gel synthesis route for (a) $Pb(Ti_xCo_{(1-x)})O_3$ (b) $Pb(Ti_xCu_{(1-x)})O_3$

2.3. Material Characterization

The quantitative analysis of lead, copper and cobalt were done by ICP-OES (Perkin Elmer 2100 DV) while a Rigaku Miniflex X-Ray Diffraction (XRD) instrument (CuK_α ,λ= 0.154 nm) was used to verify the formation of preovskite structure. Electron paramagnetic resonance (EPR) measurements were conducted on an X-Band (9.5 GHz) Bruker EMX 081 EPR spectrometer at room temperature. The microwave power was 2.012 mW with a modulation amplitude of 2 G. Sweep width was chosen as 3000 G with a center field of 2800 G whose resolution corresponds to 1024 points.

3. Results and Discussion

ICP-OES results showed that Pb weight % was around 64.15, 77 and 75.2 % for $PbTiO_3$, $Pb(Ti_{0.5}Cu_{0.5})O_3$ and $Pb(Ti_{0.5}Co_{0.5})O_3$, respectively. Besides, Cu was 1.5% and Co was nearly 1.2%. Theoretical amounts of Pb was expected to be 68% and of doping ions 1%. Therefore, it shows that the obtained materials were slightly B-excess for $PbTiO_3$ while doped materials were B-excess. On the other hand, in terms of X-Ray Diffraction, this excess amounts might be seen due to slight broadening of sharp peaks that were obtained for undoped material. Still, the formation of perovskite structure can be observed for all materials as shown in Figure.2.

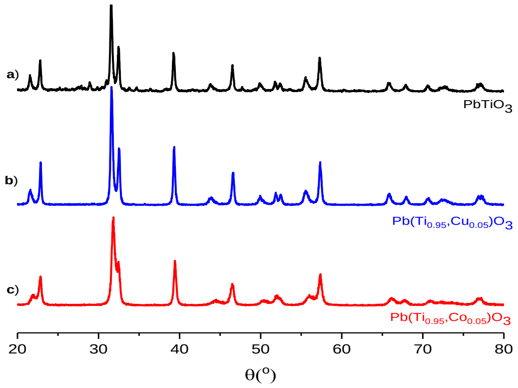

Figure-2. XRD spectra of (a) PbTiO3 (b) Pb$(Ti_{0.5}Cu_{0.5})O_3$ and (c) Pb$(Ti_{0.5}Co_{0.5})O_3$

X-Band EPR spectra of doped materials are given in Figure.3. The typical Cu^{2+} signal which addresses incorporation of dopant ion into Ti^{4+} (Fig. 3a). According to Kröger-Vink notation, the oxygen vacancy formation can be shown as

$$Cu_{Ti}'' + V_O^{\circ\circ} \leftrightarrow \mathit{nil}$$

This type of defect is epected to affect the ferroelectric and defect-induced strain parallel on one side of the domain wall and perpendicular on the other properties [14]. On the other hand, the Co doped material seems to exhibit low spin Co^{2+} center which would lead to the formation of a similar oxygen vacancy both according to other studies and obtained EPR spectra for Co doped different materials [15-19]. However, a higher frequency seems necessary to resolve Co doped material to make further interpretations.

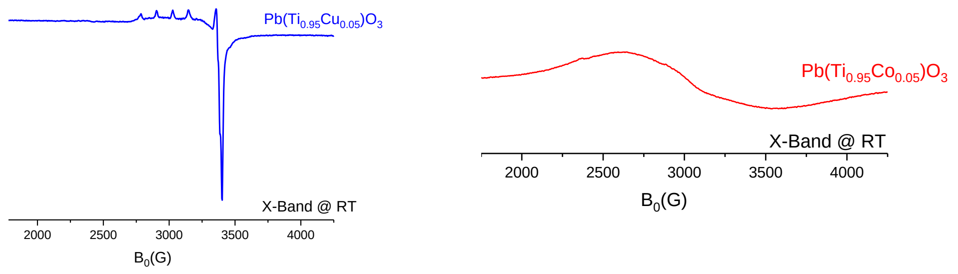

(a)

(b)

Figure-3. EPR spectra of (a) Pb$(Ti_{0.5}Cu_{0.5})O_3$ (blue in color) and (b) Pb$(Ti_{0.5}Co_{0.5})O_3$ (red in color)

4. Conclusions

The formation of perovskite structure for all materials was detected through XRD analysis. A broadening due to doping especially in case of cobalt was observed. The incorporation of Cu^{2+} into lattice in place of Ti^{4+} ion (B-site) results in formation of one oxygen vacancy were verified with room temperature X-Band EPR measurements. Co doped material seems to exhibit low spin Co^{2+} center due to X-Band EPR spectroscopy measurements. The incorporation of Co^{2+} into lattice in place of Ti^{4+} ion (B-site) seems favorable but a higher frequency EPR is necessary to resolve the broad peak obtained at X-Band.

Acknowledgements

This project is supported by Çukurova University FBA-2018-10647. Prof. Dr. Mustafa Polat from Hacettepe University and Prof. Dr. Ramazan Esen from Çukurova University are acknowledged for their contrubutions to EPR and XRD analysis. Also the author is deeply grateful for the endless supports of Prof. Dr. Bilgehan Güzel and Prof.Dr. Bekir Özçelik from Çukurova University.

References

[1] B. Jaffe, W. R. Cook and H. Jaffe, Piezoelectric Ceramics, Academic Press, London (1971).
[2] J. L. White, M. F. Baruch, J. E. Pander III, Y. Hu, I. C. Fortmeyer, J. E. Park, T. Zhang, K. Liao, J. Gu, Y. Yan, et al. Chem. Rev. 115, 12888 (2015).
[3] C. Liu, B. C. Colmon, M. Ziesack, P. A. Silver, and D. G. Nocera. Science 352, 1210 (2016).
[4] D. Uner and M. M. Oymak. Catal Today 181, 82 (2012).
[5] G. P. Smestad and A. Steinfeld, Ind. Eng. Chem. Res. 51, 11828 (2012).
[6] C. L. Muhich, B. W. Evanko, K. C. Weston, P. Lichty, X. Liang, J. Martinek, C. B. Musgrave, and A. W.Weimer, Science 341, 540 (2013).
[7] W. C. Chueh, C. Falter, M. Abbott, D. Scipio, P. Furler, S. M. Haile, and A. Steinfeld. Science 330, 1797 (2010).
[8] J. E. Miller, M. D. Allendorf, R. B. Diver, L. R. Evans, N. P. Siegel, and J. N. Stuecker. J. Mat. Sci. 43, 4714 (2008).
[9] F. Saladin and I. Alxneit, J. Chem. Soc., Faraday Trans. 93, 4159 (1997).
[10] A. M. Deml, V. Stevanovic, C. L. Muhich, C. B. Musgrave, and R. O'Hayre. Energy Environ. Sci. 7, 1996 (2014).
[11] S. Odabaşı, Effect of Cobalt Doping On Photocatalytic Activity of Lead Titanate. M.S. Thesis, M.E.T.U., Ankara (2018).
[12] D. M. Smyth, The Defect Chemistry of Oxides, Chapter 5, Oxford University Press, New York (2000).
[13] A. Abragam, and B. Bleaney, Electron Paramagnetic Resonance of Transition Ions. Clarendon Press, Oxford, (1970).
[14] R.-A. Eichel, E.Erünal, M.D.Drahus, D.M.Symth, J.van Tol, J.Acker, H.Kungl, M.J.Hoffmann, Phys. Chem. Chem. Phys., 11, 8698–8705 (2009).
[15] A. Elbasset, T. Lamcharfi, F. Abdi, L. Mrharrab, S. Sayouri, Indian Journal of Science and Technology, 8(12),1-6 (2015)
[16] D. A. Vinnik, D. A. Zherebtsov, R. Niewa, L. I. Isaenko, and G. G. Mikhailov. Russ. J. of Gen. Chem., 84 (10) 1888–1892 (2014).
[17] K. Misra, S. I. Andronenko. Journal of Applied Physics, 99, 08M106 (2006)
[18] S. Frank, E. Deery, A.A. Brindley, H.K. Leech, A. Lawrence, P. Heathcote, H.L. Schubert, K. Brocklehurst, S.E. Rigby, M.J. Warren, R.W. Pickersgill. J. Biol Chem. 23957-23969 (2007).
[19] B. A. Riga, M. D. Neves, A. E.H. Machado, D. M.S. Araújo, J. R. Souza, O. R. Nascimento, V.T. Santana, C. C.S. Cavalheiro, V. P. Carvalho-Jr, B. E. Goi. Inorganica Chimica Acta, 471, 620–629 (2018).

Investigation of Rb substitution on the thermoelectric parameters of BSCO Ceramic Materials

B. Özcelik[1], G. Çetin[1], A. Sotelo[2], M.A. Madre[2]
[1]*Department of Physics, Faculty of Sciences and Letters, Çukurova University. 01330 Adana, (Turkey)*
[2]*ICMA (CSIC-Universidad de Zaragoza). C/Maria de Luna, 3. 50018-Zaragoza (Spain)*
Corresponding Author: ozcelik@cu.edu.tr

Abstract

This study will address the main themes of today, such as reliability, sustainable and clean energy. Within this objective, $Bi_2Sr_{2-x}Rb_xCo_2O_y$ (x=0.0, 0.025, 0.050, 0.075, 0.100 and 0.125) materials have been produced as powder by solid state technique. From the resistivity graphic, we can reach that pure and 0.025 Rb samples exhibit a semiconducting-like behavior ($d\rho/dt<0$) and the other samples exhibit a metallic-like behavior ($d\rho/dt>0$). The Seebeck coefficients of all samples are positive values for all temperature ranges evidencing the conduction mechanism mainly governed by holes. The maximum power factor values have been obtained in Rb=0.10 sample as 0.19 Mw/K^2 at around 650 ^{0}C.

Keywords: Thermoelectric oxides; Resistivity, Seebeck Coefficient, Power Factor

1. Introduction

Thermoelectricity (TE) represents the direct solid-state conversion between thermal and electrical energy due to the Seebeck effect. In the current scenario, where more than half of the energy produced end up wasted in form of heat, TE energy conversion constitutes an alternative solution to improve energy efficiency of current industrial and domestic processes. Additionally, TE modules have non-moving parts, which make them silent, reliable and light. TE modules also represent an attractive alternative to power wireless sensors and systems, replacing batteries or expensive wiring. The efficiency of these materials is determined through the figure of merit, ZT ($=S^2T\sigma/\kappa$; S: Seebeck coefficient, T: absolute temperature; σ: electrical conductivity; and κ: thermal conductivity). Consequently, good thermoelectric materials should possess high S, σ, and working T, together with low κ. Nowadays, it is possible to find many works in the literature working on the improvement of ZT mostly by raising their electrical performances [1]. Thermoelectric materials involve a huge family, from semimetals and semiconductors to ceramics obtaining in different crystalline forms, from single crystals and polycrystals to nanocomposites [2]. Nowadays, the highest performances have been obtained in intermetallic TE materials such as Bi_2Te_3 [3]. However, due to their low chemical stability, reflected in oxidation and/or vaporization processes, it is impossible to use them for applications at high temperatures under air. On the other hand, starting from the discovery of the first ceramic material with relatively high thermoelectric properties, NaCoO [4], many efforts have been put forth to obtain high-performance TE CoO-based ceramics for application in energy conversion systems [5-8]. Due to good thermal stability at high temperatures, oxide TE materials may be used at high temperatures under oxygen without degradation. In addition, oxide TE materials possess less toxicity and costs comparison to the conventional intermetallic alloys. The main problem related to these oxides is their relatively low performance when compared with the intermetallic ones. As a consequence, the main objective of research has been focused on raising their TE performances using different processing routes in CoO-based ceramics through grain alignment [5,9-12], or doping [13-16]. The aim of this work is studying the effect of modifying the charge carrier concentration by substituting Rb^+ for Sr^{2+} in $Bi_2Sr_2Co_2O_y$ sintered materials. The structural and microstructural modifications promoted by Rb doping will be determined.

2. Experimental

The $Bi_2Sr_{2-x}Rb_xCo_2O_y$ ceramics, with x=0.0, 0.025, 0.050, 0.075, 0.100 and 0.125) were prepared from commercial Bi_2O_3 (Panreac, 98 + %), $SrCO_3$ (98.5 %, Panreac), Rb_2O (Sigma-Aldrich, +98%), and Co_2O_3 (Aldrich, 98 + %) powders through the classical solid state route. They were weighed in the appropriate proportions, mixed, and ball milled at 300 rpm for 30 minutes in acetone media. The obtained suspension has been dried under infrared radiation and manually milled to break the agglomerates. The homogeneous mixture was then calcined at 750 and 800 °C for 12 h, with an intermediate grinding, to decompose the metallic carbonates. The resulting material was subsequently uniaxially pressed in form of pellets (~3 x 3 mm^2 section and 15 mm length) under an applied pressure of 400 Mpa for 1 minute, followed by sintering in the best conditions determined for this material (810 ºC for 24h with a final furnace cooling)

Electrical resistivity and Seebeck coefficient were determined by the standard dc four-probe technique in a LSR-3 apparatus (Linseis GmbH) between 50 and 650 ºC under He atmosphere.

3.Results and Discussions

The electrical resistivity versus temperature, as a function of Rb content, is exhibited in Fig. 1. As it can be seen, the electrical behaviour of samples is clearly changed by Rb substitution. While pure and x=0.025 samples show semiconducting one ($d\rho/dT<0$), the others exhibit a metallic behaviour ($d\rho/dT>0$). In addition, the electrical resistivity values slightly decrease up to 0.10Rb, and then starts to increase for higher Rb content. This evolution may be explained by the raise in the charge carrier concentration. As it is well known, Rb^+ substitution for Sr^{2+} in the rock salt layer promotes the oxidation of Co^{3+} to Co^{4+} in the conducting layer, raising the charge carrier concentration in the conducting layer. In addition, the raise of electrical resistivity in the sample above 0.10Rb content can be related to an enhanced effect on the charge carrier mobility due to the high amount of defects provided by Rb. The lowest electrical resistivity value at room temperature (13.7 mΩ.cm) has been measured in the 0.10Rb doped samples, which are lower than the previously reported in sintered materials prepared by different methods (19-20 mΩ.cm) [17,18].

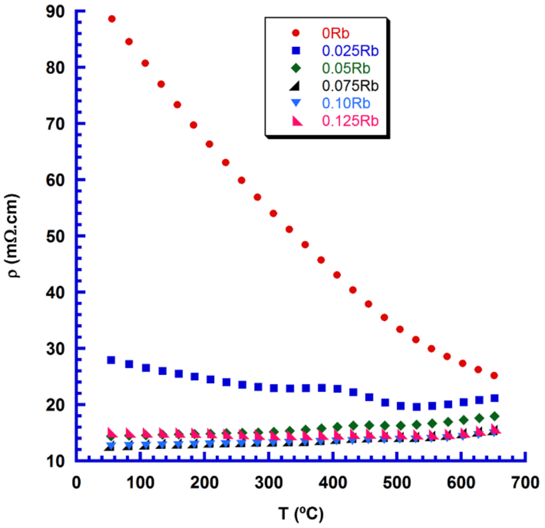

Fig.1. Temperature dependence of electrical resistivity for $Bi_2Sr_{2-x}Rb_xCo_2O_y$ samples

The decreasing of resistivity up to x=0.10Rb content point out to a clear improvement of electrical conduction promoted by Rb doping. These facts show a lower thermoelectric phase content and a significant increase in the number of grain boundaries in the bulk material. As a result, the charge carriers motion is hampered by these surface detections and reveals a significant electrical resistance.

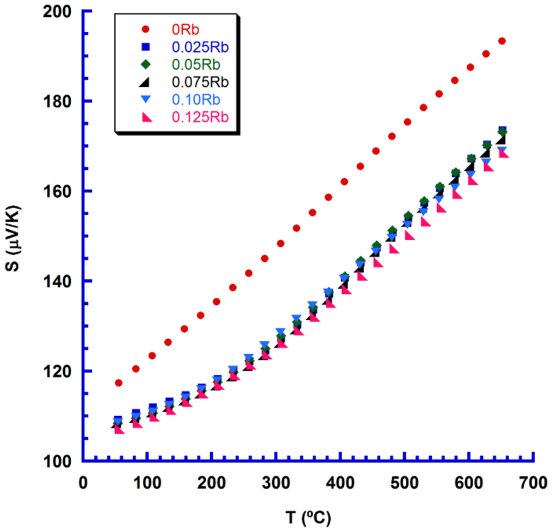

Fig.2. Temperature dependence of the Seebeck coefficient for $Bi_2Sr_{2-x}K_xCo_2O_y$ samples

The change of Seebeck coefficient with respect to temperature, as a function of Rb-content, is shown in Fig. 2. It is easy to argue that the conduction mechanism in the samples predominantly is governed by holes, since the sign of the Seebeck coefficient is positive in the whole measured temperature range. Moreover, the values are linearly increased with temperature for all the samples. This behavior can be related to a metal or degenerated semiconductor typical behavior when the variation of carrier concentration, effective mass, and Fermi level with temperature are negligible. On the other hand, all Rb-doped samples possess lower Seebeck coefficient than the pure sample, in agreement with the electrical resistivity measurements.

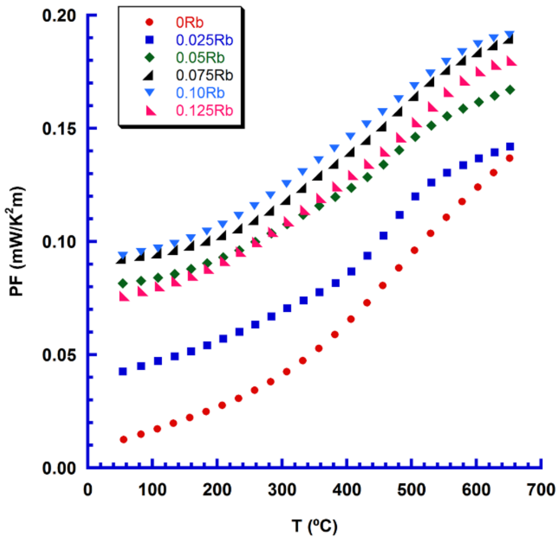

Fig.3. Temperature dependence of the power factor for $Bi_2Sr_{2-x}K_xCo_2O_y$ samples

From the resistivity and Seebeck data, the thermoelectric performances of samples, known as power factor, as a function of temperature were calculated by using PF= S^2/ρ formula. The results are presented in Fig. 3. As it can be seen, all Rb doped samples possess higher PF values than the pure sample as a result of the drastic decrease of electrical resistivity promoted by Rb doping. The maximum values at room temperature (0.095 mW/K^2m) determined in 0.10Rb doped samples are higher than the reported in sintered materials (0.06-0.08 mW/K^2m) [17,18].

4. Conclusions

In this work, $Bi_2Sr_{2-x}Rb_xCo_2O_y$ samples with x = 0, 0.025, 0.05, 0.075, 0.10, and 0.125 have been successfully prepared through the classical solid-state method. A drastic decrease of electrical resistivity, compared with the undoped sample has been ontained in Rb doped samples due to the increase of their density. On the other hand, no significant modification of Seebeck coefficient has been observed, leading to higher power factor values in all the Rb doped samples, when compared with the pure sample. The maximum power factor values have reached 0.192 $mW/K^2.m$ at 650 ºC for x=0.10Rb, clearly indicating that Rb doping is a feasible method to produce high performances thermoelectric ceramics.

Acknowledgement: This work is supported by Research Fund of Cukurova University, Adana, Turkey, under grant contracts no: FBA-2019-12034.

References

[1] D. M. Rowe, Thermoelectrics Handbook: Macro to Nano, 1st edn. CRC Press, Boca Raton, (2006).
[2] J.-C. Zheng, Recent advances on thermoelectric materials, Front. Phys. China 3, 269–279 (2008).
[3] H. C. Wang, J.-H. Bahk, C. Kang, J. Hwang, K. Kim, J. Kim, P. Burke, J. E. Bowers, A. C. Gossard, A. Shakouri, W. Kim, Right sizes of nano- and microstructures for high-performance and rigid bulk thermoelectrics, P. Natl. Acad. Sci. USA 111, 10949-10954 (2014).
[4] I. Terasaki, Y. Sasago, K. Uchinokura, Large thermoelectric power in $NaCo_2O_4$ single crystals, Phys Rev B. 56, 12685-12687 (1997).
[5] N. M. Ferreira, Sh. Rasekh, F. M. Costa, M. A. Madre, A. Sotelo, J. C. Diez, M. A. Torres, New method to improve the grain alignment and performance of thermoelectric ceramics, Mater. Lett. 83, 144–147 (2012).
[6] Y. H. Zhu, W. B. Su, J. Liu, Y. C. Zhou, J. Li, X. Zhang, Y. Du, C. L. Wang, Effects of Dy and Yb co-doping on thermoelectric properties of $CaMnO_3$ ceramics, Ceram. Int. 41, 1535-1539 (2015).
[7] J. Liu, C. L. Wang, Y. Li, W. B. Su, Y. H. Zhu, J. C. Li, L. M. Mei, Influence of rare earth doping on thermoelectric properties of $SrTiO_3$ ceramics, J. Appl. Phys. 114, 223714 (2013).
[8] J. G. Noudem, S. Lemonnier, M. Prevel, E. S. Reddy, E. Guilmeau, C. Goupil, Thermoelectric ceramics for generators, J. Eur. Ceram. Soc. 28, 41–48 (2008).
[9] H. Itahara, C. Xia, J. Sugiyama, T. Tani, Fabrication of textured thermoelectric layered cobaltites with various rock salt-type layers by using b-$Co(OH)_2$ platelets as reactive templates, J. Mater. Chem. 14, 61–66 (2004).
[10] H. Wang, X. Sun, X. Yan, D. Huo, X. Li, J.-G. Li, X. Ding, Fabrication and thermoelectric properties of highly textured $Ca_9Co_{12}O_{28}$ ceramic, J. Alloys Compds. 582, 294-298 (2014).
[11] S. Butt, J.-L. Liu, K. Shehzad, B. Zhan, Y. Lin, C.-W. Nan, High-temperature thermoelectric properties of La and Fe co-doped Ca–Co–O misfit-layered cobaltites consolidated by spark plasma sintering, J. Alloys Compds. 588, 277-283 (2014).
[12] A. Sotelo, Sh. Rasekh, G. Constantinescu, M. A. Torres, M. A. Madre, J. C. Diez, Improvement of textured $Bi_{1.6}Pb_{0.4}Sr_2Co_{1.8}O_x$ thermoelectric performances by metallic Ag additions, Ceram. Int. 39, 1597-1602 (2013).
[13] N. Sun, S. T. Dong, B. B. Zhang, Y. B. Chen, J. Zhou, S. T. Zhang, Z. B. Gu, S. H. Yao, Y. F. Chen, Intrinsically modified thermoelectric performance of alkaline-earth isovalently substituted $[Bi_2AE_2O_4][CoO_2]_y$ single crystals, J. Appl. Phys. 114, 043705 (2013).
[14] Sh. Rasekh, M. A. Madre, J. C. Diez, E. Guilmeau, S. Marinel, A. Sotelo, Effect of Pb substitution on the thermoelectrical properties of textured $Bi_2Ca_2Co_{1.7}O_y$ ceramics prepared by a polymer solution method, Bol. Soc. Esp. Ceram. Vidr. 49, 371-376 (2010).
[15] G. Constantinescu, Sh. Rasekh, M. A. Torres, J. C. Diez, M. A. Madre, A. Sotelo, Effect of Sr substitution for Ca on the $Ca_3Co_4O_9$ thermoelectric properties. J. Alloys Compds. 577, 511-515 (2013).
[16] S. Pinitsoontorn, N. Lerssongkram, N. Keawprak, V. Amornkitbamrung, Thermoelectric properties of transition metals-doped $Ca_3Co_{3.8}M_{0.2}O_{9+\delta}$ (M = Co, Cr, Fe, Ni, Cu and Zn), J. Mater. Sci.: Mater. Electron. 23, 1050-1056 (2012).
[17] M. A. Torres, A. Sotelo, Sh. Rasekh, I. Serrano, G. Constantinescu, M. A. Madre, J. C. Diez, Improvement of thermoelectric properties of $Bi_2Sr_2Co_{1.8}O_x$ through solution synthetic methods, Bol. Soc. Esp. Ceram. V. 51, 1-6 (2012).
[18] E. Combe, R. Funahashi, F. Azough, R. Freer, Relationship between microstructure and thermoelectric properties of $Bi_2Sr_2Co_2O_x$ bulk materials, J. Mater. Res. 29, 1376-1382 (2014).

Revolution in the Aluminum Industry: Scandium

T. Depci[1], E. Bahceci[2]
[1]*İskenderun Technical University, Dept. of Engineering Science, 31200, İskenderun, Hatay, Turkey*
[2]*İskenderun Technical University, Dept. of Metallurgical and Materials Engineering, 31200, İskenderun, Hatay, Turkey*
Corresponding Author: tolga.depci@iste.edu.tr

Abstract

Today's advances in material science have given rise to a new group of metals and elements, especially Rare earth elements which are great attention. Addition of the small amount of REE into base metals (Fe, Al, Cu, Zn,…) and ceramics chances drastically the properties of matter. Among them, Scandium (Sc) is one of them and known as both a rare earth element and a transition element. Depending on the technological evolution and development, scandium is a unique and a key component in producing high strength aluminum alloys. It improves the properties of aluminum alloys and make them better alloys for transportation applications (weight saving), marine equipments (corrosion), thin wall extrusions (flow rate) and decrease the application cost (weld ability). Scandium effects the grain refinement during casting or welding and occurring to Al_3Sc dispersoids in the structure, causing the hardening from Al_3Sc particles. Researches related with aluminum alloys alloyed with scandium have been studied since 1970s. In 2000, 'scandium effect' term was introduced by Milman et al. who prove the positive effect of scandium additions to the chemical and mechanical properties of aluminum alloys [1]. Significant improvements are observed in the properties of commercial 5XXX, 7XXX and other high performance alloys with scandium additions. Our research groups started the foaming and aging of aluminum alloyed with scandium to meet the growing demand for light products, high strength and high performance applications. The previous results showed that the addition of scandium increased the foam aluminum strength by 150 times.

Keywords: Scandium; Al- Foam; Al-Sc; Rare earth elements

1. Introduction

In recent years, due to technological rapid developments, there are needs for new materials with superior physical and mechanical properties compared to traditional materials. Lightness (low intensity), hardness, durability and resistant to environmental conditions are the most important properties of these new materials [2]-[4]. Aluminum is a lightweight metal that can be used in many areas. As know that it is one of the most abundant metal in the earth`s crust [5] and used nearly all sectors from the soft drinks cans to the military applications. Especially, in manufacturing industry, aluminum alloys have been preferred and great attention to improve their mechanical properties has been increased significantly in recent years, due to their ability to combine lightness and strength in a single material [6]. Aluminum alloy production methods are classified according to main alloying elements in it. Generally, forged Al alloy systems (wrought aluminum alloy designation system), cast Al alloy production [7-9], composite form production [10-12] and powder metallurgy have been used to produce aluminum alloys. The high quality of alloying in the productions determines the properties of the material. In order to strengthen Al alloys, alloying elements like Cu, Mn, Cr, Mg, Si etc, are added, resulting in a fine distribution of precipitates [13]. It has been determined that such alloying results in very high mechanical properties. One of them is scandium.

Scandium (Sc), which is known as both a rare earth element and a transition element, is a light metal ($3g/cm^{-3}$). It is a unique and a key component in producing high strength aluminum alloys [14, 15] and makes them better alloys for transportation applications (weight saving), marine equipment (corrosion), thin wall extrusions (flow rate) and decrease the application cost (weld ability). Scandium-reinforced aluminum alloys show significant grain refinement, strengthen welds due to the eliminating the micro-cracks and a good resistance to corrosion environment. Especially, addition of Sc into Al5XXX and Al7XXX increases the strength, density, and thermal stability of these alloys, finding them wide application area in aeronautical, automotive, and transportation industries [16]. Addition of the small amount of scandium (0.2 – 0.6 wt. %) increases of (i) the recrystallization temperature of Al-alloys [17]. and of (ii) strengthening per atom percent of any alloying element [18], causing the production of cast billets with a non-dendritic structure [19], (iii) weldment tensile strength, reducing hot cracking in welds and also (iv) fatigue life [20]. Due to these advantages, Al-Sc alloys are used for the military and aviation industry. In the powder metallurgical process, after addition of Sc, nanosize Al_3Sc occurs and precipitates and this form provides the high strength to aluminum [21]- [23].

The first patent about the Al alloys with Sc was taken in 1971 by Willey and then researches have been significantly increased related with phase transformations of Sc-containing Al alloys and applications [24]. An extensive review of the scientific literature is done by Dorin et al. (2018) who give the brief information about the beneficial impact of Sc on a wide range of Al alloys' properties [25].

Al-Sc alloys have been produced as bulk products and their mechanical properties have been improved. It is contemplated that if such high-strength materials can be produced as a foam form, it will add further benefits, such as resistance at high temperatures, materials with high impact resistance, and ability to easily absorb energy to the alloy. Therefore, our research group has been researched about the effect of scandium on the foam form aluminum structure. It is the first time in the literature. Our research has been continuing and just brief information was given in this text.

2. Production Method of Al-Sc Alloy Materials

Al-Sc alloys are generally produced by simple alloying and dual alloying. It is also alloyed with multiple alloy systems. Generally, production methods of Al alloys are produced by casting, continuous casting, casting + aging, casting + extrusion, electrochemical production and arc furnace method [16], [24], [26-41].

In the production methods, the cast parts are generally subjected to a secondary process (cold / hot rolling, solution, extrusion, aging, Zener method, etc.), causing the formation of Al_3Sc deposits in the microstructure which increases the mechanical properties. Therefore, many researchers have been focus on the forming a secondary phase in the microstructure [16], [24], [31], [34], [42], [43].

In the literature, Sc has been added to into the Al alloys in the production process in order to improve the mechanical properties. Some of them are given in this section. 0.38% Sc was added into the structure of 1XXX alloy system and subjected to cold rolling aging process. It was found that the strentgh of the Sc added Al-alloys increased up to 6-fold compared to pure form [24]. Sc and Zr were added into the 2618 alloy and agging process was applied to the rolled sheet alloy and then mechanical properties were increased [32]. In the study on 3XXX alloy system, flat bars which has Al-0.5Mn-0.2Mg-0.15Zr-0.26Sc chemical composition were produced by extruded method and the result showed that the addition of the micro-alloys increases the mechanical properties of the new alloys [33]. Another form of Al-alloy was produced with addition of Mg and Sc and the hot annealing process was applied to this new obtained alloy [34]. In the same alloy system, another researcher changed the Mg and Sc ratios (Al-5.3Mg-0.3Sc) and applied the cold rolling process, providing the significant improvement in mechanical properties of the 5XXX series [24]. In the 6XXX system, Sc and Zr were added into the 6082 form Al-alloy system and after the extrusion process, immediately T5 aging heat treatment process was applied [35], [38], [44]. In the study on 7XXX alloy system, 7017 alloy material in the sheet form was produced by hot-rolled process. The obtained sheet alloy was ageing to increase its mechanical property [36]. In another study of the same alloy system, flat bars which have Al-8.6Zn-2.6Mg-2.4Cu-0.1Zr-0.2Sc chemical composition was produced by extruded method and then T6 heat treatment was applied to improve the mechanical property [28].

In all of the above-mentioned studies, production methods and other processes are very costly and precise, thus alternative production methods are needed to improve the Al-Sc alloys. A production method that is both easy to manufacture and cost-effective has to be commissioned. It has been determined by our group that production can be made easily by using powder metallurgy method.

3. Results

The use of lightweight materials such as Al is increasing with developing technology. It is well known that Al-alloys must be one of the essential components for aircraft, spacecraft marine and land vehicles [3]. The new generation of Al alloy systems are Al-Sc systems for the new technology. Al-Sc alloy systems provide the desired mechanical properties by developing suitable production methods and applying post-production secondary processes. Powder metallurgical process is one of the most important production methods which generally is preferred in production process. Compared to melting, casting and electrochemical production methods, more complex alloy systems can be produced and formed by the powder metallurgy. In fact, production can be achieved by applying lower heating energies (at sintering temperatures below the melting degree) without switching to the liquid phase. It will allow the production of desired complex shaped parts. Our research group is trying to produce Al-Sc alloy systems in foam form which is extra lighter and more durable materials. Aluminum foams have attracted attention in recent years since they can absorb huge amounts of energy from many other metals, converting the impact energy to plastic energy [45]. In addition to high mechanical properties, easy processes in production will be created and all kinds of engineering materials will be completed.

References

1. Y. V. Milman, D.V. Lotsko, and O.I. Sirko, Mater. Sci. Forum, 331-337, 1107 (2000)
2. M. Kleiner, M. Geiger, A. Klaus, CIRP Annals, **52**-2, 521 (2003)
3. M. A. Meador, NASA Technical Report Server, DI: 20180007697 (2018)
4. M. Hillebrecht, C. Emmelmann, M. Feuerstein, P. Scheller, ATZ worldwide, **120**-9, 62 (2018)
5. G. Budd, Resources and production of aluminium. European Aluminium Association, (Birmingham, 1999)

6. Mario C. Santos Jr and Alisson R. Machado and Wisley F. Sales and Marcos A. S. Barrozo and Emmanuel O. Ezugwu, Int. J. Adv. Manuf. Technol., (2016).
7. A. Luca, N. Balc, I. Drstvensek, A. Popan, Academic Journal of Manufacturing Engineering, 9-3, 74 (2011).
8. j. G. Kaufman, Introduction to Aluminum Alloys and Tempers (ASM International, Ohio, 2000).
9. V. Fallah, D. J. Lloyd, M. Gallerneault, Materials Science & Engineering A, 698, 88 (2017)
10. E. Bahceci, Production of Al Based Composite Reinforced with α-Si3N4 and Characterization of Its Machinability Properties, (Gazi University Institute of Science and Technology, Ankara, 2006)
11. E. A. Chernyshov, A. D. Romanov, E. A. Romanova, Metallurgist, 62:7/8, 815 (2018)
12. F. Chen, N. Gupta, R. K. Behera, P. K. Rohatgi, The Journal of The Minerals, Metals & Materials Society, 70:6, 837 (2018)
13. T. Gladman, Mater. Sci. Technol. 15:1, 30 (1999)
14. Ralph R. Sawtell and Craig L. Jensen, Metallurgical Transactions A, 21A, 421 (1992)
15. J. Royset, N. Ryum, Int. Mater. Rev. 50, 19 (2005).
16. A. Zaki, The Journal of The Minerals, Metals & Materials Society (TMS), 55(2), 35 (2003)
17. L. S. Kramer and W. T. Tack, “Scandium in Aluminum Alloys” (Paper presented at the Alumtech Cong., Atlanta, GA, 19–23 May 1997).
18. M.D. Drits, L.S. Toropova, and Yu G. Bykov, Obbrab. Met., 7, 60 (1983)
19. V.I. Elagin, V.V. Zakharov, and T.D. Rostova, Tsvet. Met. 12, 96 (1982)
20. B. Irvine, Welding Journal, 7, 53 (1995)
21. E.A. Marquis, D.N. Seidman, Acta Mater. 49:11, 1909 (2001)
22. C.B. Fuller, J.L. Murray, D.N. Seidman, Acta Mater. 53:20, 5401 (2005)
23. C.B. Fuller, D.N. Seidman, Acta Mater. 53:20, 5415 (2005)
24. Willey, Aluminum scandium alloy. (Google Patents, 1971).
25. T. Dorin, M. Ramajayam, A.Vahid, T. Langan, Chapter 12 - Aluminium Scandium Alloys in Fundamentals of Aluminium Metallurgy Recent Advances, Woodhead Publishing Series in Metals and Surface Engineering, 439 (2018)
26. K.A. Gschneidner, Jr. and F.W. Calderwood, Bulletin of Alloy Phase Diagrams 10,1, 34 (1989)
27. L. Toropova, D. Eskin, M. Kharakterova, T. Dobatkina, Advanced Aluminum Alloys Containing Scandium: Structure and Properties, (Gordonand Breach, Amsterdam, 1998).
28. J.N. Fridlyander, N.I. Kolobnev, O.E. Grushko and V.G. Davydov: Mater. Sci. Forum, 242, 249 (1997)
29. Y.L. Wu, F.H. Froes, C.G. Li and J. Liu: Proc. Synthesis/Processing of Lightweigth Metallic Materials II, Feb. 9-13, Orlando, FL, USA, 73 (1997)
30. K. B. Ya, Croatica Chemica Acta Ccacaa, 71 (3) 635 (1998).
31. A. Johansen, microstructures and properties of aluminium-magnesium alloys with additions of manganese, zirconium and scandium, (the norwegian university of science and technology (NTNU), march 2000).
32. K. Yu, S. Li, W. Li and Y. Xiao: Trans. Nonferrous Met. Soc. China, 9, 593 (1999),
33. Y.W. Riddle, H. Hallem and N. Ryum: Mater. Sci. Forum, 396-402, 563 (2002)
34. Yu.A. Filatov, V.I. Yelagin, V.V. Zakharov, Materials Science and Engineering, A280, 97 (2000)
35. J. Röyset, U. Tundal, S.R. Skjervold, G. Waterloo, C. Braathen and O. Reiso: Proc. 9th Int. Conf. on Aluminium Alloys, Aug. 2-5, Brisbane, Australia, 246 (2004)

36. A.K. Mukhopadhyay, K.S. Prasad, V. Kumar and S.V. Kamat: Proc. 9th Int. Conf. on Aluminium Alloys, Aug. 2-5,, Brisbane, Australia, 793 (2004)
37. N.I. Kolobnev, L.B. Khokhlatova, S.V. Samokhvalov, A.A. Alekseev, S.V. Sbitneva, T.I. Tararaeva and V.I. Popov: Mater. Sci. Forum, 519-521, 519, (2006)
38. P. Leo, E. Cerri, P.P. De Marco and H.J. Roven: J. Mater. Process. Techn., 182, 207(2007)
39. M. Harata, K. Yasuda, H. Yakushiji, T. H. Okabe, Journal of Alloys and Compounds, 474, 124 (2009)
40. M.E. Krug, D.C. Dunand, D.N. Seidman, Acta Materialia, 59, 1700 (2011)
41. S. Riva, K. V. Yusenko, N. P. Lavery, D. J. Jarvis & S. G. R. Brown, International Materials Reviews, 61:3, 203 (2016)
42. M. S. Kaiser, S. Datta , A. Roychowdhury and M. K. Banerjee, Materials and Manufacturing Processes, 23:1, 74 (2007)
43. A.P. Mukhachov, E.A. Kharitonova, D.G. Skipochka, Past, 1:101, 45 (2016)
44. M. Schöbel, P. Pongratz , H.P. Degischer, Acta Materialia, 60, 4247 (2012)
45. A.G. Hanssen, M. Langseth, and O. S. Happerstad, Int. J. of Impact Eng. 24:5, 475 (2000).